Investigation on Wear Characteristics of HP40Nb Steel and Its Enhancement by Heat Treatment

A Thesis Submitted in

Partial Fulfillment of the Requirements

for the Degree of

DOCTOR OF PHILOSOPHY

by

LEENA HARSHAL NEMADE

(Roll no: 146103048)

DEPARTMENT OF MECHANICAL ENGINEERING

INDIAN INSTITUTE OF TECHNOLOGY GUWAHATI

GUWAHATI, ASSAM-781039

May 2025

Department of Mechanical Engineering
Indian Institute of Technology Guwahati
Guwahati-781039,
INDIA

CERTIFICATE

It is certified that the work contained in the thesis entitled "**Investigation of Wear Characteristics of HP40Nb Steel and Its Enhancement by Heat Treatment"** submitted by **Mrs. Leena Harshal Nemade** (Reg. No. 146103048) to the Indian Institute of Technology Guwahati for the award of degree of **Doctor of Philosophy** has been carried out under our supervision in the Department of Mechanical Engineering. This work has not been submitted elsewhere for the award of any other degree or diploma.

The thesis, in our opinion, has reached the standard fulfilling the requirements for the award of degree of Doctor of Philosophy in accordance with the regulations of the institute.

Professor P. S. Robi
Department of Mechanical Engineering
Indian Institute of Technology Guwahati
Guwahati-781039
INDIA

Professor Pankaj Biswas
Department of Mechanical Engineering
Indian Institute of Technology Guwahati
Guwahati-781039
INDIA

Dedicated to

To my beloved parents,

Smt. Pushpalata and Late Shri. Hemachandra Kisan Jawale, whose support has been my imparted in me the values of resilience and a passion for knowledge.

To my dear husband, Dr. Harshal Nemade whose patience, motivation, and understanding have made this journey achievable, and to my sons Baliraja and Kanad, my true treasure and greatest sources of inspiration and joy.

To my in-laws, Dr. Bhalchandra and Smt. Prathibha Nemade for their warmth, wisdom, and blessings,

Along with always supporting and encouraging my teachers,

With heartfelt gratitude and love, I dedicate this work to all of you.

ACKNOWLEDGEMENT

I sincerely thank my supervisors, Prof. P. S. Robi and Prof. Pankaj Biswas, for their invaluable guidance, support, and encouragement throughout my Ph.D. at Indian Institute of Technology Guwahati. It has been a great privilege to work with Prof. Robi and Prof. Biswas, and I sincerely hope to continue collaborating with them in the future. I would also like to express my heartfelt thanks to the members of my doctoral committee - Prof. Sukhomay Pal, Prof. A. Srinivasan, and Prof. R. Ganesh Narayanan for their constructive advice, thoughtful suggestions, and encouragement during my research journey. I extend my heartfelt gratitude to the former and current heads of the department, including Prof. A.K. Dass, Prof. S.K. Dwivedy, Prof. S. Senthilvelan, Prof. K.S.R. Krishna Murthy, and Prof. Shyamanta M. Hazarika for their generous support and permissions that allowed me to enrol, register, and complete my work at IIT Guwahati.

I am also deeply appreciative of the staff at the Mechanical Workshop for their invaluable assistance in fabricating the experimental setup for this research. My sincere thanks go to the Central Instruments Facility at IIT Guwahati for providing crucial technical support with FESEM and facilities. Additionally, I would like to thank Numaligarh Refinery Limited, Assam, India, for supplying the reformer tube and sharing essential information about it.

Finally, I owe my thanks to my family Dr. Harshal B. Nemade for being a combination of companion and cheer leader in life as well in work, and to Baliraja and Kanad, our cherished sons, my constant sources of inspiration.

I feel a deep sense of loss for not being able to share this occasion with my father, the late. Hemchandra Jawale and my dear brother the late Vikas Jawale.

My unending gratitude extends to my mother Smt. Pushplata Jawale and my in-laws Dr. Bhalchandra and Smt. Pratibha Nemade.

14th April 2025 Leena Harshal Nemade

Abstract

Centrifugally cast HP40Nb reformer steel is primarily used as reformer tubes in steam methane reforming units. The "HP" part refers to "High Performance", while "Nb" represents Niobium, a chemical element added to enhance the alloy's properties. Specifically, HP40Nb (25Cr35Ni1Nb) is a microalloyed austenitic stainless steel, meaning it's primarily composed of iron, chromium, and nickel with a small amount of Niobium added. These reformer tubes are a critical part of hydrogen production processes. These tubes have excellent resistance to corrosion, oxidation, and carburization. Also, it has good weldability, structural stability and strength at elevated temperatures due to the high percentage of nickel and chromium as well as niobium. The parts of these tubes which are exposed to temperatures up to 650 °C for 11 ½ years do not undergo microstructural degradation and therefore maintains its high hardness and strength. Therefore, these parts of the reformer tubes could be utilized in applications demanding exceptional wear resistance even after completing their high-temperature service life.

The present work aims to investigate the abrasive and adhesive wear behaviour of HP40Nb reformer steel tube after being exposed to 650°C for 11½ years. Abrasive wear analysis is done by using Taguchi Design of Experiments (DOE) technique and ANOVA on the as received HP40Nb stainless steel (SS). It was presented in two parts. The first part examines the effects of individual parameters i.e. grit size, load and disc rotational speed with 3 levels each on abrasive wear, while the second part focuses on the interaction between these parameters. Adhesive wear tests were carried out by applying the DOE full factorial technique. It had two parameters like disc rotational speed and normal loads with 4 levels each. The effect of operating parameters on coefficient of friction (COF), wear, sliding distance and surface roughness was investigated. The disc and pin wear surfaces were investigated using different microscopic techniques i.e. OM, SEM/EDS and wear profiles were measured using an optical profilometer. An attempt was made to improve the abrasive and adhesive wear resistance of this steel by one of the highly applicable surface hardening technique, i.e., pack carburizing heat treatment. Pack carburization was done at 950°C temperature for 19.07 hours on the HP40Nb pin samples in a muffle furnace, followed by air cooling. The time and temperature of the pack carburization technique were estimated by applying Fick's second law of diffusion.

From the experimental investigation, it was observed that on abrasive wear, the abrasive grit size is the most significant parameter followed by load and RPM. Also, it was found that the effect of interaction in between the parameters is significant on abrasive wear of this steel.

In case of adhesive wear, at higher rotational speed, the COF has a significant effect from 5 N to 10 N. However, at the lowest rotational speed, the COF has marginal effect for all loads. It was also observed that the wear rate increases as the load increases. Microscopic observation of the wear track revealed various modes of adhesive wear such as ploughing, micro-cutting, plastic deformation, adhesion, and delamination. It was revealed that the rotational speed has significant effect on adhesive wear mechanism. Like, at lower rotational speed, the wear is by plastic deformation along with delamination whereas at higher rotational speed, the mechanism is by plastic deformation along with metal transfer.

A comparative study was carried out between with and without carburization heat treatment of as-received HP40Nb SS material on the surface hardness as well as wear resistance. Surface hardness of the material was found to be increased from 257.4 HV to 490.7 HV (91%) due to pack carburizing heat treatment process. Also, post heat treatment mechanical and microstructural characterizations were conducted to study the wear characteristics of HP40Nb reformer steel. To compare the wear resistance of HP40Nb steel with standard materials i.e. high-speed steel (HSS) and SS304, adhesive and abrasive wear tests were conducted under carefully selected parametric conditions. It was found that, the abrasive wear rate of HP40Nb steel lies between the SS304 and HSS. With finer grit size abrasives, the wear rate of heat-treated HP40Nb steel closely matches that of HSS, while the difference between as-received HP40Nb steel and SS304 is more significant.

In case of adhesive wear, SS304 exhibits the lowest adhesive wear resistance, which follows an increasing order: as-received HP40Nb steel > carburized HP40Nb steel > HSS. At 150 RPM, adhesive wear resistance improves as the normal load increases from 10 N to 20 N, with a similar trend observed at 250 RPM.

Keywords: Reformer Steel HP40Nb, abrasive wear, abrasive wear modes, adhesive wear, adhesive wear modes, pack carburization, abrasive wear resistance, adhesive wear resistance, HSS, SS 304.

CONTENTS

LIST OF FIGURES

LIST OF TABLES

Nomenclature

RMS or R_q	Root mean square
R_t	Total Roughness
R_a	Roughness Average
z (x)	profile heights measured from a reference line
k_s	Specific wear rate
k	Wear rate
μ	Coefficient of friction
F	Force
ϕ	Pin diameter
R_t or R_y, R_{max}	maximum peak-to-valley height
R_v	maximum depth of a valley from the mean line
R_z	average peak-to-valley height
R_{pm}	average height from the mean line to the peaks

Abbreviations

SS	Stainless steel
ANSI	American National Standards Institute
ISO	Organization for Standardization
CLA	centre-line average
HSS	High speed steel
VHN	Vickers hardness number
COF	Coefficient of Friction
RPM	Disc rotational speed
WEDM	Wire-cut electro discharge machining
SEM	Scanning electron microscope
OM	Optical Microscope
XRD	X-ray diffraction
EDS / EDX	Electron dispersive X-ray spectroscope
RPM	Rotations per minute
ANOVA	Analysis of variance
S/N	signal-to-noise
UTS	Ultimate tensile strength
YS	Yield strength
G	Grit size
DOE	Design of experiments
RSM	Response Surface Methodology
MSD	Mean square deviation
F	Fishers ratio
DF	degrees of freedom
Seq SS	sequential sum of squares
Adj SS	adjusted sum of squares
Adj MS	adjusted mean squares
ANSI	American National Standards Institute
ISO	International Organization for Standardization
CLA	centre-line average
HT	Heat Treated
BHT	Before heat treatment
PH	precipitation hardening

Chapter 1
Introduction

Stainless steel is a corrosion-resistant ferrous alloy primarily alloyed with chromium (Cr) and nickel (Ni), supported by minor additions of Mn, Mo, and Si, and containing trace impurities such as S, O, and P; its exceptional durability arises from the formation of a protective passive film, making it a central material in research on corrosion resistance and structural performance. They exhibit exceptionally high corrosion resistance due to the formation of a continuous passive chromium oxide (Cr_2O_3) layer on the surface. This layer is thermodynamically stable in many environments and exhibit self-healing properties. The low ionic and electronic conductivity of this layer supresses corrosion reactions.

- Self-healing: reforms instantly if scratched (as long as oxygen is available)
- Low ionic and electronic conductivity, which suppresses corrosion reactions

Since the passive film on stainless steel responsible for corrosion resistance consists mainly of a thin, continuous chromium oxide (Cr_2O_3) layer, with minor amounts of iron oxides and hydroxides; the chromium-rich inner layer provides the primary protection.

It is a versatile and widely used class of material known for its remarkable properties and applications in various industries such as automotive, aerospace, oil, gas, power plants, construction, chemical, petrochemical, food, beverages etc. These are high alloy steels that contains a minimum of 10.5% chromium by weight along with nickel, which gives it its unique combination of properties viz, excellent corrosion resistance, strength, ductility and toughness. Its unique properties contribute to its popularity in both functional and aesthetic aspects in engineering applications making it a preferred choice for a wide range of applications and consumer use.

Stainless steels are generally classified into four types: ferritic stainless steel, martensitic stainless steel, precipitation-hardening stainless steels and austenitic stainless Steel. The austenitic grades are the widely used grades of SS mainly since they provide predictable levels of corrosion resistance with excellent mechanical properties [1]. Steel, a fundamental material in modern industry, has undergone continuous evolution to meet increasingly demanding mechanical and environmental requirements. HP40Nb steel is an austenitic steel designed for high-temperature and pressure applications, particularly in the petrochemical industries, such as in reformer tubes used in steam methane reforming units. Steam methane reforming is a

common method for producing hydrogen and syngas (synthesis gas), which are essential in various industrial processes. Specifically, HP40Nb (25Cr35Ni1Nb) is a microalloyed austenitic stainless steel, meaning mainly consists of iron, chromium, and nickel, with a minor addition of niobium. Since the Reformer tubes contains high percentage of Ni (20-35 %) and Cr (20-30 %), it has excellent resistance to corrosion, oxidation, high temperature creep and exhibit structural stability from room temperature to above 950°C. The designed life for these tubes, at high temperature applications, is 10^5 hours (11.4 years) [2]. Though the design life is for 11.4 years, several instances of premature failure of these tubes has been reported. The cause of these premature failure is attributed to one or more of the following: (i) tripping causing temperature fluctuation, (ii) localized overheating, (iii) uneven burners firing, (iv) restricted expansion and contraction of the reformer tubes and (v) creep deformation. The premature failure of the HP40Nb reformer tube results in the replacement of the tubes [3–7]. Breakdown maintenance costs due to unexpected failure of the tubes are very high in addition to the revenue loss resulting from the forced shutdown of the plant. The damage rate for the HP40Nb alloy significantly increases with elevated operating temperatures [8]. Investigation of the microstructure of HP40Nb steel reformer tube continuously exposed to a temperature of 997°C at the hot end for 11 ½ years revealed no microstructural degradation at regions along the tube exposed to 510°C for 8 years [9], 650°C for the same period [10]. However, micro-voids were evident in the same tube at locations exposed to 997°C [10]. Few studies also has revealed uneven degradation in the microstructure along the length of the reformer tube [3-11] at sections exposed to higher temperatures. Since the microstructural degradation is confined only to those sections exposed to very high temperatures for prolonged periods of time, parts exposed to lower temperatures can be utilized for other applications instead of salvaging the whole tube [12, 13]. The performance of the reusable part of HP40Nb reformer under various tribological conditions is important and unexplored. The efforts to improve its wear performance by doing surface treatment has potential work in this regard. Research in tribology explores how steel composition, surface treatments, and lubrication affect wear, friction, and energy efficiency, guiding the design of more durable and efficient components for industries like automotive and aerospace.

Wear is an integral part of tribology, influencing material performance and system efficiency. Understanding and controlling wear mechanisms through lubrication, material selection, and surface treatments is crucial for extending the lifespan of mechanical components. The term "tribology" was derived from the Greek word *tribos*, meaning "rubbing," it literally translates

to "the science of rubbing." It involves applying operational analysis to tackle critical economic concerns, including the reliability, maintenance, and wear of technical equipment, ranging from spacecraft to household appliances. Tribology is essential in modern machinery that depends on sliding and rolling surfaces. Examples of useful friction include brakes, clutches, driving wheels in trains and cars, as well as bolts and nuts. Beneficial wear can be observed in tasks like pencil writing, machining, polishing, and shaving. Conversely, undesirable friction and wear are present in systems such as internal combustion and aircraft engines, gears, cams, bearings, and seals [14]. The contact between two materials and the friction between them inevitably lead to wear. In engineering, the impact of sliding speed, surface roughness, and various environmental conditions is typically more pronounced and significant. Friction and wear are interconnected yet distinct phenomena. Wear mechanisms play a role in friction since they require force application and energy consumption. Simultaneously, wear is influenced by the shear forces generated by friction and the rise in temperature due to frictional heating. As a result, friction affects wear behavior, while wear alters surface characteristics, which in turn can impact friction.

Investigation of the tribological characteristics of materials is centred around identifying (i) wear behaviour, (ii) mechanism of wear to identify the losses due to friction and wear (iii) reducing wear rate of the existing materials or (iv) recommendation to replace the existing materials with new materials. It is seen that, the total wear encountered in industrial situations such as, abrasive 50%, adhesive 15%, erosion 8%, fretting 8%, and corrosion 5% [15]. The high percentage of abrasive in industrial applications mandates establishment of standards for evaluating such a wear phenomenon in this material. Similar is the case of adhesive wear. Hence it is important to explore the failure modes, and its mechanism associated with adhesive and abrasive wear. While both adhesive and abrasive wear lead to material loss, adhesive wear results from direct surface contact and bonding, whereas abrasive wear is caused by hard particles or rough surfaces removing material. Controlling these wear mechanisms requires tailored solutions such as lubrication for adhesive wear and harder materials or coatings for abrasive wear.

While previous research has primarily focused on its high-temperature performance in reformer applications, no comprehensive studies have examined its abrasive and adhesive wear behavior, particularly under heat-treated or carburized conditions. This work contributes new insights by investigating the comparative wear performance of HP40Nb against materials of

varying hardness, coupled with detailed post-wear microstructural characterization. By extending the application scope of HP40Nb beyond traditional reformer environments and establishing its tribological behavior, the study provides a significant advancement in understanding and utilizing this high-performance alloy for broader industrial uses.

Conventional machining of HP40Nb steel is extremely difficult due to its high hardness and strain hardening. The high hardness of HP40Nb reformer steel can be utilized for applications requiring high wear resistance. Investigation of wear resistance of HP40Nb steel has so far not been reported. Information regarding the tribological properties of this material will bring insight into its wear resistance and new areas of application. As mentioned earlier, even if the expected life of the reformer tube is complete, a major portion of the tube has not undergone degradation in the microstructure or mechanical properties [9, 10]. Investigation of the wear resistance of HP40Nb steel tubes at these locations will open new avenues for their applications. It was necessary to ascertain whether this portion of the tube could be utilized in wear-resistant applications rather than being discarded as waste.

The present work was therefore taken up with the main objective of investigating the adhesive and abrasive wear behaviour of the HP40Nb reformer steel tube which was exposed to 650 °C for 11 ½ years. An attempt was made to improve the abrasive and adhesive wear resistance of reformer steel by surface hardening, i.e., by pack carburizing heat treatment. Experiments and post heat treatment analysis was conducted to study the wear characteristics of HP40Nb reformer steel, and the results were compared with HSS steel and SS304.

This thesis is organized in seven chapters.

Chapter 1 presents a general introduction to stainless steels, with particular emphasis on the application of HP40Nb steel. The importance of reusing HP40Nb steel after the completion of its designed service life in petrochemical industries is discussed, along with an overview of wear phenomena in steels. The chapter concludes by outlining the aims of the present research work and the overall organization of the thesis.

Chapter 2 provides an extensive review of the relevant literature. The review covers various types of stainless steels, the characteristics and microstructure of HP40Nb steel, and the different types and mechanisms of wear in metallic materials, such as abrasive and adhesive wear. Factors influencing wear behavior, methods of wear evaluation, and the effect of heat

treatment on hardness and wear resistance are discussed. In addition, the chapter includes a discussion on surface characterization techniques and the principles of the design of experiments (DOE). The research gaps identified from the literature are highlighted toward the end of the chapter, leading to the formulation of the specific objectives of the present study.

Chapter 3 describes the methodology adopted to achieve the objectives of the research. It details the experimental procedures, including sample preparation, microstructural characterization using optical microscopy, scanning electron microscopy (SEM), and X-ray diffraction (XRD). The chapter also discusses the pin-on-disc wear testing setup, DOE approaches (Taguchi and full factorial techniques), adhesive and abrasive wear testing methods, surface profilometry, surface hardening techniques, and hardness measurements.

Chapter 4 presents the results and discussion related to the abrasive wear behavior of as-received HP40Nb steel. The outcomes of the Taguchi analysis, analysis of variance (ANOVA), and regression analysis of wear rate are discussed. The influence of various parameters on the coefficient of friction (COF) and wear rate, as well as the corresponding microstructural features, are analysed in detail.

Chapter 5 focuses on the results of adhesive wear testing of as-received HP40Nb steel. The effects of operating parameters on COF and wear rate are presented and discussed with support from debris analysis and the morphology of worn surfaces.

Chapter 6 presents the results of the investigation on the effect of pack carburization on the adhesive and abrasive wear behavior of HP40Nb steel. The influence of surface hardening on hardness and wear resistance is analysed in relation to the resulting microstructural modifications. The wear performance of the heat-treated samples is compared with that of SS304 and high-speed steel (HSS).

Chapter 7 summarizes the major conclusions drawn from the present research work and suggests possible directions for future investigations.

This is followed by a comprehensive list of References and the List of Publications arising from the present work.

Chapter 2
Literature Review

2.1 Introduction

A detailed literature survey was carried out on the topic related to the project. This includes the importance of stainless steel, types of stainless steels heat treatment and their microstructure, applications of stainless steels, HP40Nb steels etc. The wear of materials, types of wear, effect of microstructure on wear, effect of heat treatment on wear. The effect of parameters like load, speed, and surface quality along with methods of characterization is discussed in detail.

2.2. Stainless Steel (SS)

Stainless steel (SS) was first invented in the year 1913 by Harry Brearley of United Kingdom [16]. The name "Stainless steel" evolved due to his high resistance to staining by rusting. This material was first made by alloying 12.5 wt.% chromium into steel. It offers excellent corrosion and heat resistance (up to 1200°C), along with strong formability, weldability, and durability, and is resistant to rust. This steel is highly resistant to many corrosive substances and is more affordable compared to specialized non-corrosive alloys. Over the past century, scientific research and development efforts have led to the creation of numerous stainless steel grades, incorporating various processing methods and enhanced properties tailored for specialized applications. The major grades of stainless steels are Austenitic SS, Pearlitic SS, Martensitic SS, Ferritic SS and precipitation hardening (PH) SS. Scientists have refined alloying techniques to produce stainless steels, enabling better control over their properties and allowing for large-scale manufacturing with consistent quality. A very brief details about the various grades of SS are as follows [1, 17].

2.2.1 Ferritic Stainless Steels

Standard ferritic stainless steels primarily contain chromium (11–19 wt.%) as the main alloying element, with minimal or no nickel content. This composition ensures cost stability and affordability comparable to carbon steels, while offering significantly enhanced corrosion resistance. Their microstructure is ferritic, making them magnetic. To avoid the formation of chromium-rich carbides or nitrides at grain boundaries during welding, small amounts of niobium (Nb) and/or titanium (Ti), which have a higher affinity for carbon and nitrogen than

chromium, are added. As ferrite stabilizers, Nb and Ti also help prevent the formation of martensite. The properties of ferritic SS are: Yield strength (YS) from 275 to 450 MPa; ultimate tensile strength (UTS) from 400 and 600 MPa.; % elongation from 20% to 30%. It can withstand a temperature of up 600–850°C. These steels are commonly used across a range of temperatures, from ambient to elevated levels, particularly in sulphur-rich environments. However, due to their high brittleness at low temperatures, ferritic stainless steels are generally unsuitable for cryogenic applications.

2.2.2 Martensitic Stainless Steels

Martensitic stainless steels have a chromium content comparable to that of ferritic stainless steels. However, to enhance austenite stability at high temperatures a critical factor for effective heat treatment, elements like nickel (Ni), nitrogen (N), or carbon (C) are added. These steels are magnetic and can undergo heat treatment processes similar to conventional carbon steels, including austenitizing, quenching, and tempering. Martensitic stainless steels exhibit the lowest corrosion resistance among stainless steel grades but are widely used in applications similar to other martensitic alloys. The properties of martensitic SS are: YS from 275 to 1,900 MPa; UTS from 500 and 2,070 MPa; % elongation from 2% to 20%. It can withstand a temperature of up 480-650°C. Common uses include surgical instruments, razors, cutlery, bearings, and related items.

2.2.3 Precipitation-Hardening Stainless Steels

Precipitation-hardening stainless steels represent a specialized category designed primarily for applications requiring high strength at elevated temperatures. However, their corrosion resistance is generally not as high as that of standard ferritic stainless steels. These steels are categorized as martensitic, austenitic, or semi-austenitic based on the predominant phase in their microstructure. The properties of precipitation-hardening SS are: YS from 520 to 1380 MPa; UTS from 860–1520 MPa; % elongation from 5% to 25%. It can withstand a temperature of up 595°C. To enhance their strength, elements such as titanium (Ti), aluminium (Al), copper (Cu), niobium (Nb), and molybdenum (Mo) are commonly included in their composition.

2.2.4 Austenitic Stainless Steel

Austenitic stainless steels represent a diverse group, designed to meet specific application needs. Several grades of austenitic stainless steels exist such as 304, 316, 321, HP40Nb reformer etc. each designed for specific applications. The most widely produced and versatile

type is the Cr-Ni alloy, commonly known as "18-8" (type 304). For improved pitting resistance, molybdenum (Mo) is added, resulting in type 316.

These steels maintain an austenitic structure at room temperature due to the stabilizing effects of nickel (Ni) and sometimes manganese (Mn) or nitrogen (N). They exhibit excellent formability across a broad temperature range, from cryogenic conditions to high temperatures, where they retain YS 200-400 MPa and UTS 500-800 MPa and ductility better than ferritic grades. Austenitic stainless steels cannot be heat-treated but demonstrate exceptional work hardenability. Low-carbon variants are specifically developed to address welding issues, such as carbide precipitation, which can cause embrittlement and reduced corrosion resistance.

2.3 HP40Nb Austenitic Stainless Steel

Hydrogen reformer furnaces are extensively used in the petrochemical industry to generate hydrogen-rich gas by processing a mixture of hydrocarbons and steam at high temperatures. HP40Nb reformer steel is primarily used in the construction of reformer tubes and related components in steam methane reforming units. These reformer tubes are a critical part of hydrogen production processes [11, 17]. HP40Nb SS is an austenitic stainless steel which are manufactured by centrifugal casting. The composition of this steel typically contains ~~includes~~ elements such as carbon, nickel, chromium, niobium, and iron. Niobium (Nb) plays a significant role in enhancing high-temperature properties. The alloy typically has chemical composition (wt. %) of C: 0.35-0.45, Cr: 23-27, Ni: 33-36, Mn: 1-1.5, Si: 1-2, Nb: 0.8-1.2 and balance Fe [18-24]. In the decade 60, the reformer tubes used were mostly cast of HK-40 alloy (25Cr-20Ni-Fe). In the decade of 80s, the alloy is modified by Nb resulted in modified HP alloys [2, 25]. This is a high-temperature stainless steel and have been used for the past six decades mainly in applications such as (i) petrochemical industries like reformer tubes for hydrogen production, furnace tubes, heat exchanger parts (ii) fired heaters, (iii) chemical process equipment requiring high temperature exposures and (iv) heat treating furnace tubes.

HP40Nb steel is engineered to withstand extremely very high temperatures for hydrogen production by steam methane reforming. The operating temperatures generally used are at around 1000°C at pressures of around 10 MPa for very long periods, up to 11 ½ years. without deteriorating its mechanical strength. The alloy forms a protective oxide layer on its surface that helps prevent corrosion. This exhibits very high oxidation resistance making the choice for applications where hydrocarbons and steam are present at elevated temperatures.

HP40Nb SS exhibits very high creep resistance when utilized as reformer at high temperatures and nominal pressures making it suitable for long-term use in high-temperature environments. In addition, the steel exhibits high corrosion resistance in some severe corrosion environments generally in chemical industries and refineries. This alloy maintains its mechanical strength at elevated temperatures, ensuring the integrity of reformer tubes and other components under stress. This steel is weldable which is important for the fabrication of very long reformer pipes.

2.3.1 Microstructure of HP40Nb Stainless Steel

The microstructure of these materials features a dendrite with carbide network the inter-dendritic regions. The presence of dendritic structure is due to the centrifugal casting and absence of any deformation processing. A highly dispersed intermetallic phases within austenite grains is also evident [12, 25].

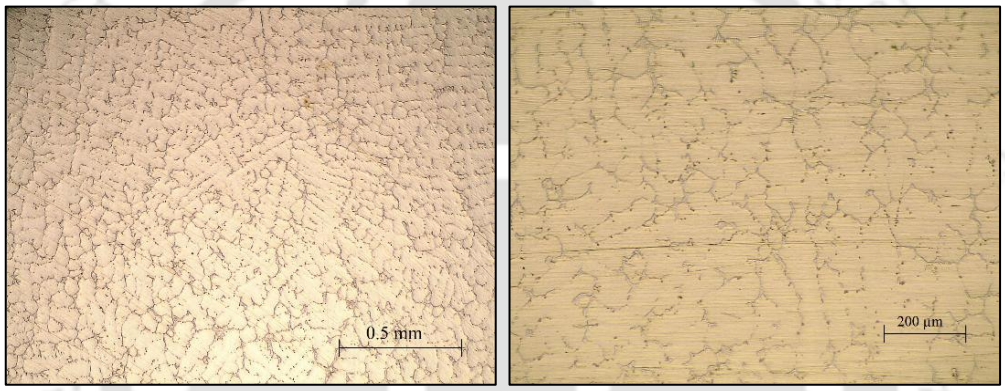

(a) (b)

Figure 2.1 Optical micrographs of as received sample [71]

Figure 2.1 (a and b) shows the typical optical micrograph of the HP40Nb steel revealing dendritic structure with carbide network at the grain boundary region. The carbides are in the form of Cr-rich (Cr_7C_3) and Nb-rich (NbC) particles [26, 27]. At elevated service temperatures, Cr_7C_3 precipitates convert into $Cr_{23}C_6$ [28], whereas NbC [29] carbides retain their chemical composition and morphology at still higher temperatures. Studies shows that prolonged high-temperature exposure of steel results in $Cr_{23}C_6$ formation on the outer tube surface, while the inner surface consists of a mixture of $Cr_{23}C_6$ and Cr_7C_3 [30-32]. Addition of 0.8–1.2 wt.% Nb and Ti as alloying elements enhances microstructural stability at service temperatures by inhibiting the transformation of Cr_7C_3 into $Cr_{23}C_6$ through NbC precipitate formation. At 1000°C, $Cr_{23}C_6$ decomposes, facilitating chromium diffusion into the Nb-rich carbide region, which results in the formation of CrNbC [33].

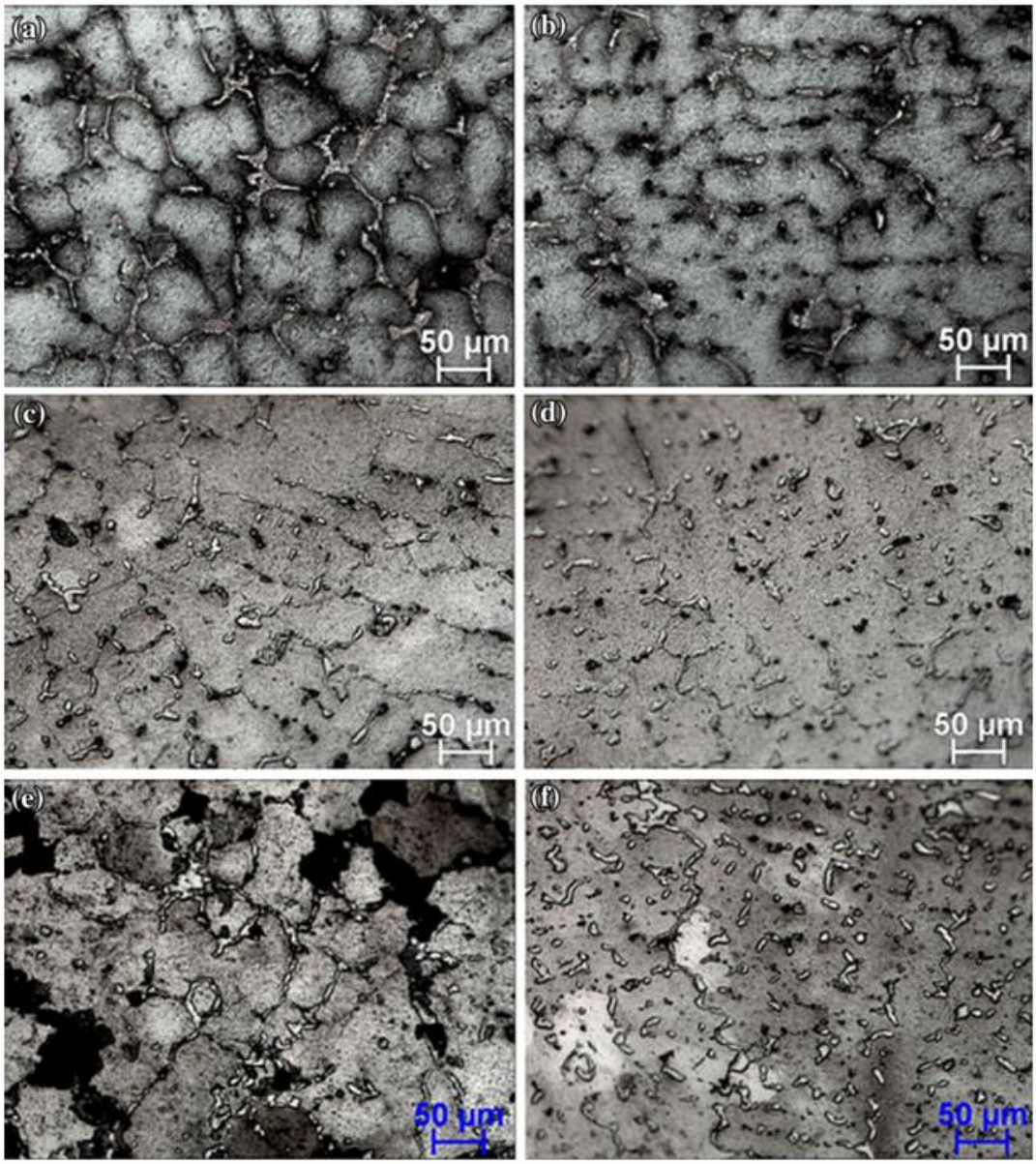

Figure 2.2 Optical micrographs of HP40Nb reformer steel specimen exposed to wall (a) and (b) 650 ° C, (c) and (d) 820° C and (e)and (f) 997 ° C. locations of (a), (c) and (e) at inner wall region and (b), (d) and (f) near to the outer wall [10]

Prolonged exposure to high temperatures leads to chromium depletion in the matrix and the coarsening of interdendritic carbides [34]. The tensile strength of HP40Nb steel at 900°C improves and stabilizes after 1500 hours of aging, attributed to the transformation of unstable Cr_7C_3 into stable $Cr_{23}C_6$ carbide. In contrast, the Charpy impact strength progressively declines with prolonged aging [34]. The tensile strength of these materials was degraded after approximately 11 years of service exposure at 950°C [5]. It is reported that, at elevated temperatures, an increase in carbon content enhances the mechanical properties, but the formation of Cr-rich carbides at these temperatures results in reduced ductility of the steel. A

network of coarse Cr-rich carbides forms at the grain boundaries, accompanied by crack growth along these boundaries near the inner wall of the tube exposed to 997°C [10, 104].

Reformer tubes exposed to high temperatures primarily fail due to several creep-related damage mechanisms, such as microstructural degradation, high-temperature fatigue, a combination of creep and fatigue, embrittlement, hydrogen-induced damage, graphitization, thermal shock, erosion, and high-temperature corrosion [35]. In HP40Nb micro-alloy steels, cavities and micro-cracks are more likely to form in chromium-rich precipitates than in Nb-rich carbides [36]. Achieving the right balance of temperature, pressure, and alloy is crucial to ensure that the material meets its intended design life. The material retains its high hardness and resists microstructural degradation even after exposure to 650°C for 11 ½ years. As a result, reformer tubes can still be used in applications requiring outstanding wear resistance, even after their high-temperature operational life has ended.

2.4 Wear in Metallic Alloys

Wear is the surface deterioration or material loss that occurs on one or both solid surfaces due to relative motion such as sliding, rolling, or impact, typically resulting from interactions at surface asperities. Wear occurs in machine tools such as cutting tools in lathe, milling and drilling machine, gears, bearing and shafts. In automobile engines it occurs in piston rings and cylinder walls, cam shafts and valve lifters, transmission gears etc. In locomotives and railways, railroad tracks and wheels, brake discs and pads, coupling and suspension systems etc. Wear is inevitable and is considered a primary factor contributing to the failure of machine components. Depending on the material, environment, surface condition etc., wear occurs in different forms. Wear can result from a surface interacting with other metal or non-metal surfaces, flowing liquids, or solid particles and liquid droplets carried by moving gases. Ultimately, wear leads to material loss from the surface or the transfer of material between contacting surfaces. Failures due to wear arise from a material's or system's vulnerability to surface alterations caused by this process. The study of a material's tribological properties focuses on: (i) understanding its wear behavior, (ii) analysing wear mechanisms to determine friction- and wear-related losses, (iii) minimizing the wear rate of current materials, or (iv) suggesting alternative materials to replace those in use. The wear behaviour of a material describes its tendency to degrade or lose material over time due to mechanical interactions like friction, abrasion, erosion, or adhesion during operation [figure 2.3].

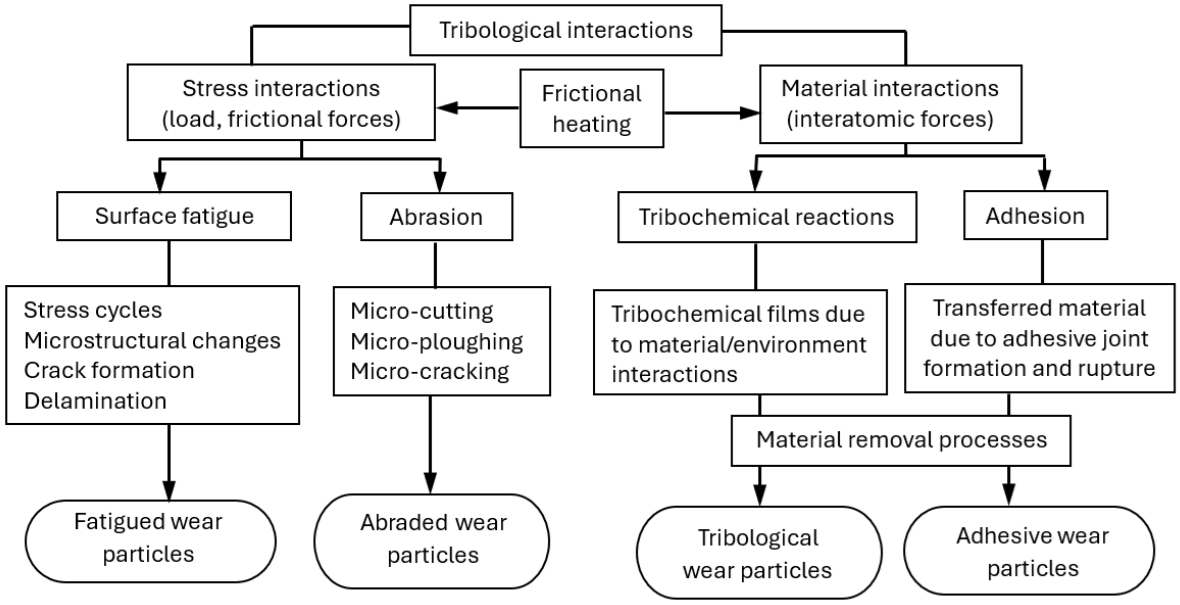

Figure 2.3 Tribological solid/solid interactions and wear mechanisms [37]

Analysing wear behaviour is essential for choosing suitable materials and designing components in engineering systems, as excessive wear can result in failures, reduced efficiency, and increased maintenance expenses. Under conditions of solid-on-solid sliding contact, the interplay of stresses, material interactions driven by interatomic forces, and the heat generated from interfacial friction results in wear of varying intensity.

Wear processes can be categorized into various types based on the load and the materials involved, including abrasive wear, adhesive wear, fatigue wear, and corrosive wear. Eyre [15] has reported the distribution of wear types in industrial settings as follows: abrasive wear comprises approximately 50%, followed by adhesive wear at 15%, erosion and fretting wear each at 8%, and chemical wear at 5%. Given that abrasive wear constitutes roughly half of total wear in industrial environments, establishing standards to assess this phenomenon becomes imperative for achieving prolonged machinery lifespan and conserving energy and resources. Different types of wear depending on the service conditions are classified as [14]:

- abrasive wear: polishing, scouring, scratching, grinding, gouging.
- adhesive wear: galling, scuffing, scoring
- cavitation: interaction with fluid
- corrosive Wear: chemical in nature
- erosive wear
- fretting wear: (wear from short oscillating motion)

2.4.1 Abrasive Wear

Abrasive wear happens when hard particles are forcefully applied to a solid surface and move along it as shown schematically in figure 2.4. It is the most common and rapidly occurring form of wear observed across various industrial sectors. Abrasive wear occurs through various material removal mechanisms, including cutting and scratching, which cause surface damage and may result in either single or recurring plastic deformation. For an abrasive material to induce wear on a surface, the hardness of the abrasive must be greater than the hardness of the surface [14].

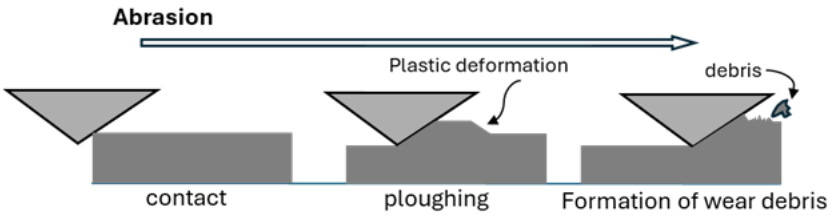

Figure 2.4 Abrasive wear

Abrasive wear can occur in almost any environment, including air or liquids in the presence of abrasive particles. It is especially common during the handling and processing of raw materials like ores, minerals, and metals. Its effects are most evident in the agricultural, mining, mineral processing, and earth-moving industries. Moreover, wear is a major issue in numerous machine components, frequently serving as a crucial factor in defining or restricting their lifespan. A notable example is the wear found in dies and moulds. Abrasive wear occurs by either two or three body abrasion.

Two-body abrasion occurs when the harder of two contacting surfaces abrades the other as shown in figure 2.5. This is commonly observed in mechanical processes like grinding, cutting, and machining. Two-body abrasive wear happens in metal-on-metal contact when the asperities on the harder surface scrape or cut into the softer surface. Since asperities are present on all engineering surfaces and cannot be entirely removed, even with highly precise polishing, the potential for two-body abrasion is always present. Three-body abrasion happens when a hard, abrasive particle becomes trapped between two surfaces that are moving relative to each other, causing wear on one or both, as depicted in figure 2.5 (b). Initially, the wear mechanism is often adhesive, producing wear particles that become trapped at the interface, leading to three-body abrasive wear [14]. Two body abrasive wear processes occur in two ways such as by (i) the creation of plastically deformed grooves without the removal of metal and (ii) detachment of metal particles as microchips [38].

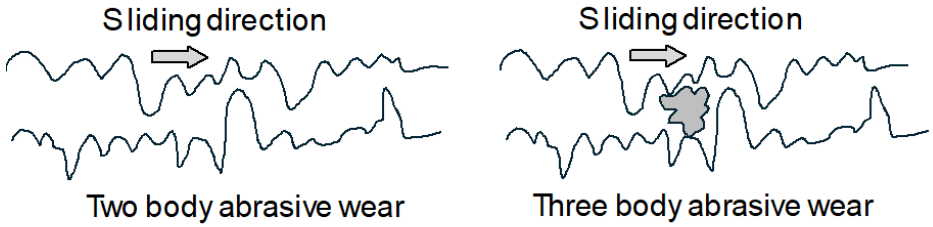

(a) (b)

Figure 2.5 Schematic of (a) two body and (b) three body abrasive wear

Three-body abrasion occurs when foreign hard particles are either trapped between two sliding surfaces, causing wear on one or both surfaces, or embedded in a softer surface, where they abrade the opposing surface. Examples of three body abrasive wear are commonly found in the mining industry and in machines operating in desert environments. In practice, two-body and three-body abrasions often occur simultaneously, as a situation that starts with metal-on-metal contact (two-body) can shift to three-body abrasion. This can occur, for instance, when work-hardened wear debris forms or abrasive particles are introduced via contaminated lubricant. A key requirement for abrasive wear is that, during friction, the abrasive material's surface must be harder than that of the material being worn. Abrasive wear can be further classified into several subcategories, as outlined in Table 2.1.

Table 2.1 Subcategories of abrasive wear [39]

Attribute	Variations
Count of entities	Single-body (abrasive surface) or duel-body (loose particles between surface
Stress level	High stress or low stress
Surface modification	Scratching, polishing or gauging
Fluid occurrence	Dry wear or liquid-based abrasion (particles in fluid medium)
Particle hardness compared to surface	Harder or softer surface compared to particles

2.4.2 Factors Influencing Abrasive Wear Behavior

Wear, like friction, is not an inherent material property but rather a system response influenced by operating conditions at the interface. The factors that influence abrasive wear behavior are outlined in the Table 2.2. For both the abrasive and the material being worn, the majority of the factors impacting abrasive wear are linked to their mechanical properties. Equally significant is the mechanical interaction between the abrasive and the wear material.

Table 2.2 Factors influencing abrasive wear behavior [39]

Abrasive properties	Particle size and shape, hardness, YS, fracture properties, concentration level
Contact conditions	Impact force, speed, impact orientation, sliding/rolling movement, thermal condition, Moist/dry, Acidity/alkalinity
Wear material properties	Resistance to indentation, YS, modulus of elasticity, ductility, impact resistance, work hardening behavior, fracture resistance, microstructure, resistance to corrosion

The impact of the parameters shown in Table 2.2 can be understood through their influence on the mechanisms responsible for material removal from a worn surface. Following are the different modes responsible for material removal.

2.4.3 Abrasive Wear Modes

During abrasion, removal of material from a surface by means of plastic deformation can occur through various modes, incorporating cutting, ploughing and wedge formation.

a) Cutting: In this mode of abrasive wear, the material is removed in a significant amount as compared to the displaced material. An abrasive tip cuts a groove, displacing material as discontinuous or ribbon-shaped debris particles, much like those formed in metal cutting processes.

b) Ploughing: In the ploughing process, also known as ridge formation, material is moved out of a groove, creating ridges along its sides without any removal of material. Ploughing creates a series of grooves created by the plastic flow of the softer material.

c) Wedge formation: In wedge formation abrasive wear, an abrasive tip cuts a groove while creating a wedge at its front. In this case, part of the displaced material moves to the sides, while the rest accumulates as a wedge.

Various mechanisms and laboratory test-methods for examination of abrasive wear on metals are available in literature [38, 40, 41]. In one approach, hard materials or abrasive particles create surface grooves without material removal, while another method involves the removal of metal microchips. Some abrasive grains merely create elastic contact with the surface, while in others, secondary chips are formed from the extruded fins along the edges of grooves created during rubbing.

To reduce abrasion damage in industrial equipment, it is crucial to have a clear understanding of abrasive wear mechanisms and how the materials used for parts or

components respond to abrasion, particularly regarding their suitability for manufacturing complex designs.

Abrasive wear causes various morphological alterations on the abraded surface. Numerous researchers have examined a broad range of factors that can affect the abrasive wear of materials [14, 42, 43]. The literature indicates that the interaction between parameters in dry sliding wear is unique and intricate. Choosing the optimal combination of parameters is crucial for minimizing the specific wear rate and coefficient of friction. The Taguchi technique is considered a valuable method for addressing responses influenced by multiple variables [44-58]. It is designed for optimizing processes and identifying the optimal combinations of parameters for a given response. This method greatly reduces the number of trials needed to model the response function, in contrast to the full factorial design of experiments. The key advantage of this technique is its ability to reveal potential interactions between factors. Both abrasive wear (50%) as well as adhesive wear (15%) have great influence among all the wear types in industry settings [14].

2.4.4 Adhesive Wear

Adhesive wear takes place when two solid surfaces slide against one another under load, causing material degradation. The microscopic asperities on the surfaces experience high contact stress, resulting in localized bonding or welding at the interface. As sliding progresses, these bonds break, resulting in material transfer between the surfaces or the formation of wear particles [14]. Following are the characteristics of adhesive wear.

a) Material Transfer: Small fragments of one material adhere to the other surface, creating surface roughness and potential damage.

b) Cold Welding: At a microscopic level, the asperities experience plastic deformation and form micro-welds under pressure.

c) Wear Debris: As the micro-welds break, they form tiny particles that can further contribute to abrasive wear.

d) Surface Damage: It typically results in surface scoring, galling, or scuffing, depending on the severity. Figure 2.6 shows the schematic of adhesive wear mechanism.

Metallic components in sliding contact can experience significant damage due to wear. The wear resistance of structural steels such as Fe–Mn–Si–Cr–Ni stainless steel and AISI 321 SS has been investigated [15], Hadfield steel [59], powder metallurgy steel components has been reported [60].

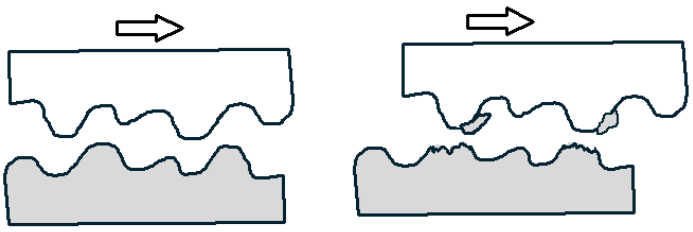

Figure 2.6 Schematic of adhesive wear mechanism

The influence of various parameters like sliding speed [61], TiC coating on tool surface [62], the effect of microstructure and hardness on ferritic steel [63], temperature [64], etc. reports have been made on the wear resistance of these materials. A study on the impact of temperature on the wear process shows that the formation of a protective metal oxide leads to enhanced wear resistance [65]. The study also found that at extremely high temperatures, the accelerated oxidation rate, along with the compaction and sintering of these layers, leads to a significantly low abrasive wear rate. The impact of nitriding on the high-temperature friction and wear resistance of various tool steels has been documented [66]. Research on the effect of sliding wear on both austenitic and austenitic-ferritic stainless steels is also available in the literature.

Adhesive wear plays a significant role in the failure of materials with sliding contacts, contributing to about 70% of typical component failures. Therefore, it is crucial to investigate the mechanisms and various failure modes associated with adhesive wear. Material properties significantly influence adhesive wear. Factors that can help prevent adhesive wear include reducing load, speed, and temperature as much as possible, increasing the contact area, using harder materials, selecting dissimilar materials, or having oxides present on the contact surface, among others [67]. Wear modelling and its numerical simulation [68, 69] or experimental study [70, 71, 72] is important to gain an understanding of adhesive wear in each material. The adhesive wear of material is influenced by various factors as below.

2.4.5 Factors Influencing Adhesive Wear

a) **Material Properties:** Softer materials are more prone to adhesive wear, while harder materials resist it. In material combinations involving dissimilar materials, wear particles are generated from both materials. However, the softer material tends to produce more particles, which are typically larger than those from the harder counterpart.

b) **Surface Roughness:** Smoother surfaces can actually increase adhesion, while controlled roughness can reduce it [98].

c) **Load and Speed:** Higher loads and sliding speeds intensify adhesive wear.

d) **Lubrication:** Proper lubrication reduces direct metal-to-metal contact, minimizing adhesion.

Conventional machining of HP40Nb SS is highly challenging due to its exceptional hardness and strain hardening. The high hardness of HP40Nb reformer steel makes it suitable for applications that require significant wear resistance. However, research on the wear resistance of HP40Nb steel has not yet been reported. Investigating the tribological properties of this material will provide valuable insights into its wear resistance and potential new applications. As previously noted, although the expected life of the reformer tube is complete, a large portion of the tube remains unaffected in terms of microstructure and mechanical properties. Studying the wear resistance of HP40Nb SS tubes in these areas will open up new possibilities for their use. It is important to apply the most suitable method to find wear in metals. Different wear calculation models are proposed by various researchers are discussed as follows:

2.4.6 Wear Calculation Models

Various equations have been formulated to model wear under different conditions. The most commonly used wear equations, along with their original references, are outlined below.

a) Archard's Wear Equation: Archard's equation is the most widely used model for adhesive wear. It relates the volume of worn material to the applied load, sliding distance, and material properties. Archard's analysis indicates two basic principles of wear: the wear rate is independent of the apparent contact area and directly correlates with the applied load.

$$V = \frac{KWL}{H} \tag{2.1}$$

where V is wear volume (mm³ or m³), K is wear coefficient, W is normal applied load (N), L is sliding distance (m), H is hardness of the softer material.

b) Rabinowicz Wear Equation: Rabinowicz refined Archard's model, incorporating the probability of asperity fracture.

$$V = \frac{KWL}{H} \times P \tag{2.2}$$

where V is wear volume (mm³ or m³), K is wear coefficient, W is normal applied load (N), L is sliding distance (m), H is hardness of the softer material and P represents the probability of asperity junction fracture.

(c) Khrushchov Wear Equation: Khrushchov introduced an equation for abrasive wear considering wear as the result of micro cutting [38].

$$Q = \frac{KWL}{\sigma 0} \tag{2.3}$$

where Q is wear rate (volume loss per unit load and distance), K is wear coefficient, σ_0 is Flow stress of the material.

From above models it can be seen that, improving surface hardness can help to reduce the wear in metals.

2.5 Effect of Hardness and Surface Hardening

Hardness plays a very important role in the wear resistance of material. Higher hardness results in reduction in wear [73-77]. Centrifugally cast HP40Nb micro alloyed austenitic stainless steel have been used as reformer tube materials in petrochemical industries for several decades. Very often, instances of premature failure of these materials due to creep deformation at sections exposed to very high temperature (~1000°C) has been reported by industries. The petrochemical industries generally discard such entire tube as scrap. Investigation reveals that the sections of the prematurely failed tubes which were exposed to temperatures less than 650 °C for very long time have undergone neither any microstructural changes nor deterioration in the mechanical properties [3, 10, 78]. Since the hardness of these components are high, it appears that these tubes can be used for applications requiring high wear resistance.

The wear behaviour of different types of coatings such as TiCN, CrN, TiAlCrN, TiN, and TD on SKD11 tool steels UHSS pair [79] have been reported. Adhesive and abrasive wear behaviour of steel coating done by electrochemical deposition, thermochemical treatment, CVD, PVD and plasma spraying on phase composition, thickness, hardness and roughness are described are also reported [80]. Abrasive wear between hardened steel - flat surfaces of brass (60Cu-40Zn) and S45C (0.45C steel) - SUS304 (18Cr-8Ni austenitic stainless steel) [81] are also investigated in detail by researchers. The wear resistance of pure metals such as W, Mo, Fe, Ni, Cu etc. and annealed steels increases in direct correlation with their hardness levels. Heat-treated steels show an increase in wear resistance with hardness, although this increase is generally lower compared to that observed in pure metals with equivalent hardness levels [82, 83]. Given its widespread occurrence across various industries, comprehending the mechanisms underlying abrasive wear is essential for analysing wear patterns. [4, 5].

Efforts have been made to enhance the wear resistance of metals by increasing their hardness by surface hardness heat treatments such as carburizing, nitriding, boriding, cyaniding, induction hardening, cladding etc. [15, 77, 84-88]. Among these, carburization and nitriding are the most popular surface hardening treatments employed to improve the hardness and wear resistance of low carbon steels [88, 92-98]. Nitriding is generally carried out on steels at the ferritic temperature range. Literature indicates that the carbide network can be controlled with reasonable accuracy by adjusting the process parameters, viz, temperature, time, and carbon concentration before carburizing [99].

2.5.1 Pack Carburizing Heat Treatment

Carburizing is a very old process, used for centuries to surface harden steels. Powder carburizing (charcoal), salt bath carburizing (cyanides), gas carburizing and plasma carburizing are among possible carburizing techniques available nowadays.

Pack carburization (pack carburizing) is a traditional thermochemical surface-hardening process in which low-carbon steel parts are buried in a solid carbonaceous "pack" (charcoal, coke or other carbon sources) together with a small amount of carbonate energizer, sealed in a retort and held at elevated temperature so carbon atoms produced at the pack surface diffuse into the steel to form a hard, wear-resistant case over a tougher core; the resulting case depth and carbon profile are governed mainly by carburizing temperature, time and the carbon activity of the pack, and parts are typically subsequently quenched and tempered to produce the desired combination of surface hardness and core toughness [106].

Since HP40Nb steel is austenitic at room temperature, carburizing heat treatment appears to be the most suitable heat treatment for enhancing the surface hardness. Since the stable austenitic microstructure prevent quench hardening, hence pack carburization is adapted in this work to improve the surface hardness of HP40Nb reformer steel. Literature regarding the effect of heat treatment on the hardness and wear resistance of HP40Nb steel is not available in the open literature. Therefore, this study was taken up with the aim of studying the effect of carburizing heat treatment on the microstructure, hardness, and wear resistance of HP40Nb austenitic steel.

Centrifugally cast HP Grade (25Cr, 35Ni, and 0.4C) creep-resistant austenitic stainless-steel alloys have been utilized in steam reforming operations [11, 17]. The designed lifespan of these tubes for reformer applications is approximately 10,500 hours (11 years). However, early failure of these tubes has been reported due to various factors such as reformer tripping leading to temperature fluctuations, localized overheating caused by impaired catalysts, temperature differences along the tube, uneven burner firing, restricted expansion and

contraction of the reformer tubes, and arching of the tubes. As a result, the early failure of the HP40Nb reformer tubes has led to their replacement [3, 11]. From the literature it is seen that there is no microstructure degradation due to the service exposure at 650°C whereas micro-voids were evident at tube locations exposed to 997°C [9, 10]. Also, among the total length of the reformer tube only 1/3 of the portion of the tube is exposed to a high temperature above 650°C. Since the catalyst tube assembly can amount to 25% of total cost of the furnace, optimizing its design from chemical, thermal, and mechanical points of view is a great incentive. Being costly material, it can be reused as wear resistant material further. The wear behaviour of reformer steel has not been reported so far by anyone. It is therefore necessary to investigate the wear resistance of HP40Nb steel. For experimental investigation and analysis various design of experiments techniques available in literature are discussed as follows.

2.6 Design of Experiments (DOE)

Design of Experiments (DOE) is a methodical approach to exploring and evaluating how different variables impact the outcome of the process. It is a systematic approach used in scientific and industrial research to plan, conduct, analyze, and interpret controlled tests. It helps in understanding the relationships between input factors (independent variables) and output responses (dependent variables) are explored with the aim of minimizing experimental costs and time [44-58].

2.6.1 Key Parameters of DOE

The following are the key parameters of DOE.

a) Factors: These are the independent variables that impact the outcome of an experiment, such as load, speed or temperature.

b) Levels: The specific values or conditions assigned to each factor, such as low, medium, or high.

c) Response: The dependent variable or measurable result influenced by changes in the factors, including aspects like wear rate, COF, or strength.

2.6.2 Types of Experimental Designs

a. Full Factorial Design: It tests all possible combinations of factor levels. Suitable for small experiments where interactions between factors need to be fully explored. Example: Studying three factors (A, B, C) at two levels (high/low) requires $2^3 = 8$ experiments.

b. Fractional Factorial Design: It uses only a subset of all possible combinations, reducing the number of experiments. It is suitable when many factors exist, but full experimentation is impractical. Example: Instead of running 16 experiments for four factors, a fractional factorial design might use only 8 trials.

c. Response Surface Methodology (RSM): It is used for optimizing processes by modelling nonlinear relationships between factors and responses. Example: Optimizing temperature and reaction time to maximize yield in a chemical process [54, 56-58].

d. Taguchi Technique: It focuses on robust design to improve product quality by reducing variability. It uses orthogonal arrays to systematically study factor effects. Example: Improving the durability of an automotive component by optimizing material composition and processing conditions [44-50].

e. Randomized Block Design (RBD): It accounts for variability due to uncontrollable factors by grouping similar experimental units into blocks. Example: Testing different parameters on wear while considering variations in composites.

2.6.3 Taguchi Method

To minimize the specific wear rate and coefficient of friction, it is crucial to choose the optimal combination of parameters. The Taguchi technique is a key method for addressing responses influenced by multiple variables. Dr. Genichi Taguchi of Nippon Telephone and Telegraph Company, Japan, introduced this method as an effective, simple, and reliable technique for optimizing process parameters. It combines the principles of Design of Experiments with control parameter optimization to achieve optimal process performance. In this method, the key factors affecting the process are systematically organized in rows, known as Orthogonal Arrays. These arrays are designed to reduce variance while identifying the optimal combination of control parameters. By utilizing Orthogonal Arrays, a well-structured set of experiments can be performed with fewer trials.

To assess process parameters, Taguchi's method employs a statistical measure called the Signal-to-Noise (S/N) ratio, which evaluates response variation in relation to a target or nominal value. Taguchi's studies commonly apply three types of S/N ratios: larger-the-better, smaller-the-better, and nominal-the-best, chosen based on the experiment's objective. Regardless of the quality characteristic being analysed, a higher S/N ratio signifies better performance. Therefore, the optimal experimental condition corresponds to the highest S/N ratio. In our study, the larger-the-better S/N ratio is applied to distortion, while the smaller-the-better S/N ratio is used for ultimate tensile strength as output responses.

The expression for S/N ratio (smaller-the-better) is defined by the equation as follows

$$\text{S/N ratio (smaller-the-better)} = -10log_{10}(\frac{1}{n})[\sum y^2] \quad (2.4)$$

The S/N ratio for (larger-the-better) is expressed as follows

$$\text{SN (larger the better)} = -10\log_{10}\left(\frac{1}{n}\right)\sum_{i=1}^{n}\frac{1}{y^2} \quad (2.5)$$

2.6.4 Analysis of Variance (ANOVA)

ANOVA (Analysis of Variance) is a statistical technique used to identify which process parameters have a significant effect. It examines experimental data to assess the interaction between various factors influencing a specific outcome. By breaking down the total output variability, ANOVA differentiates the effects of individual factors from random errors. This analysis offers crucial insights into how different parameters affect the overall process.

$$SS_T = SS_f + SS_e \quad (2.6)$$

where $SS_T = \sum_{j=1}^{p}\left(\gamma_j - \gamma_m\right)^2$ and SS_T is the total sum of squared deviations about the mean p is number of experiments in the orthogonal array

γ_j mean response for j^{th} experiment

γ_m grand mean of the response

SS_f sum of squared deviations due to each factor

SS_e sum of squared deviations due to error

In ANOVA, the mean square deviation (MSD) is calculated as the sum of squared deviations divided by the degrees of freedom. The F-value, representing Fisher's ratio, is determined by the ratio of the mean square deviation of a specific term to that of the error term. The MSD, Fisher's ratio, and percentage contribution are defined using the following equations:

$$\text{Mean square deviation (MSD)} = \frac{\text{Sum of squres (SS) of the deviations}}{\text{Degrees of freedom (DF)}} \quad (2.7)$$

F is the variance ratio also called Fishers ratio which is defined as

$$F_{\text{calculated}} = \frac{\text{MSD of any term (main or combined effect)}}{\text{MSD for error term}} \quad (2.8)$$

The percentage contribution of each factor can be estimated using the following formula:

$$\text{P \% Contribution} = \frac{SS_f}{SS_T} \quad (2.9)$$

The S/N ratio optimization method can be used to identify the best parameter combination. In an orthogonal experiment, the impact of each parameter at defined levels can be examined separately. ANOVA and response table computations were conducted using commercially available software. In this study optimization of process parameters to reduce abrasive wear in HP40Nb reformer steel. Optimization of material type, sliding speed, and applied load aims to minimize the reduction in specimen weight and coefficient of friction caused by abrasive wear in Polyamide6 and Wollastonite composite materials [44], optimization of milling machining parameters, such as surface roughness and flank wear, for Hadfield steel using PVD- and CVD-coated carbide inserts is studied by researchers [45]. The impact of various factors like load, sliding speed and sliding distance on wear rate of aluminium hybrid composites was studied and optimization of the tribological properties by using Taguchi technique [46] is also available. Taguchi method is an effective tool to design the experiments to optimize the wear parameters or to predict the Abrasive Wear Behavior of different materials [47-51]. When multiple performance characteristics need to be optimized, they can be converted into a single grey relational grade to simplify the process and avoid complications [52, 53]. The Taguchi method, combined with Response Surface Methodology (RSM), has been successfully used to optimize parameters in various processes such as machining, laser machining, and injection moulding [54-58]. The surfaces of engineering materials play a crucial role while analysing the wear mechanism in it. It is studied by analysing the topography of the surface. It has different parameters as follows.

2.7 Surface Topography

Roughness parameters are essential for characterizing wear as they offer numerical insights into a surface's texture, which significantly impacts wear performance [13, 43, 100-102].

2.7.1 Roughness Parameters

Surface roughness significantly impacts wear performance. Therefore, it is an essential parameter for the characterization of wear performance [13, 43, 100-102]. Solid surface properties are crucial in surface interactions, as they impact real contact area, friction, wear, and lubrication. Surface texture refers to the repetitive or random irregularities that deviate from the nominal surface, forming its three-dimensional topography [14]. Surface roughness generally describes the vertical deviations or height variations on a surface when measured against a defined reference plane. It is measured along a single line profile or a series of parallel line profiles. Various roughness parameters are employed to quantify the characteristics of a

surface profile. For instance, Peak-to-Valley Height (R_z) indicates the total height difference across the surface, while Root Mean Square (R_q or *RMS*) reflects the general height variation. Total Roughness (R_t) measures the vertical distance between the highest peak and the deepest valley within a given sampling length. Roughness Average (R_a) represents the arithmetic mean of the absolute height deviations from the mean line over the evaluation length.

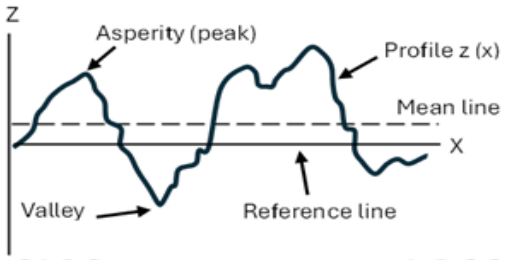

Figure 2.7 Schematic of surface profile Z (X)

The surface profile is generally defined using one of two statistical height descriptors recommended by the American National Standards Institute (ANSI) and the International Organization for Standardization (ISO). These include (1) R_a, *CLA* (centre-line average), or AA (arithmetic average) and (2) the standard deviation or variance (σ), R_q, or root mean square (*RMS*). An alternative method for assessing surface roughness involves using extreme value height descriptors. R_t also known as R_y, R_{max}, maximum peak-to-valley height, or simply P-V distance-indicates the greatest vertical distance between a peak and a valley. R_v measures the maximum depth of a valley from the mean line, R_z represents the average peak-to-valley height, and R_{pm} denotes the average height from the mean line to the peaks [14].

Consider a profile z (x) where profile heights are measured from a reference line (figure 2.5). The centre line or mean line is defined as the line where the area of the profile above it equals the area below it. R_a, *CLA*, or *AA* represents the arithmetic mean of the absolute vertical deviations from the mean line across the profile. The standard deviation σ is the square root of the arithmetic mean of the squared vertical deviations from the mean line [14].

$$R_a = CLA\ (centre\text{-}line\ average) = AA = \frac{1}{L}\int_0^L |z - x|\, dx \qquad (2.10)$$

where L is known as the profile length, represents the sampling length of the profile.
The variance is given as

$$\sigma^2 = \frac{1}{L}\int_0^L (Z - X)^2 dx \qquad (2.11)$$

where σ denotes the standard deviation, and Rq is the square root of the mean of the squared vertical deviations from a reference line.

$$R_q^2 = RMS^2 = \frac{1}{L}\int_0^L z^2\,dx \tag{2.12}$$

In many instances, Ra and σ can be used interchangeably, particularly for Gaussian surfaces,

$$\sigma \sim \sqrt{\frac{\pi}{2}}\,R_a \sim 1.25R_a \tag{2.13}$$

The relationship between wear morphology and peak roughness removal is important while investigating the wear morphology. In engineering, understanding complex wear mechanisms and optimizing surface roughness morphology are crucial. By analysing the surface of stainless steel (SS 304) using various roughness parameters such as R_a, R_p, R_{pk}, R_{pc}, and R_{ku} the pattern of mass loss under abrasive wear conditions was effectively identified. [100].

The literature review is briefed in the following section.

2.8 Summery of literature study

The summary of the literature study reveal major findings in the following table

Table 2.3 Literature review summary

No.	Research Focus	Key Findings	Research Gaps / Relevance to Current Study
1.	Utility of HP40Nb reformer after the service period	The part of the reformer tube exposed to temperature at 650°C has not gone under microstructure degradation even after the service period	The part of HP40Nb reformer can be repurposed as antifiction material instead of salvaging it.
2.	Types of wear in metallic alloys	Impact of different types of wear such as abrasive wear, adhesive wear, fatigue wear, and corrosive wear in industry varies.	The contribution of abrasive and adhesive wear in industry among total wear are dominant as 50% and 15% respectively.
3.	Abrasive wear in metallic components	Effect of different parameters on abrasive wear mechanism on various types of steels.	Abrasive wear behavior of HP40Nb steel under the effect of various parameters such as load, speed, COF, and sliding distance.
4.	Adhesive wear in metallic components	Adhesive wear mechanism. Adhesive wear resistance in different types of steel such as	Adhesive wear behaviour and effect of various parameters on HP40Nb steel.

		structural steels, stainless steel, Hadfield steel, tool steel etc.	
5.	Various techniques to improve wear resistance in metallic components	Different surface treatment techniques utilized to improve the wear resistance of steel such as carburizing, nitriding, boriding, cyaniding, induction hardening, cladding etc.	HP40Nb steel's stable austenitic structure prevents quench hardening, so pack carburization was used to enhance its surface hardness.
6.	Comparison of wear performance of HP40Nb with different materials	Comparison of abrasive and adhesive wear of HP40Nb reformer steel with commercial materials such as SS304 and HSS tool steel.	The effect of pack carburization on wear resistance of HP40Nb in comparison with the materials having high hardness as well as low hardness.

2.9 Research Gap

Based on a literature survey carried out, the following areas have not been addressed or investigated by researchers.

Repurposing potential: The section of the reformer tube that was exposed to a temperature of 650°C has shown no signs of microstructural degradation even after service life. Therefore, the HP40Nb reformer material from this part can be repurposed as an anti-friction material rather than being scrapped. The use of HP40Nb steel for applications other than reformer steel, as wear resistant material has not been explored.

Wear studies: No reports exist on the abrasive or adhesive wear behavior of HP40Nb reformer steel in the available literature. Different types of wear, including abrasive, adhesive, fatigue, and corrosive wear, affect industries to varying degrees. Among these, abrasive and adhesive wear are the most significant, accounting for approximately 50% and 15% of the total industrial wear, respectively.

The abrasive and adhesive wear behaviours of various steels are influenced by several factors such as applied load, sliding speed, coefficient of friction, and sliding distance. Different types of steels, including structural, stainless, Hadfield, and tool steels, exhibit distinct levels of

resistance to adhesive wear due to their compositional and microstructural differences. Understanding these mechanisms and parameter effects is essential for improving wear resistance and extending the service life of steel components. In particular, the effect of these parameters on wear performance of HP40Nb steel is essential to study.

Heat treatment and microstructure: Post-wear and microstructural analyses of HP40Nb reformer steel have not been reported in existing literature. Various surface treatment methods such as carburizing, nitriding, boriding, cyaniding, induction hardening, and cladding are employed to enhance the wear resistance of steel. However, since HP40Nb steel possesses a stable austenitic structure that inhibits quench hardening, pack carburization was adopted to improve its surface hardness.

Comparative performance: No report regarding the comparison of abrasive and adhesive wear of carburized HP40Nb steel with materials of higher hardness (HSS) and lower hardness (SS304) is available. The influence of pack carburization on the wear resistance of HP40Nb was also evaluated relative to materials possessing both higher and lower hardness levels. A comparison was made between the abrasive and adhesive wear behavior of HP40Nb reformer steel and commercial materials such as SS304 and HSS tool steel. The research gaps are briefed as follows

1. No work regarding the abrasive wear of HP40Nb reformer steel has been reported in so far.
2. Adhesive wear of HP40Nb is not seen studied in open literature.
3. Information regarding the heat treated HP40Nb steel has not been reported so far.
4. The use of HP40Nb steel for applications other than reformer steel, as wear resistant material has not been explored.
5. No report regarding the comparison of abrasive and adhesive wear of carburized HP40Nb steel with materials of higher hardness (HSS) and lower hardness (SS304) is available.
6. Post abrasive wear characterization and microstructure investigation on HP40Nb reformer steel are not found in published literature.
7. Post adhesive wear characterization and microstructure investigation on HP40Nb reformer steel are not found in published literature.
8. Comparison of abrasive and adhesive wear of HP40Nb reformer steel with the materials having high hardness as well as low hardness is not available in open literature.

2.10 Objectives of Work

Based on the research gap objectives of the research work are as follows.

1. Experimental investigation on effect of different operating parameters such as load, speed and grit size on abrasive wear and characterization of abrasive wear of HP40Nb reformer steel.
2. Experimental investigation on effect of different operating parameters such as load, speed and sliding distance on adhesive wear and characterization of adhesive wear of HP40Nb reformer steel.
3. Effect of pack carburization on abrasive wear of HP40Nb reformer steel.
4. Effect of pack carburization on adhesive wear of HP40Nb reformer steel.
5. Comparison of abrasive and adhesive wear of HP40Nb reformer steel with other similar materials (HSS and SS304).

This chapter describes the methodology employed to accomplish the objectives of this thesis. It provides a detailed explanation of the experimental procedures, and the techniques used to analyze the results. This consists of (i) experiments performed to analyze the abrasive wear and adhesive wear of as received HP40Nb reformer steel, (ii) characterization of the worn surfaces after wear testing and (ii) abrasive and adhesive wear testing of the samples after carburizing heat treatment followed by characterization of the worn surface. The following subsections provide a comprehensive account of the procedures undertaken.

3.1 Experimental Procedures

3.1.1 Material

The reformer tubes used was centrifugally cast HP40Nb micro-alloyed austenitic stainless steel obtained from Numaligarh Refineries Limited, Assam, India. The supplied material was in the form of a tube with a thickness of 15.3 mm and an inside diameter of 106 mm. The part of the tube supplied had been exposed to high temperatures up to 650°C for 11 years. Manufactured by Doncasters Paralloy Limited, England, using centrifugal casting, the reformer tube was utilized for hydrogen generation. The chemical composition of the steel is as shown in Table 3.1.

Table 3.1 Chemical composition (in wt., %) of reformer steel

C	Si	Mo	Cr	Ni	Nb	Ti	Fe
0.4 %	1.3 %	0.037 %	23.6 %	34.9 %	0.8 %	0.037 %	Bal.

3.1.2 Metallographic Sample Preparation

Microstructural analysis specimens were prepared following standard metallographic procedures. A transverse section of the reformer tube was cut using wire-cut electrical discharge machining (WEDM). The 5 mm thick sliced specimen was mounted in thermosetting resin using a hot mounting press (Buehler Simplimet-2) at 20.7 MPa pressure and 150°C. Polishing was carried out with a grinder/polishing machine (Buehler Ecomet-6), using SiC-coated polishing discs with grit sizes 240, 320, 600, 1000, and 1500, while water served as the lubricant. Further cloth polishing was performed with a 0.5 µm alumina suspension in distilled

water at a disc speed of 120 rpm. Finally, the polished specimens were ultrasonically cleaned in acetone for 5 minutes, dried, and preserved in a vacuum desiccator.

3.1.3 Optical Microscopy

The samples, which were polished metallographically, were etched using a freshly prepared glyceregia solution consisting of 10 ml glycerol, 15 ml HCl, and 5 ml HNO_3. After etching, the samples were rinsed with running water and dried. The etched specimens were then examined under an upright optical microscope (Model: Axiotech, Make: Carl Zeiss) with monochromatic light. Digital images of the microstructures were captured and analysed using Axio Vision Rel.4.2 software.

3.1.4 Scanning Electron Microscopy

The unetched polished samples were gold-coated using a plasma sputter coater prior to analysis with a scanning electron microscope (SEM) (Model: LEO 1430 VP) and a field emission scanning electron microscope (FESEM) (Zeiss Sigma). Secondary electron (SE) detection was employed for imaging, with most SEM observations conducted at accelerating voltages of 10-20 kV and a working distance of 15 mm. The composition of the different phases in the matrix was analysed using an energy dispersive X-ray spectroscope (EDX) (Oxford INCA X-Sight), integrated with the electron microscopes. Quantitative phase analysis was performed using high-purity cobalt as the reference standard, while X-ray elemental mapping was used to assess the qualitative distribution of elements across specific areas of the specimen.

3.1.5 X-ray Diffraction

X-ray diffraction (XRD) was used to analyze the crystal structure of the steel and the different phases present. The samples measuring 6mm diameter and 3 mm height were sectioned using wire electrical discharge machining (WEDM) and cleaned with acetone. XRD analysis was performed on (i) the as-received sample and (ii) the sample after carburization heat treatment. For the carburized condition, the sample underwent pack carburization at 950 °C for 19.07 hours in a muffle furnace, followed by air cooling to room temperature. Before XRD analysis, the samples were polished using standard metallographic techniques. The XRD pattern was

recorded over a 2θ range of 30°–80°. The phases present were identified by comparing peak positions and intensities with the JCPDS database.

3.2 Abrasive Wear Testing

HP40Nb cylindrical specimens 50 pin samples (ϕ 6 mm, length 30 mm) were cut from the as-received HP40Nb pipe by using WEDM. It were thoroughly cleaned with acetone before and after the wear test. The weight of specimen pin before and after the experiment was measured by digital weight balance of accuracy 0.0001 g. Dry sliding wear tests were conducted using a pin-on-disc machine (Wear and Friction Monitor Tester, Model TR-201 by M/S DUCOM, Bangalore, India) Fig.3 (d) as per ASTM G99 standard. The experiments were conducted under dry sliding condition at normal temperature in atmospheric air. Few sample photos of wear tracks are as shown in Figure 3.1 (a), (b) and (c) formed by silicon carbide papers of grit size 600G, 320G and 400G respectively.

(a) (b) (c)

Figure 3.1 Wear tracks formed by carburised HP40Nb pin samples by (a)15N 150RPM 600G (b) 320G150RPM 20N (c) 400G15N 250RPM

The abrasive wear were studied by using different roughness for the disc surface by pasting silicon carbide abrasive paper of different grit sizes. Subjecting the stationary pin to abrade against the abrasive disc simulates a two-body abrasive environment. The different operating parameters employed during the tests are disc speed (150 RPM, 200 RPM and 250 RPM), normal load (10 N, 15 N and 20 N) and silicon carbide grit papers (grit size 320G, 400G and 600G). Experiments were carried out for a fixed sliding distance of 1000 m.

3.2.1 Design of Experiments

The Taguchi technique is employed to design the experiments for abrasive wear study. Three parameters each of level 3 have been selected. Grit size (A), Load (B) and Disc speed (C) are

the 3 parameters assigned as per their levels taken as shown in Table 3.2. The L_{27} orthogonal array was selected i.e. 27 rows and 13 columns.

Table 3.2 Parameters and levels

Level	Silicon carbide Paper Grit size (A)	Load (N) (B)	Disc speed (RPM) (C)
1	600G	10	150
2	400G	15	200
3	320G	20	250

The experiment has 27 tests, i.e. each row in the L_{27} orthogonal array, and the specific parameters are assigned to the columns.

3.2.2 Understanding the Columns and Parameters

- **L27 (3^{13}) Orthogonal Array**: This array is typically used for 3-level factors, meaning each parameter (factor) can have three different levels (e.g., low, medium, high).
- **Columns 1-13**: Each column represents an experimental factor or interaction.

Parameters Assigned: The parameters are assigned as shown in table 3.3.

Table 3.3 Column wise Parameters and interactions

Column no.	1	2	3	4	5	6	7	8	9	10	11	12	13
Parameter	A	B	AB	AB^2	C	AC	AC^2	BC	BC^2	D	E	F	G

Table 3.4 Explanation column wise parameters and their allocation

Column No.	Factor Assigned	Explanation
1.	A	Main factor Grit Size (A)
2.	B	Main factor Load (B)
3.	AB	Interaction between Grit Size (A) and Load (B)
4.	AB^2	Second order interaction between Grit Size (A) and Load (B)
5.	C	Main factor Speed (C)
6.	AC	Interaction between Grit Size (A) and Speed (C)
7.	AC^2	Second order interaction between Grit Size (A) and Speed (C)
8.	BC	Interaction between Load (B) and Speed (C)
9.	BC^2	Second order interaction between Load (B) and Speed (C)
10.	D	Main factor Wt. loss (mg) (D)
11.	E	Main factor k_s (mm^3/Nm) (E)
12.	F	Main factor COF (F)
13.	G	Main factor R_a (μm) (G)

Main factors in the experiment are assigned as A, B, C, D, E, F, G whereas interaction terms are AB, AB^2, AC, AC^2, BC, BC^2 which are (e.g., the combined effect of two factors). The first, second, the fifth column is designated as A, B and C is allocated to Grit type, Load, and RPM respectively with the other columns allocated to their interactions. Whereas, D, E, F, G are assigned as Wt. loss (mg), k_s (mm^3/Nm), COF and Ra (μm) respectively. Further detailed explanation is given below as per the table 3.3 above.

3.3 Adhesive Wear

Wear testing was conducted by pin-on-disc wear testing setup Fig. 3.1 (d) and schematic of the same in Fig. 3.1 (e). The pins used were made up of HP40Nb SS and discs for these tests were made of SS 316. The chemical composition of the steel is shown in Table 3.5.

Table 3.5 Chemical Composition (in wt.%) of pin (HP40Nb SS) and disc (SS 316)

Pin: HP40Nb Reformer steel	C	Si	Mo	Cr	Ni	Nb	Ti	Fe
	0.40	1.30	0.037	23.6	34.9	0.8	0.037	Bal.
Disc: SS 316	C	Si	Mn	Cr	Ni	P	S	Fe
	0.08	1.00	2.00	16.00	18.00	0.045	0.03	Bal.

The pin was cylindrical specimens (50 pin samples) of 30 mm length × 6 mm diameter, prepared by wire cut EDM machine and few samples are shown in Figure 3.1(a)and schematic of pin in figure 3.2 (b). 20 Discs of 316 austenitic stainless steel diameter 100 mm and 10 mm thickness, prepared by LASER cutting and few samples are shown in Figure 3.2(c).

The disc surfaces were machined to obtain a smooth surface. Finally, both pin and discs were polished to get an average roughness in the range of 0.4 to 0.6 μm. The experiments were conducted on the same friction and wear testing machine. The specimens were cleaned with acetone before and after the wear test. The details regarding the test parameters are shown in Table 3.6. The pin was placed at locations corresponding to a wear track diameter of 60 mm and experiments were conducted for a sliding distance of 1000 m.

Experiments were carried out for different combinations of disc rotational speeds and loads as presented in Table 3.6. After each 250 m of sliding distance, the experiment was stopped to determine the weight loss on the pin during sliding for the 250 m and then the experiments were further continued. The weight of the specimen pin before and after the experiment was measured by the digital weighing balance with an accuracy of 0.0001 g. Each

experiment was repeated 3 times, and the average was taken. During the experiment, the digital data of the COF was continuously captured and plotted vs sliding time. The experiments were carried out at ambient temperature.

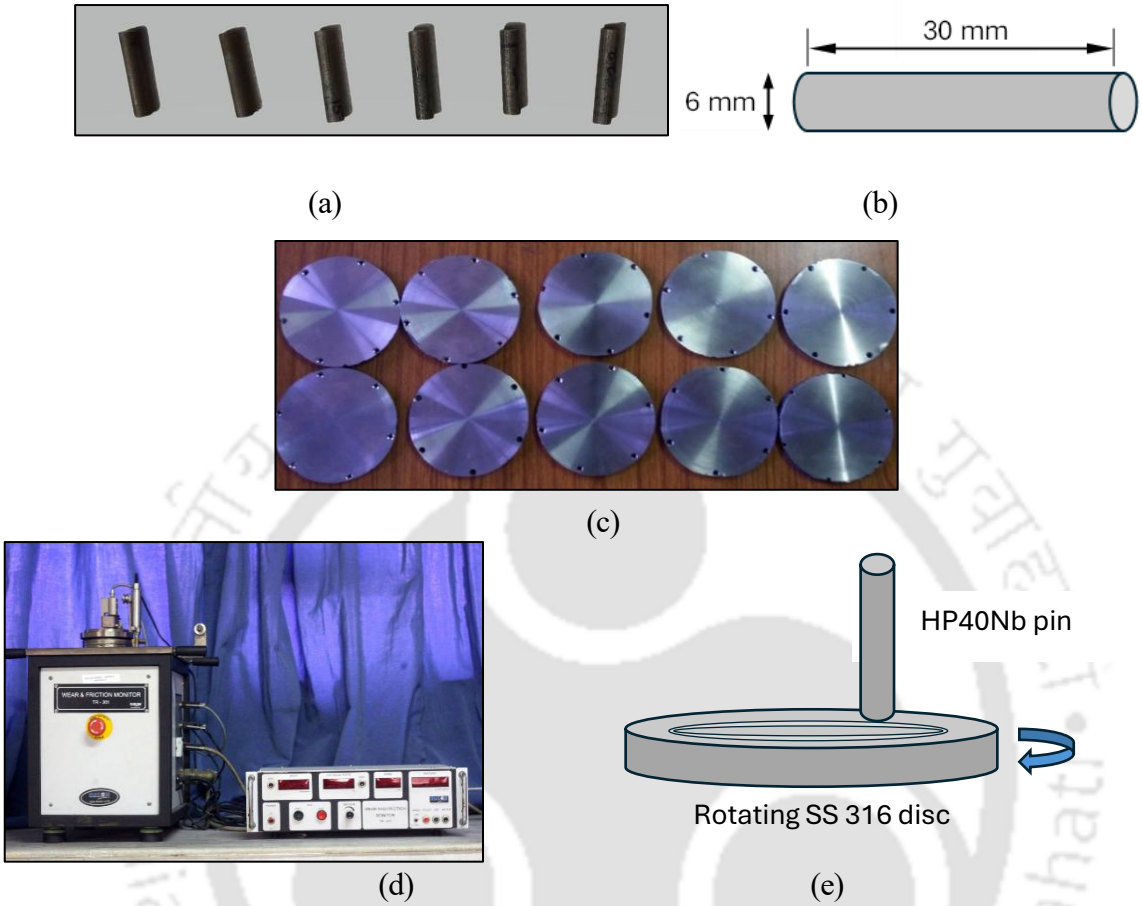

Figure 3.2 (a) Specimen HP40Nb pin, (b) schematic of pin samples (c) disc SS 316 samples and (d) friction and wear tester (TR-201) (e) Schematic of pin on disc set up

Table 3.6 Process parameters adhesive wear testing

Sl. No.	Process Parameters	Specifications
1	Wear disc diameter (mm)	100
2	Temperature	Ambient
3	Wear track diameter (mm)	60
4	Sliding distance, d (m)	1000
5	Pin diameter⌀length (mm)	6mm⌀30mm
6	HP40Nb Pin Hardness (VHN)	257.4 ± 2
7	Hardness of SS 316 Disc (VHN)	208 ± 8
8	Disc rotation speed (RPM)	150, 200, 250, 300
9	Load (N)	5, 10, 15, 20

The design of experiments was performed using general full factorial technique. For conducting the experiments, the 2 parameters such as load of 4 levels and RPM of 4 levels were chosen. Each experiment is repeated 3 times, and average of reading is calculated.

3.4 Surface Hardening

Austenitic stainless steel being a single-phase austenitic alloy, cannot be hardened by quenching. Therefore, pack carburizing heat treatment was carried out to improve the hardness and wear resistance. The HP40Nb 120 pin samples for carburizing were surrounded by the carburizing mixture and packed inside a 145 × 80 × 80 mm sized closed steel box as shown in Figure 3.3.

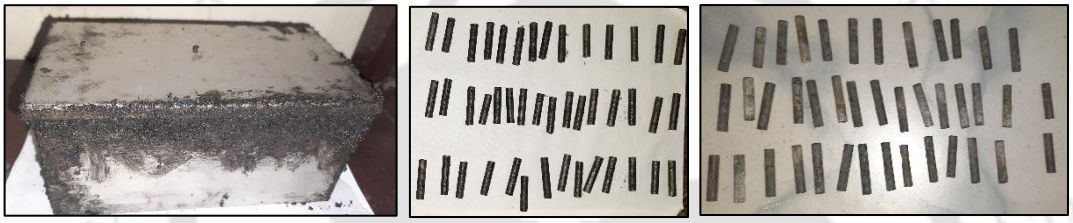

(a) (b) (c)

Figure 3.3 (a) Stainless steel Box 1.5 mm thickness (b) HP40Nb pin samples (before heat treatment) (c) HP40Nb pin samples (after heat treatment)

The carburizing mixture consist of 70% activated charcoal (as a carbon source), 20% $BaCO_3$ (as the energizer), and 10% NaCl (as an activator). The carburizing was carried out at 950°C for 19.07 hrs in a muffle furnace, followed by air cooling to room temperature.

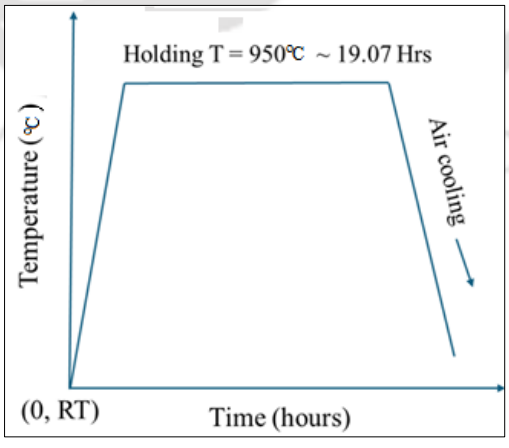

Figure 3.4 Carburization process

Figure 3.4 illustrates the heat treatment cycle followed in the present investigation. The temperature and soaking time for the carburization heat treatment was determined by solving Fick's second law of mass transfer, by applying necessary boundary conditions.

The heat treatment temperature and soaking time for the heat treatment was determined by solving the Fick's second law,

$$\frac{\partial C}{\partial t} = D\frac{\partial^2 C}{\partial x^2} \quad (3.1)$$

where C= carbon concentration, D is the diffusion coefficient, and x is the distance from the surface,

The boundary conditions are: $t = 950^oC$

At $t = 0$, $C = Co$ at $0 \leq x \leq \infty$

For $t > 0$, $C = Cs$ at $x = 0$. It is assumed that

$C_s = 1.2\%$ C

$C_o = 0.4$ % C,

$C_x = 0.8$ % to achieve, $x = 1$ mm $T = 19.0757$ h

In the following subsections the experimental design adopted after the pack carburization heat treatment is explained.

3.5 Design of Experiments for Wear Testing of Post Carburized Specimens

The abrasive and adhesive wear experiments were conducted as follows.

3.5.1 Abrasive Wear

Abrasive wear experiments on the carburized reformer steel specimens were carried out using the pin on disc set up. The design of experiments was performed using full factorial technique.

Table 3.7 Process parameters abrasive wear testing after carburization heat treatment

Sl. No.	Process Parameters	Specifications
		Abrasive Wear
1.	Wear Disc Diameter	100 mm
2.	Disc Rotation Speed	150, 200, and 250 RPM
3.	Temperature	Ambient
4.	Wear Track Diameter	60 mm
5.	Load	10 and 20 N
6.	Grit Size	320 G, 400 G, and 600 G
7.	Sliding Distance (d)	1000 m
8.	Pin Diameter ϕ /length (mm)	ϕ 6 mm, 30 mm

3 parameters such as Grit size of 3 levels, load of 2 levels and RPM of 3 levels were chosen. The process parameters are chosen as shown in Table 3.7. The effect of parameters on abrasive

wear, coefficient of friction and surface roughness is studied. The surface topography and morphology of the wear sample were studied by using profilometer as well as optical microscope.

3.5.2 Adhesive Wear

Adhesive wear analysis, design of experiments was done by using full factorial technique. For conducting the experiments, the 2 parameters such as load of 3 levels and RPM of 4 levels were chosen. The process parameters are chosen as shown in Table 3.8.

Effect of different operating parameters such as disc speed (150 RPM, 200 RPM, and 250 RPM), normal load (10 N, and 20 N), a fixed sliding distance 1000 m. were studied on HP40Nb pin sample against the SS316 disc.

The experiment was stopped after every 250-meter travel distance and the weight low was measured. Subsequently, the experiments were continued under the same conditions till a total of 1250 m. The specimen was thoroughly cleaned with acetone before and after the wear test. The weight of specimen pin before and after the experiment was measured by digital weighing balance having an accuracy of 0.0001 g. Each experiment was repeated 3 times, and the average is taken. The disc surfaces were machined and polished again for another sets of experiments.

Table 3.8 Process parameters adhesive wear testing after carburization heat treatment

	Process Parameters	**Adhesive wear**
1.	Wear Disc Diameter	100 mm
2.	Disc Rotation speed	150, 200, 250, 300 RPM
3.	Temperature	Ambient
4.	Wear Track Diameter	60 mm
5.	Load	10 N, 15 N, 20 N
6.	Counter surface	SS 316 Disc 100 mm diameter, 10 mm thick
7.	Sliding distance (d)	1000 m
8	Pin DiameterØ/length (mm)	6 mm Ø/30 mm

$$\text{Sliding speed (m/s)} = \frac{D \times N}{60000} \tag{3.2}$$

$$\text{Sliding distance in meter, } d = \frac{\pi DNT}{60000} \tag{3.3}$$

where D = Diameter of track in mm, N = Disc speed in RPM, T = test time in seconds

The wear was measured by the loss in weight, which was then converted into wear volume using the measured density.

Density of HP40Nb steel, ρ = 7709 kg.m^{-3} = 0.007709 g.mm^{-3}

Cross-sectional area of pin, $A = \pi r^2$ (3.4)

Volume loss of pin, $\Delta V = cross\ sectional\ area\ (pin) \times height\ loss$ (3.5)

Specific wear rate (k_s)= $\frac{Wear\ rate}{load}$ = $\frac{Weight\ loss\ in\ gram}{sliding\ distance \times load \times density}$

$= \frac{\Delta m}{\rho L d}$ (3.6)

where Δm is the weight loss (g), L is the applied normal load (N), and d is the sliding distance (m)

The wear rate (k) calculated from the equation:

$k = \frac{\Delta V}{d}$ mm^3/m = $\frac{\Delta m}{\rho \times d}$ (3.7)

where ΔV is the wear volume loss (mm^3),

Coefficient of friction is calculated by $\mu = \frac{F}{N}$ (3.8)

where F = frictional force (N), N = Normal reaction)

The surface roughness was determined using high precision non-contact computerised surface profilometer (Make: Taylor Hobson, Model: Talysurf CCI lite.). Surface profilometry across the pin surface was used to assess the wear mechanism. The surface topography of the wear (disc) sample was investigated using stereo zoom microscope (Make: NIKON). Composition analysis of the worn pin surface was studied using FESEM/EDS system. Adhesive wear rate was calculated for every 250 m sliding distance; total wear rate is calculated for up to 1250 m of sliding distance.

3.6 Hardness Measurement

The hardness measurement of samples was done in the following ways:

a) Before carburization: The Vickers hardness of disc and pin samples were determined by applying a load of 30 N. The average of five readings for the HP40Nb pin and 316 SS disc are 257.4 ± 24 VHN and 208 ± 8 VHN, respectively.

b) After Carburization: The post carburised HP40Nb samples were analysed for hardness using a Vickers microhardness tester (make: Omni Tech) with a diamond indenter (136° included

angle). The constant load of 300 gram was applied for a time period of 20 seconds. The Vickers hardness (HV) was determined using the following relation.

$$HV = \frac{1.584F}{D^2} \tag{3.9}$$

where D is the arithmetic mean of the two diagonal lengths of the indentation in mm and F is the load applied in kilogram. The readings were taken radially from the circumference of the pin specimen to the centre at regular intervals. The hardness values of the carburised HP40Nb samples were obtained by taking average of minimum 9 individual readings. The results are plot then in order to analyse the variation of hardness from the circumference to the core of the pin specimen.

3.7 Comparison of Wear

In order to compare the wear resistance of HP40Nb reformer steel, Abrasive and Adhesive wear tests were carried out on the standard HSS and SS304 pin samples. The process parameters for the abrasive and adhesive wear testing are discussed in the following section. The pin samples used for these experiments were carburised HP40Nb pin samples.

The measured density of high speed steel: 0.00781 g/mm^3

The measured density of SS 304: 0.007350 g/mm^3

3.7.1 Abrasive Wear

The HSS and SS304 pin was EDM wire cut of 30 mm length and 6mm diameter. Total wear rate is calculated for 1000 m of sliding distance. The weight of specimen pin before and after the experiment was measured by digital weight balance of accuracy 0.0001 g.

Table 3.9 Process parameters for Abrasive wear of (HSS and SS304)

Sl. No.	Process Parameters	Specifications
1.	Wear Disc Diameter	100 mm
2.	Disc Rotation speed	100, 250 RPM
3.	Temperature	Ambient
4.	Wear Track Diameter	60 mm
5.	Load	10N, 20 N
6.	Grit size	320G, 400G, 600G
7.	Sliding distance	1000 m
8.	Pin Diameter	6 mm ϕ, 30 mm

The experiments were conducted similar as explained in section 3.2. Each experiment was repeated for 3 times, and the average is taken. The process parameters are selected as shown in Table 3.9.

3.7.2 Adhesive Wear

Table 3.10 shows the process parameters used for comparison of wear experiments.

Table 3.10 Process parameters Adhesive wear (HSS and SS 304)

Sl. No.	Process Parameters	Specifications
1.	Wear Disc Diameter	100 mm
2.	Disc Rotation speed	150, 250 RPM
3.	Temperature	Ambient
4.	Wear Track Diameter	60 mm
5.	Load	10N, 20 N
6.	Sliding distance (d)	1000 m
7.	Pin Diameter	6 mm ϕ, 30 mm

The adhesive wear testing the pin samples were made from HSS and SS304 EDM wire cut of 30mm length and 6 mm diameter. The disc specimen used was made up of SS316. The specimen preparation was similar to that of done for adhesive wear of HP40Nb SS. Total wear rate is calculated for 1000 m of sliding distance. The experiments were conducted similar as explained in section 3.2. Each experiment was repeated for 3 times, and the average is taken.

3.8 Summary of chapter 3

In this chapter the methodology adapted for the complete work is explained. The abrasive and adhesive wear resistance of as received HP40Nb steel is compared with the carburised heat treated HP40Nb steel. For each of the case surface morphology, topography is also compared for the as received material with carburised heat treated worn surfaces. The various modes of both abrasive and adhesive wear are studied by examining the worn surfaces under various microscopes. In order to compare the wear resistance with the standard material, the abrasive and adhesive wear test were conducted on SS304 and HSS pin samples. A set of experiments by selecting parameters carefully was conducted for both the materials.

.

Chapter 4

Abrasive Wear Behaviour of HP40Nb SS

In this section the results obtained from the Abrasive wear tests are presented and discussed. This involves the following. Taguchi analysis and ANOVA of abrasive wear of as-received HP40Nb steel and is presented in two parts: (i) the effect of each parameter on abrasive wear and (ii) interaction between the parameters on the abrasive wear. The results of the microscopic analysis by OM, SEM/EDS and the surface characteristics of the worn surfaces, investigated by digital profilometer, has been presented and discussed in the subsequent sub-sections.

4.1 Abrasive Wear

4.1.1 Wear Test Results and Taguchi Analysis

A statistical analysis of variance (ANOVA) was conducted along with the Taguchi technique to find the contribution of each of the process parameter such as grit size, load and speed on the wear loss, specific wear rate, COF and surface roughness, respectively. The percentage contribution of various process parameters for selected performance characteristic is estimated by ANOVA. To obtain the contribution of parameters, ANOVA was performed for each parameter separately in first phase; secondly, it was done to find out the contribution of parameters along with their interaction.

Table 4.1 depicts the responses obtained for the 27 experiments of the Taguchi DOE. Considering the three levels of the input parameters viz, load, grit and speed mentioned in Table 3.2, the signal-to-noise (S/N) ratio was determined for responses like wt. loss (*ks*) specific wear rate (k_s), coefficient of friction (COF) and roughness (R_a). The S/N ratios were determined using the equation (2.4) in MINITAB software with "smaller is better" option.

Table 4.2 shows the mean weight loss and S/N ratio for the 27 experiments [102]. Figure 4.1 shows the plots of S/N ratios and the mean weight loss for each factor against each of its levels with the "smaller is better" condition for wt. loss., COF and R_a. The greater the S/N ratio, the smaller the variance of weight loss (k), wear rate (k_s), coefficient of friction (COF) and surface roughness (R_a) around the desired value. Optimal testing conditions of these control factors could be very easily determined from the response graphs. The minimum weight loss, wear rate, coefficient of friction and surface roughness were at the higher S/N values in the response graphs.

Table 4.1 Input and output parameters

parameters	A	B	C	D	E	F	G				
Expt. No.	Grit	Load	Speed	Wt. loss k (mg)	k_s ($\times 10^{-3}$) mm^3/Nm	Avg. COF	R_a (µm)	S/N (k)	S/N (k_s)	S/N (Avg. COF)	S/N (R_a)
1.	3	2	1	0.2012	1.74	0.45	0.58	13.93	55.19	6.94	4.73
2.	1	1	2	0.0057	0.07	0.54	0.41	44.88	82.63	5.35	7.79
3.	1	3	2	0.0100	0.06	0.36	0.26	40.00	83.76	8.87	11.67
4.	3	2	3	0.2039	1.76	0.6	0.68	13.81	55.07	4.44	3.34
5.	3	3	2	0.2244	1.46	0.45	0.78	12.98	56.74	6.94	2.15
6.	2	2	1	0.0184	0.16	0.44	0.45	34.70	75.97	7.13	7.03
7.	3	1	2	0.1690	2.19	0.65	0.67	15.44	53.18	3.74	3.43
8.	3	1	1	0.1790	2.32	0.61	0.61	14.94	52.68	4.29	4.32
9.	3	1	3	0.1857	2.41	0.66	0.69	14.62	52.36	3.61	3.24
10.	1	1	3	0.0047	0.06	0.54	0.43	46.56	84.29	5.35	7.35
11.	2	2	2	0.0415	0.36	0.48	0.47	27.64	68.90	6.38	6.54
12.	1	3	3	0.0127	0.08	0.42	0.31	37.92	81.68	7.54	10.17
13.	1	1	1	0.0040	0.03	0.38	0.27	47.96	85.70	8.40	11.37
14.	2	3	3	0.0899	0.58	0.48	0.46	20.92	64.69	6.38	6.82
15.	2	1	2	0.0163	0.21	0.53	0.46	35.76	73.50	5.51	6.71
16.	2	1	3	0.0419	0.54	0.55	0.47	27.56	65.30	5.19	6.60
17.	2	3	1	0.0332	0.22	0.39	0.29	29.58	73.34	8.18	10.72
18.	2	3	2	0.0626	0.41	0.47	0.42	24.07	67.83	6.56	7.56
19.	1	2	2	0.0086	0.07	0.37	0.40	41.31	82.57	8.64	7.89
20.	3	3	3	0.2334	1.51	0.62	0.62	12.64	56.40	4.15	4.10
21.	1	3	1	0.0135	0.09	0.34	0.32	37.39	81.15	9.37	9.82
22.	1	2	1	0.0225	0.19	0.36	0.25	32.96	74.22	8.87	12.22
23.	2	1	1	0.0109	0.14	0.56	0.42	39.25	76.99	5.04	7.58
24.	3	3	1	0.2154	1.40	0.46	0.77	13.34	57.10	6.74	2.30
25.	3	2	2	0.1841	1.59	0.54	0.65	14.70	55.96	5.35	3.74
26.	2	2	3	0.0628	0.54	0.56	0.44	24.04	65.30	5.04	7.07
27.	1	2	3	0.0073	0.09	0.5	0.31	42.73	84.00	6.02	10.23

The parameters A1-B1-C1shows the highest S/N ratios, i.e. for lowest grit size, lowest load and lowest speed for both wt. loss and *k*. However, the S/N ratio for the COF is highest for the combination A1-B3-C1, i.e. for lowest grit size, highest load and lowest speed. However, the highest S/N ratio for the surface roughness is for the combination of parameters A1-B2-C1.

4.1.2 Analysis of Wt. Loss vs Grit, Load, Speed

(a) S/N Ratio Analysis

The responses of means and S/N ratio for the wt. loss over the grit, load, speed is as shown in Table 4.2. It is observed from Table 4.3 that, grit size has the strongest influence on weight

loss due to wear, followed by applied load and speed. The details about the theoretical background of Table 4.2 is as chapter 2 section 2.6.3 and 2.6.4.

The main effect plot and S/N ratio, based on table 4.2, (smaller is better eq. 2.4) plot for the wt. loss are as shown in figure 4.1 (a) (b), respectively. The plot shows influence by grit size, applied load and speed, respectively on weight loss due to wear which is in line with the response Table 4.3.

Table 4.2 Response Table: wt. loss versus Grit, Load and Speed

Response table for means			
Level	**Grit**	**Load**	**Speed**
1	0.009889	0.068578	0.077567
2	0.041944	0.083367	0.080244
3	0.199567	0.099456	0.093589
Delta	0.189678	0.030878	0.016022
Rank	1	2	3
(a)			

S/N ratios (smaller is better condition)			
Level	**Grit**	**Load**	**Speed**
1	41.30	31.89	29.34
2	29.38	27.31	28.53
3	14.04	25.43	26.76
Delta	27.26	6.46	2.58
Rank	1	2	3
(b)			

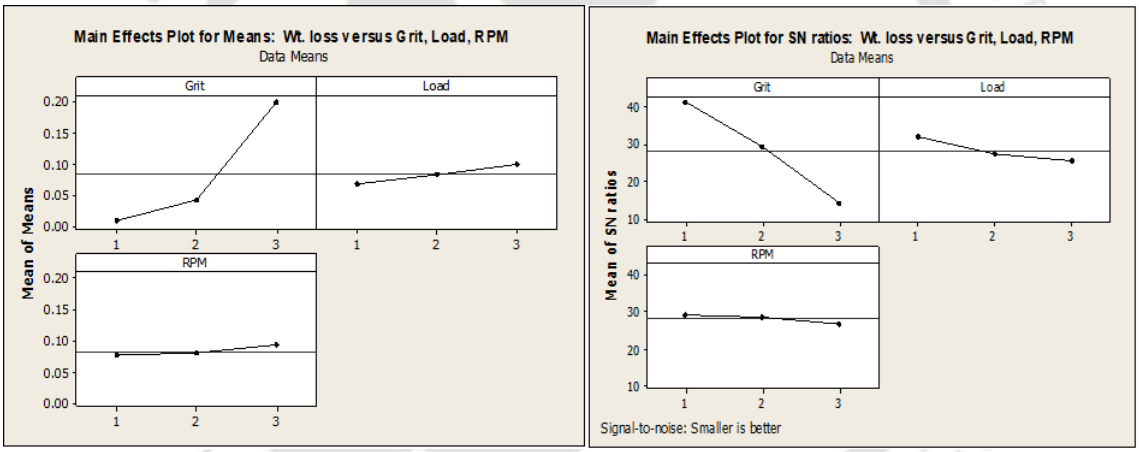

Figure 4.1 Main effects plots of (a) means and (b) S/N ratios, Wt. Loss versus Grit, Load and Speed

(b) ANOVA and Regression Analysis

The results of the ANOVA analysis carried out for a confidence level of 95% is shown in Table 4.3. Parameters with a p-value < 0.05 has statistically significant contribution to the performance measures. Table 4.3 shows the percentage contribution of each parameter. The Grit size have the highest contribution of 95.12% followed by load 2.20%. Speed has the lowest contribution and has a p value more than 0.05. From the F values also, it is confirmed that grit size has a very influential effect on wt. loss, whereas load has much less influence compared to grit size and speed has negligible effect on wt. loss.

Table 4.3 Analysis of variance for wt. loss

Source	DF	Seq SS	Adj SS	Adj MS	F	P	P % (Contribution)
Grit	2	0.185550	0.185550	0.092775	477.64	0.000	95.12
Load	2	0.004293	0.004293	0.002099	10.28	0.001	2.20
Speed	2	0.001326	0.001326	0.000663	2.99	0.053	0.68
Error	20	0.003885	0.003885	0.000194			2.00
Total	26	0.195054					100
S = 0.0139369 R-Sq = 98.01% R-Sq (adj) = 97.41%							

DF: degrees of freedom; Seq SS: sequential sum of squares; Adj SS: adjusted sum of squares; Adj MS: adjusted mean squares

Regression Analysis for wt. loss versus Grit, Load, Speed

To establish the correlation between the wear parameters, viz, grit, sliding distance, load and speed with the wear loss, regression equation was developed. Equation (4.1) shows the correlation between the wear parameters and wt. loss due to wear.

$$k = -0.153 + 0.0948 \times (A) + 0.0154 \times (B) + 0.00801 \times (C) \quad (4.1)$$

4.1.2.1 ANOVA and Regression Analysis with Interaction in Between Parameters for wt. Loss

(a) The ANOVA for weight loss, using Adjusted SS for tests is as shown in Table 4.4.

Table 4.4 Analysis of interactions for wt. loss

Source	DF	Seq SS	Adj SS	Adj MS	F	P	P% (Contribution)
Grit	2	0.188491	0.188491	0.094246	1073.82	0.000	94.69
Load	2	0.005436	0.005436	0.002718	30.97	0.000	2.73
Grit×Load	2	0.000522	0.000522	0.000261	2.97	0.108	0.26
Grit×Load×Load	2	0.001296	0.001296	0.000648	7.38	0.015	0.65
Speed	2	0.000741	0.000741	0.000371	4.22	0.056	0.37
Grit×Speed	2	0.000255	0.000255	0.000128	1.45	0.289	0.13
Grit×Speed×Speed	2	0.001009	0.001009	0.000504	5.75	0.028	0.51
Load×Speed	2	0.000397	0.000397	0.000199	2.26	0.166	0.20
Load×Speed×Speed	2	0.000212	0.000212	0.000106	1.21	0.349	0.12
Error	8	0.000702	0.000702	0.000088			0.35
Total	26	0.199061					100
S = 0.00936841 R-Sq = 99.65% R-Sq (adj) = 98.85%							

DF: degrees of freedom; Seq SS: sequential sum of squares; Adj SS: adjusted sum of squares; Adj MS: adjusted mean squares.

The percentage contribution of each parameter including interaction is as shown in the last column of the table. The most significant parameter is Grit size, followed by Load, Grit × Load × Load, Grit × Speed × Speed and Speed respectively.

The influence of interactions between control factors is shown in the Figure 4.2. Analysis of interactions between control factors provides significant information about the nature of the process under consideration. It can be seen that there is interaction between grit size and load as well as between grit size and speed.

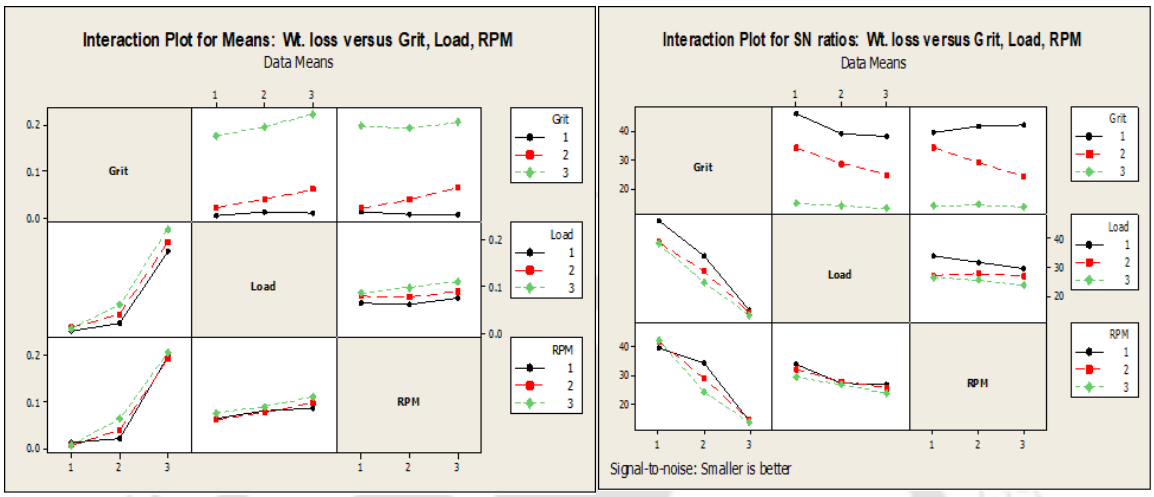

(a) (b)

Figure 4.2 Interaction plots, wt. loss versus Grit, Load and Speed of (a) means and (b) S/N ratios

(b) Regression Analysis:

Regression analysis was done to find out the relation among the parameters as well the interaction between the parameters. The regression equation is as given in equation no.4.2.

$$k = -0.107 + 0.0948 \times (\mathrm{A}) + 0.0174 \times (\mathrm{B}) - 0.00537 \times (\mathrm{A} \times \mathrm{B}) - 0.00836 \times (A \times \mathrm{B} \times \mathrm{B}) + 0.00611 \times (C) - 0.00203 \times (\mathrm{A} \times \mathrm{C} \times \mathrm{C}) - 0.00396 \times (\mathrm{B} \times \mathrm{C}) + 0.00286 \times (\mathrm{B} \times \mathrm{C} \times \mathrm{C}) \quad (4.2)$$

4.1.3 Analysis of Coefficient of Friction vs. Grit, Load, Speed

(a) S/N Ratio Analysis

The response table for the means and S/N ratio on Avg. coefficient of friction versus Grit, Load, Speed are as shown in Table 4.5.

Table 4.5 Response table avg. COF versus Grit, Load, Speed

Signal to Noise Ratios (Smaller is better)			
Level	Grit	Load	Speed
1	7.602	5.166	7.219
2	6.155	6.533	6.371
3	5.134	7.192	5.301
Delta	2.469	2.025	1.918
Rank	1	2	3

(a)

Response Table for Means			
Level	Grit	Load	Speed
1	0.4233	0.5578	0.4433
2	0.4956	0.4778	0.4878
3	0.5600	0.4433	0.5478
Delta	0.1367	0.1144	0.1044
Rank	1	2	3

(b)

As per the rank obtained, the most influential parameter is grit size followed by load and speed respectively.

The Main effects plots of means and S/N ratios for Avg. COF versus grit, load and speed is as shown in figure 4.3. The highest S/N ratio is for the lowest level of grit as well as for speed, whereas is highest for highest level of load.

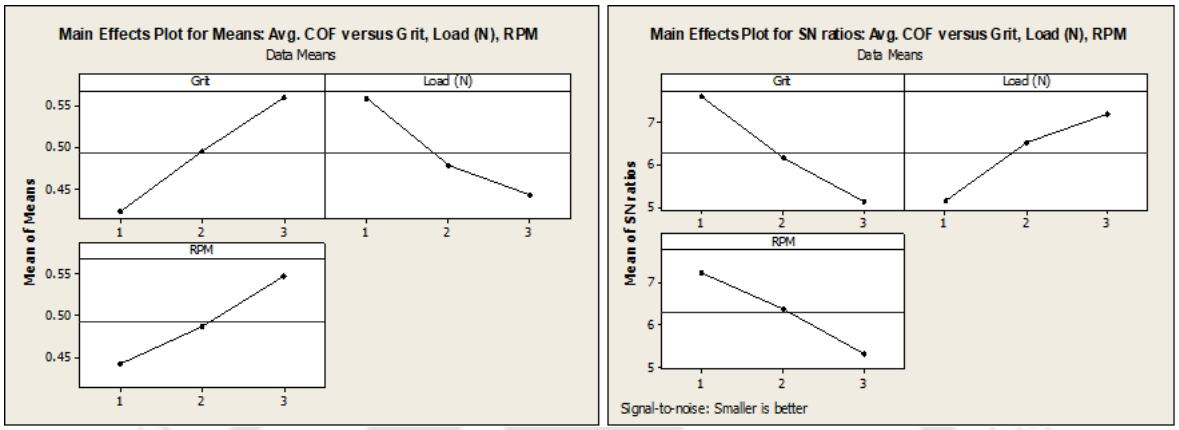

Figure 4.3 Main effects plots of means and S/N ratios: Avg. COF versus Grit, Load, Speed

(b) ANOVA and Regression Analysis: Coefficient of Friction vs. Grit, Load & Speed

The analysis of variance results is as shown in Table 4.8.

Table 4.6 Analysis of Variance for avg. COF

Source	DF	Seq SS	Adj SS	Adj MS	F	P	P% (Contribution)
Grit	2	0.084141	0.084141	0.042070	28.50	0.000	37.38
Load	2	0.062052	0.062052	0.031026	21.02	0.000	27.50
Speed	2	0.049452	0.049452	0.024726	16.75	0.000	21.96
Error	20	0.029519	0.049452	0.001476			13.16
Total	26	0.225163					100
S = 0.0384178 R-Sq = 86.89% R-Sq (adj) = 82.96%							

DF: degrees of freedom; Seq SS: sequential sum of squares; Adj SS: adjusted sum of squares; Adj MS: adjusted mean squares.

It shows the contribution of each parameter on coefficient of friction. In this case all the three have significant effect on coefficient. Even though the coefficient of friction is not an inherent material property; it depends very much on the operating conditions and surface conditions, all the three parameters are significant here. The contribution of grit is highest of 37.38%, load has 27.50% and speed has 21.96% contribution.

Regression Analysis: Coefficient of Friction vs. Grit, Load and Speed

The Regression Analysis gives the correlation between the parameters, Avg. COF versus grit, load, speed. The regression equation is as shown in equation 4.3.

$$\text{Avg. COF} = 0.366 + 0.0683 \times (\text{A}) - 0.0572 \times (\text{B}) + 0.0522 \times (\text{C}) \quad (4.3)$$

4.1.3.1 ANOVA and Regression Analysis with Interaction in Between Parameters: Coefficient of Friction

The ANOVA for coefficient of friction, using Adjusted SS for tests is as shown in Table 4.7.

Table 4.7 Analysis of interactions for avg. COF

Source	DF	Seq SS	Adj SS	Adj MS	F	P	P% (Contribution)
Grit	2	0.065696	0.065696	0.032848	25.20	0.000	31.05
Load	2	0.087163	0.087163	0.043581	33.43	0.000	41.20
Grit × Load	2	0.001607	0.001607	0.000804	0.62	0.564	0.76
Grit × Load × Load	2	0.000496	0.000496	0.000248	0.19	0.830	0.23
Speed	2	0.040363	0.040363	0.020181	15.48	0.002	19.08
Grit × Speed	2	0.000230	0.000230	0.000115	0.09	0.917	0.19
Grit × Speed × Speed	2	0.000674	0.000674	0.000337	0.26	0.589	0.32
Load × Speed	2	0.001474	0.001474	0.000737	0.57	0.589	0.70
Load × Speed × Speed	2	0.003430	0.003430	0.001715	1.32	0.321	1.62
Error	8	0.010430	0.010430	0.001304			4.93
Total	26	0.211563					100
S = 0.0361068 R-Sq = 95.07% R-Sq (adj) = 83.98%							

DF: degrees of freedom; Seq SS: sequential sum of squares; Adj SS: adjusted sum of squares; Adj MS: adjusted mean squares.

The percentage contribution of each parameter including interaction is as shown in the last column of the table. The most significant parameter is grit size, followed by load, and speed respectively.

The interaction plot of means and S/N ratio is as shown in Figure 4.4. It is observed that there is no interaction between the parameters that can affect the avg. coefficient of friction. It can be seen from Table 4.7 the influence of various parameters. Here it is important to note that, effect of temperature is not considered while doing the analysis. However, the temperature has impact on the COF [42]. Mild rise in temperature often leads to a decrease in COF due to thermal softening of the surface of metals. Moderate to high temperatures increases the COF due to abrasive oxides formed due to oxidation, phase transformation or structural changes,

conversely very high temperature may decrease the COF due to formation of trioxides, protective oxides layer on the rubbing surface.

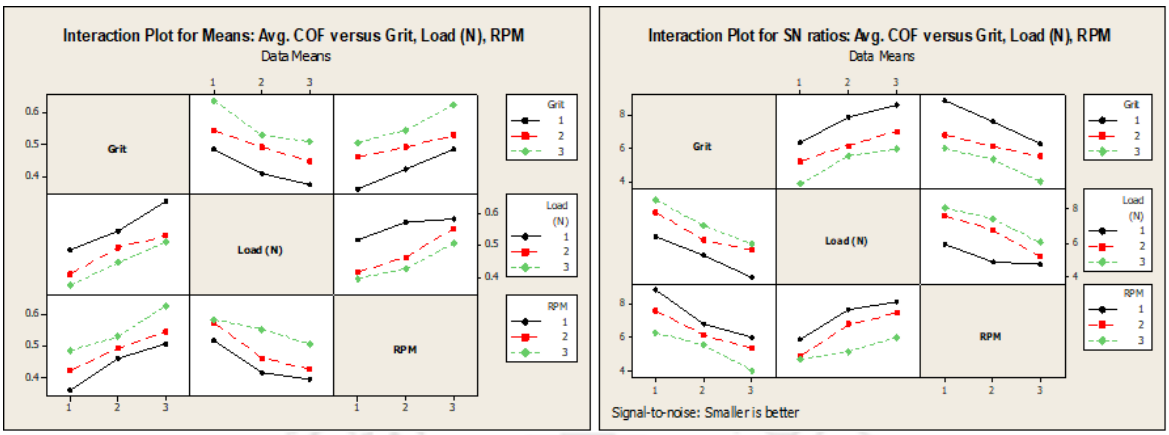

Figure 4.4 Interaction plots of (a) means and (b) S/N ratios, Avg. COF versus Grit, Load, Speed.

Regression Analysis: The equation obtained by regression for Avg. COF, showing the relation among parameters including interaction of parameters is as shown in equation 4.4.

$$\text{Avg. COF} = 0.407 + 0.0600 \times (\text{A}) - 0.0683 \times (\text{B}) + 0.00444 \times (\text{A} \times \text{B}) - 0.0011 \times (\text{A} \times \text{B} \times \text{B}) + 0.0472 \times (\text{C}) + 0.00333 \times (\text{A} \times \text{C}) + 0.00611 \times (\text{A} \times \text{C} \times \text{C}) - 0.00833 \times (\text{B} \times \text{C}) - 0.00056 \times (\text{B} \times \text{C} \times \text{C}) \quad (4.4)$$

4.1.4 Analysis of Surface Roughness (R_a) vs. Grit, Load and Speed

(a) S/N Ratio Analysis

The Response Table for roughness R_a versus Grit, Load, Speed is shown in Table 4.8.

Table 4.8 Response Table: surface roughness versus Grit, Load and Speed

Signal to Noise Ratios (Smaller is better)			
Level	Grit	Load	Speed
1	9.834	6.486	7.788
2	7.402	6.977	6.385
3	3.482	7.256	6.545
Delta	6.352	0.770	1.403
Rank	1	3	2

(a)

Response Table for Means			
Level	Grit	Load	Speed
1	0.3286	0.4918	0.4386
2	0.4303	0.4696	0.5032
3	0.6727	0.4702	0.4898
Delta	0.3441	0.0222	
Rank	1	3	2

(b)

It is seen that the grit size is the most influential parameter followed by speed and load respectively.

The Main effects plots of means and S/N ratios, Ra versus Grit, Load, Speed is as shown in Figure 4.5. As per the plot, grit size has highest S/N ratio for the lowest level followed by moderate and highest level. However, for Load even though S/N ratio has not considerable variation, the highest Load has highest S/N ratio followed by moderate and lowest load

respectively. For speed, it is highest for lowest followed by lowest and moderate respectively with slight variation.

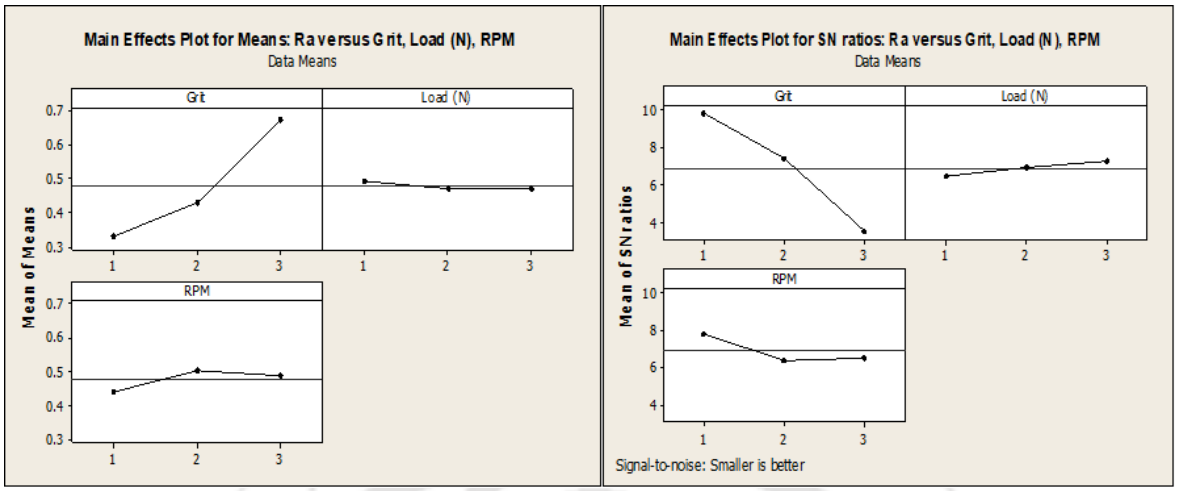

Figure 4.5 Main effects plots of means and S/N ratios: Surface roughness (R_a) versus Grit, Load, Speed

(b) ANOVA and Regression Analysis: Surface Roughness vs. Grit, Load, Speed

The ANOVA table for Surface roughness (R_a) versus Grit, Load, Speed is as shown in Table 4.9.

Table 4.9 Analysis of Variance for Surface roughness (R_a), using Adjusted SS for Tests

Source	DF	Seq SS	Adj SS	Adj MS	F	P	P % (Contribution)
Grit	2	0.562490	0.562490	0.281245	74.69	0.000	85.02
Load	2	0.002877	0.002877	0.001438	0.38	0.687	0.43
Speed	2	0.020959	0.020959	0.010479	2.78	2.78	3.17
Error	20	0.075307	0.075307	0.003765			11.38
Total	26	0.661632					100
S = 0.0613623 R-Sq = 88.62% R-Sq(adj) = 85.20%							

DF: degrees of freedom; Seq SS: sequential sum of squares; Adj SS: adjusted sum of squares; Adj MS: adjusted mean squares.

The most significant parameter is Grit followed by Load and Speed respectively. However, the contribution of Load and Speed is insignificant as per the values obtained. The contribution of Grit is 85.02%, Load has 0.43% and Speed has 3.17% contribution. Here the error has contribution of 11.38 %. However as per R-Sq. value 88.62 it is in the acceptable range.

Regression Analysis: Surface Roughness vs. Grit, Load, Speed

As per the regression Analysis of surface roughness (R_a) versus Grit, Load, Speed, the regression equation is as shown in equation 4.5.

$$Ra = 0.103 + 0.172 \times (A) - 0.0108 \times (B) + 0.0256 \times (C) \quad (4.5)$$

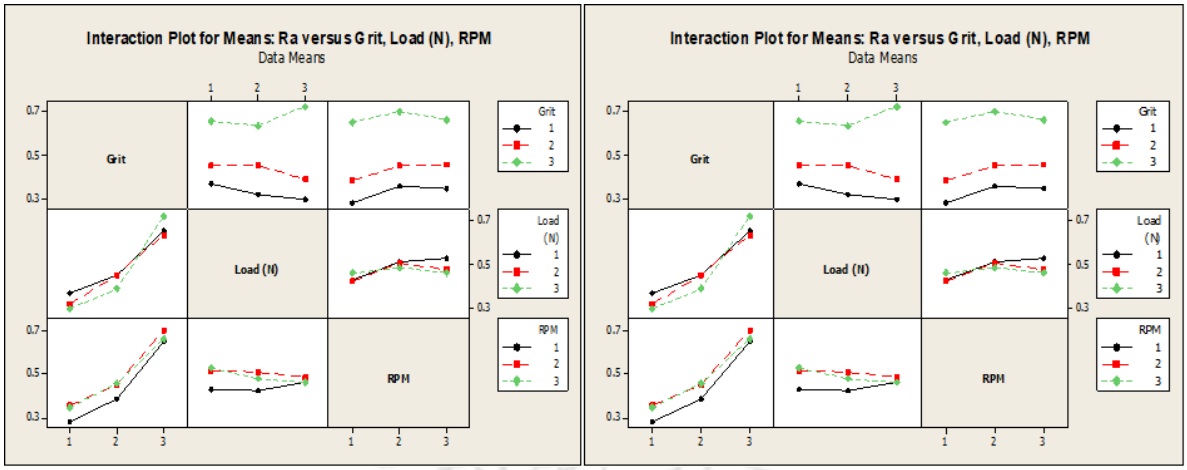

Figure 4.6 Interaction plots of means and S/N ratios: R_a versus Grit, Load, Speed

The interaction plot in between the parameters is as shown in figure 4.6. Interaction can be seen in between grit and speed.

4.1.4.1 ANOVA and Regression Analysis with Interaction in Between Parameters: Surface Roughness (R_a)

The ANOVA for Surface Roughness, using Adjusted SS for tests is as shown in Table 4.10.

Table 4.10 Analysis of Variance for R_a, using Adjusted SS for Tests

Source	DF	Seq SS	Adj SS	Adj MS	F	P	P% (Contribution)
Grit	2	0.562490	0.562490	0.281245	135.32	0.000	85.02
Load	2	0.002877	0.002877	0.001438	0.69	0.528	0.43
Grit × Load	2	0.005569	0.005569	0.002785	1.34	0.315	0.84
Grit × Load × Load	2	019846	0.019846	0.009923	4.77	0.043	3.00
Speed	2	0.020959	0.020959	0.010479	5.04	0.038	3.17
Grit × Speed	2	0.001037	0.001037	0.000518	0.25	0.785	0.16
Grit × Speed × Speed	2	0.002471	0.002471	0.001236	0.59	0.574	0.37
Load × Speed	2	0.006437	0.006437	0.003218	1.55	0.270	1.00
Load × Speed × Speed	2	0.023319	0.023319	0.011659	5.61	0.030	3.52
Error	8	0.016627	0.016627	0.002078			2.51
Total	26	0.661632					100
S = 0.0455898 R-Sq = 97.49% R-Sq (adj) = 91.83%							

DF: degrees of freedom; Seq SS: sequential sum of squares; Adj SS: adjusted sum of squares; Adj MS: adjusted mean squares.

The percentage contribution of each parameter including interaction is as shown in the last column of the table. The most significant parameter is Grit size, followed by Load x Speed x Speed, Speed and Grit x Load x Load respectively.

Regression Analysis: The equation obtained by regression for Surface Roughness R_a, showing the relation among parameters including interaction of parameters is as shown in equation 4.6.

$$Ra = 0.0296 + 0.172 \times (A) - 0.0108 \times (B) + 0.0022 \times (A \times B) - 0.0269 \times (A) \times (B) \times (B) + 0.0256 \times (B) - 0.0024 \times (A \times B) + 0.0068 \times (A \times B \times B) + 0.0168(A \times B) + 0.0356 \times (B \times C \times C) \quad (4.6)$$

4.2 Contour Plots and Surface Plots of Parameters

Contour plot and Surface plots shown in figures 4.7 to 4.9 depicts the change in output parameters as per the change in input parameters on the entire region/ surface.

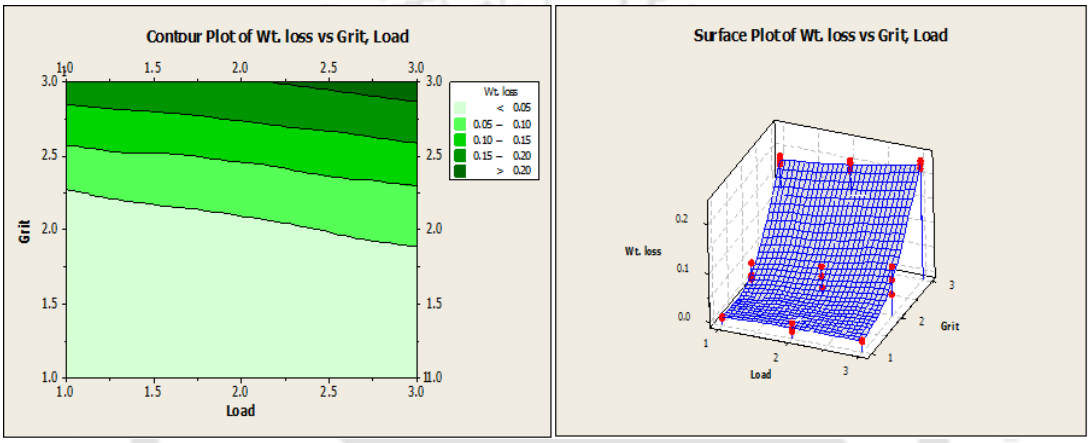

(a) (b)

Figure 4.7 (a) Contour plot and (b) Surface plot of wt. loss

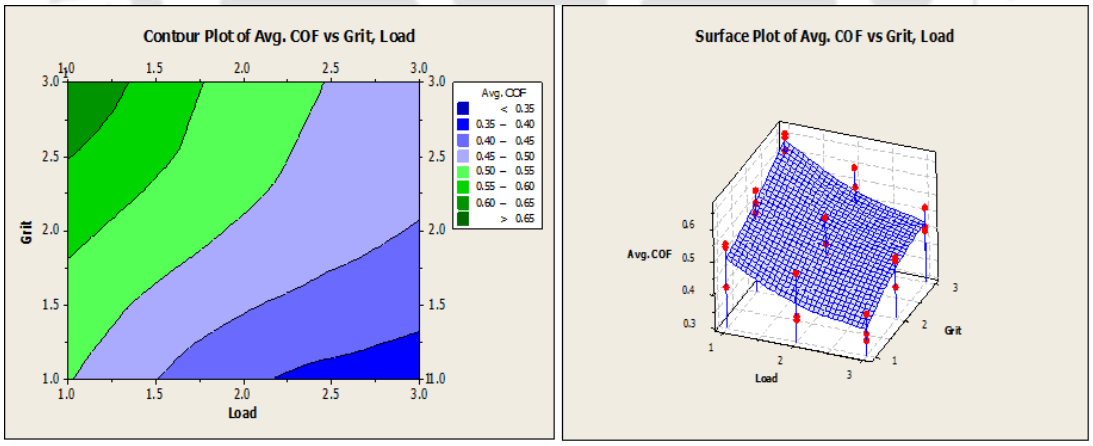

(a) (b)

Figure 4.8 (a) contour plot and (b) surface plot of Coefficient of friction

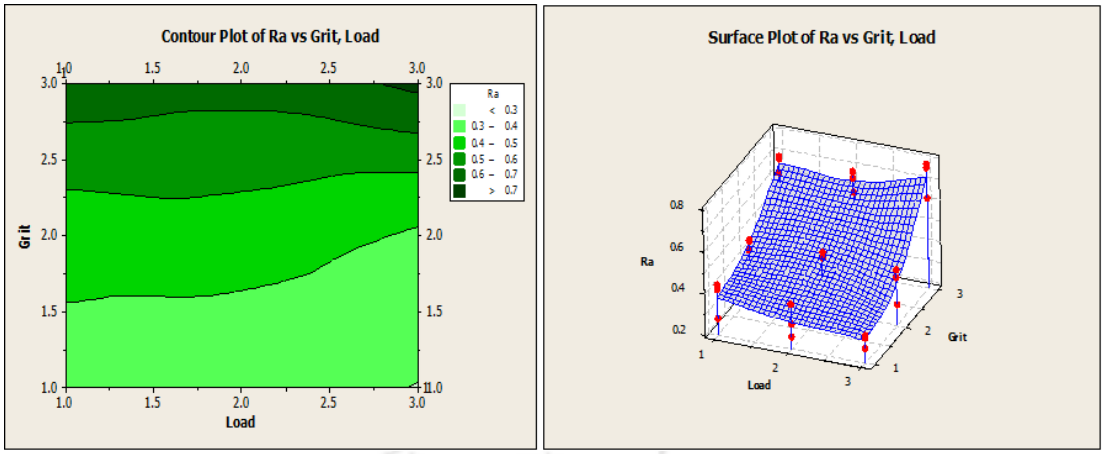

(a) (b)

Figure 4.9 (a) contour plot and (b) surface plot of surface roughness

The change in wt. loss, as per change in the level of input parameters such as grit and load is shown in Fig. 4.7 (a) and (b). Wt. loss increases as grit size and load increases. The change in Coefficient of friction and Surface roughness changes, as per change in the level of input parameters is shown in Fig. 4.8 and 4.9 respectively.

4.3 Surface Morphology of the Worn Surfaces

The worn-out surfaces are observed under SEM, to study surface morphology. The surface morphology of the worn surfaces is shown in following figures from Figure 4.10 to 4.12. The images clearly show the scratches formed due to the material removed by microchips, cutting and ploughing as well as groves formed due to plastically impressed grits of abrasive. It is observed that the different modes of abrasive wear such as cutting, ploughing are clear in all the specimens at different operating parameters. For the specimen abraded by 320 G along with cutting and ploughing, plastically impressed grooves are significantly observed. For 600 G the scratches are shallow as compared to the scratches on specimen with other two grit sizes. The worn specimens were characterized by SEM to evaluate the following wear mechanisms.

Ploughing Mode: The flow of material to both sides of the groove, which does not generate volume removal from the groove. The ploughing mode of wear is evident in figures 4.15 (b).
Cutting Mode: The groove in the cutting mode shows that the larger part of the groove volume is lost as wear without remaining at the sides of the groove. The cutting mode of wear can be observed in figures 4.11 and 4.12. Figure 4.11 shows abrasion due to highest grit size, lowest load and moderate speed. The deep scratches with discontinuity are observed. From figure, 4.11 it can be seen that the scratches formed are not continuous.

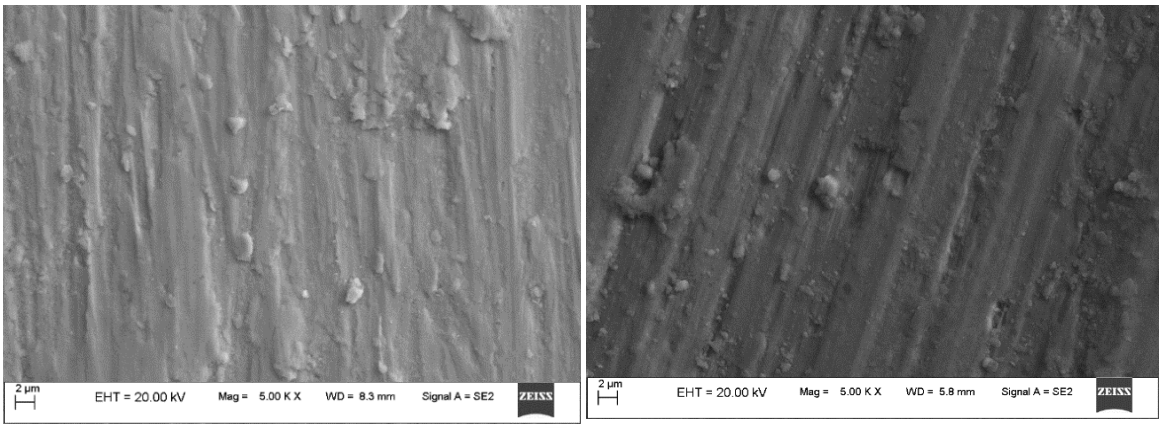

(a) (b)

Figure 4.10 Worn out Surface of parameters (a) 320 G 15 N 200 RPM (b) 320 G 20 N 250 RPM

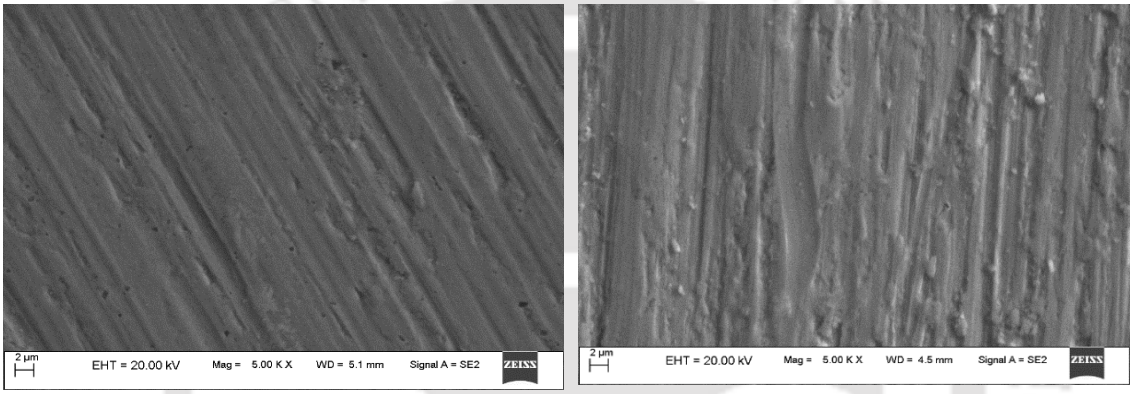

(a) (b)

Figure 4.11 Worn out surface of pin by various parameters (a) 400 G 10 N 250 RPM (b) 400 G 15 N 150 RPM

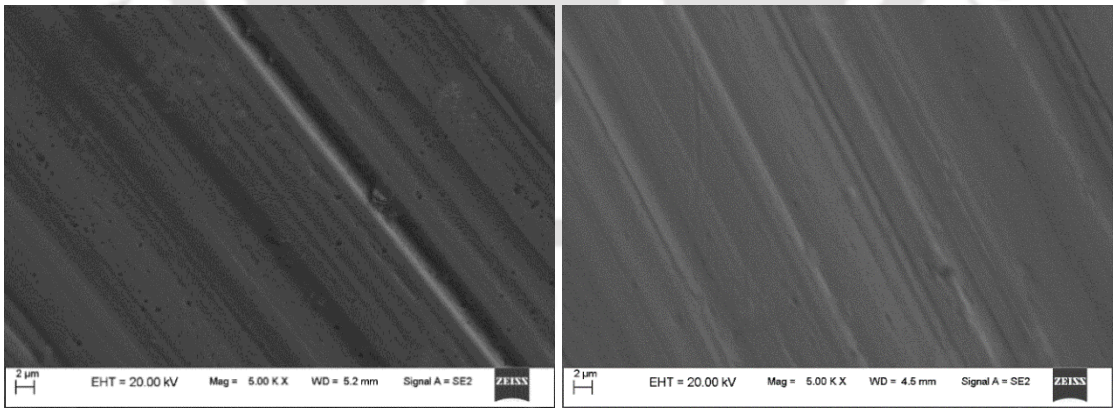

(a) (b)

Figure 4.12 Worn out surface of pin by various parameters (a) 600 G 15 N 250 RPM (b) 600 G 200 RPM 10 N

The discontinuity formed due to material removal by microchipping. The discontinuity due to microchipping is prominently seen for the specimen abraded by higher Grit size. For lower grit size the scratches are shallow.

4.4 EDS Analysis

Scanning electron microscopic (SEM, 20 kV with SE2 detector) techniques were used for surface characterization. A SEM image of the sample after wear testing is shown in Figure 4.13. The distribution of elements are found to be of similar range of as received sample.

(a)

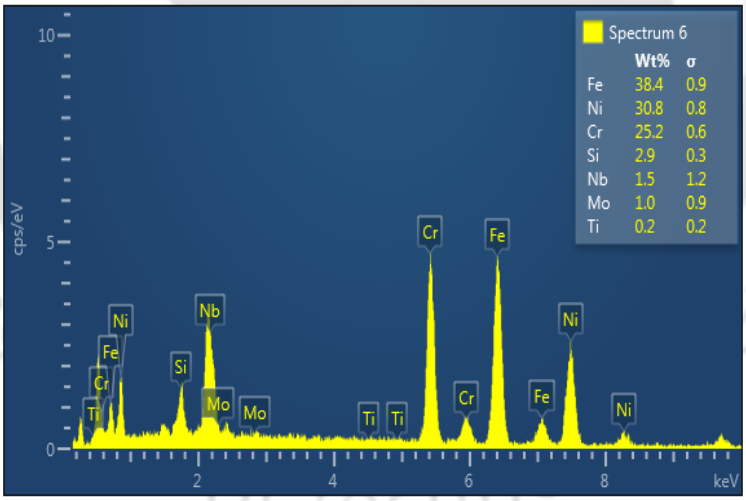

(b)

Figure 4.13 A typical EDS spectrum (b) of the worn HP40Nb pin surface at various locations (a) of the pin sample worn by parameters 320 G 250 RPM 20 N

4.5 Surface Topography of the Worn Surfaces

The surface topography of the pin, as well as the wear track of the disc, was investigated using the surface profilometer (Model: Form Talysurf; Make: Taylor Hobson Co.) over an area of 865 μm × 865 μm. Figure 4.14, 4.15 and 4.16 shows the surface profile of the pin after wear

testing under various conditions of grit size, load and Speed. The maximum roughness is represented by the Z value in each figure.

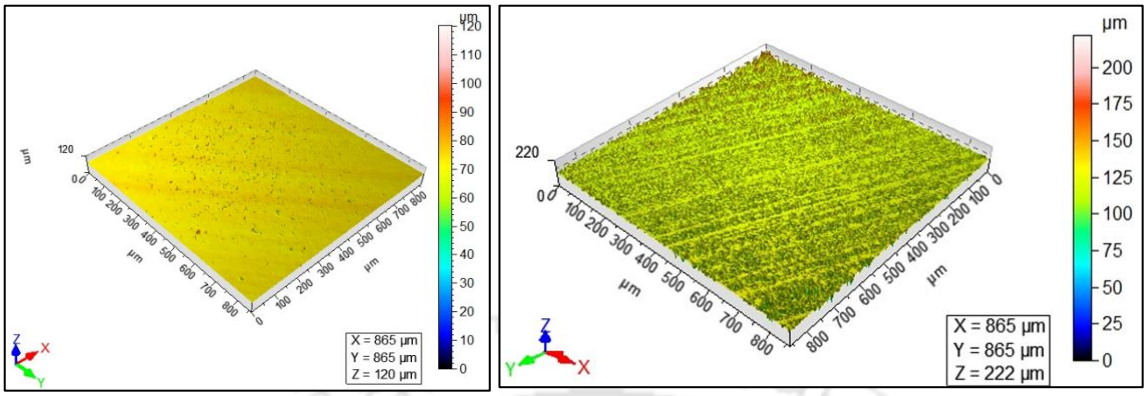

(a) (b)

Figure 4.14 3D profile pin surface worn by parameters (a) 320 G 10 N 150 RPM (b) 320 G 20 N 200 RPM

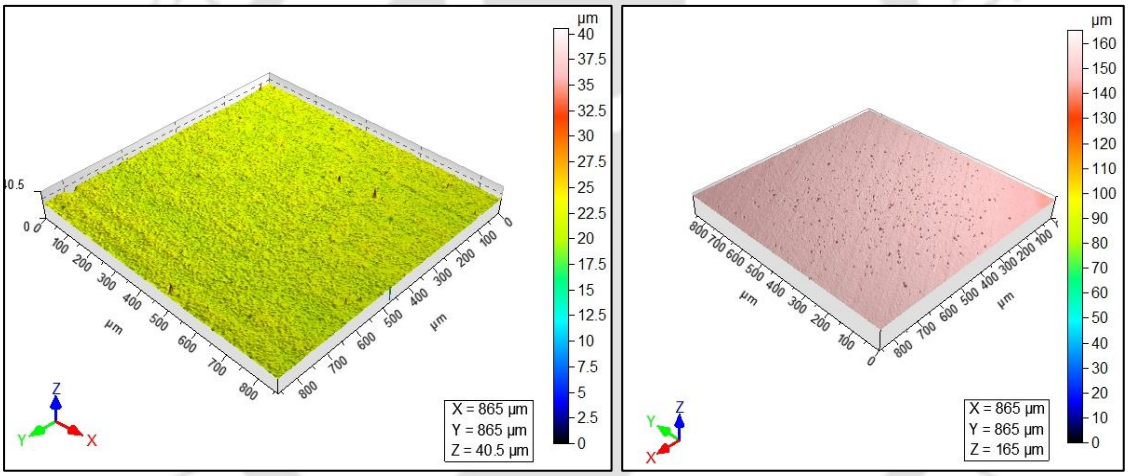

(a) (b)

Figure 4.15 3D profile pin surface worn by parameters (a) 400 G 10 N 200 RPM (b) 400 G 15 N 250 RPM

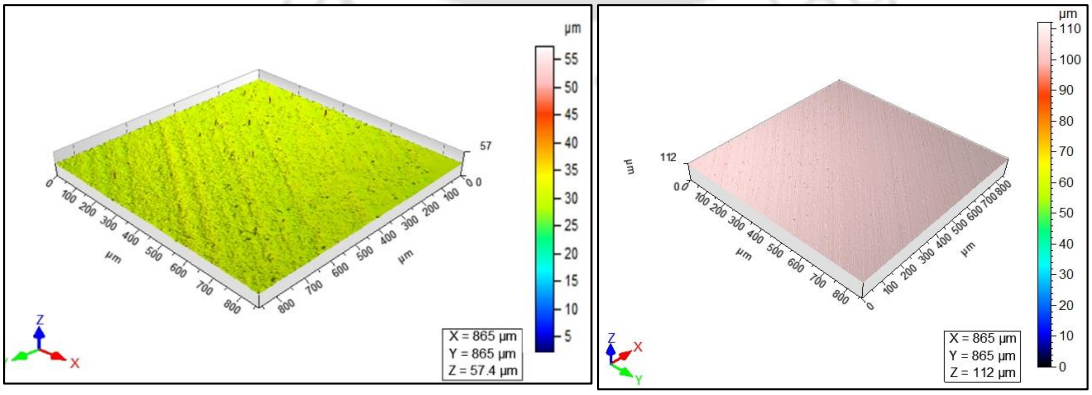

(a) (b)

Figure 4.16 3D profile pin surface worn by (a) 600 G 15 N 150 RPM (b) 600 G 20 N 200 RPM

It is observed that; Z value is more for the high load conditions as compared to the low load conditions. Also, for the specimen worn by higher grit size the Z values are more as compared to the specimen surface worn by smaller grit size of 400 G and 600 G.

4.5 summary of chapter 4

The abrasive wear analysis was done using Taguchi analysis. The grit size has the strongest influence on wear as well as on COF. It was followed by load but has much less effect as compared to grit size and followed by disc rotational speed. The interaction between the parameters has been also found influential on wear. Though the most significant parameter is Grit size, the interaction is found influential as Load, Grit × Load × Load, Grit × Speed × Speed and Speed respectively. The surface topography revealed various features of abrasive wear mechanism such as ploughing, cutting, wedge forming, microchipping etc.

Chapter 5
Adhesive Wear of HP40Nb SS

This chapter presents the results obtained from the investigation of the effect of load and speed on the COF and wear rate and the effect of sliding distance on adhesive wear rate. The experiments were performed by using full factorial technique. The results of the characterization of the worn surfaces by SEM/EDS, digital profilometer, surface roughness, microstructure evaluation and wear debris analysis is also being presented and discussed in the subsequent section.

5.1 Adhesive Wear Test Results and Analysis

5.1.1 Effect of Load on Coefficient of Friction (COF)

Figures 5.1 to 5.4 depicts the changes in the coefficient of friction (COF) under varying loads at rotational speeds of 150 RPM, 200 RPM, 250 RPM, and 300 RPM, respectively. Figure 5.1(a) presents how the COF evolves over time for different load conditions at 150 RPM. As shown in Figure 5.1(b), the average COF values at this speed remain relatively consistent, ranging from approximately 0.74 to 0.76 as the applied load increases from 5 N to 20 N. This suggests that at 150 RPM, the effect of load on COF is minimal. In contrast, at 200 RPM, the COF starts at 0.77 under a 5 N load and decreases to 0.68 at 10 N, indicating stronger adhesion between the pin and disc at lower loads [11]. Similarly, Figures 5.2 (a), 5.3 (a), and 5.4 (a) reveal that at higher speeds of 250 RPM and 300 RPM, the COF is greater under a 5 N load compared to a 10 N load.

For the 20 N load at 200 RPM, 250 RPM, and 300 RPM, the coefficient of friction (COF) increases during the initial 500 seconds, as shown in Figures 3 (a) to 5 (a). After reaching a certain level, it fluctuates around a mean value for the remainder of the test period. Similar behavior has been observed in previous studies involving AISI 1018 steel–AISI D2 tool steel contact pairs [61, 64].

An increase in sliding speed tends to raise the coefficient of friction (COF) at lower loads, primarily due to adhesive interactions between the sliding surfaces [11]. In contrast, at higher loads, the COF tends to decrease as the hard surfaces experience plastic deformation, resulting in smoother contact and a reduced ploughing effect [11, 53, 56]. Numerous studies have highlighted the relationship between COF and variables such as normal load, sliding speed, and apparent contact area under both dry and lubricated conditions [13].

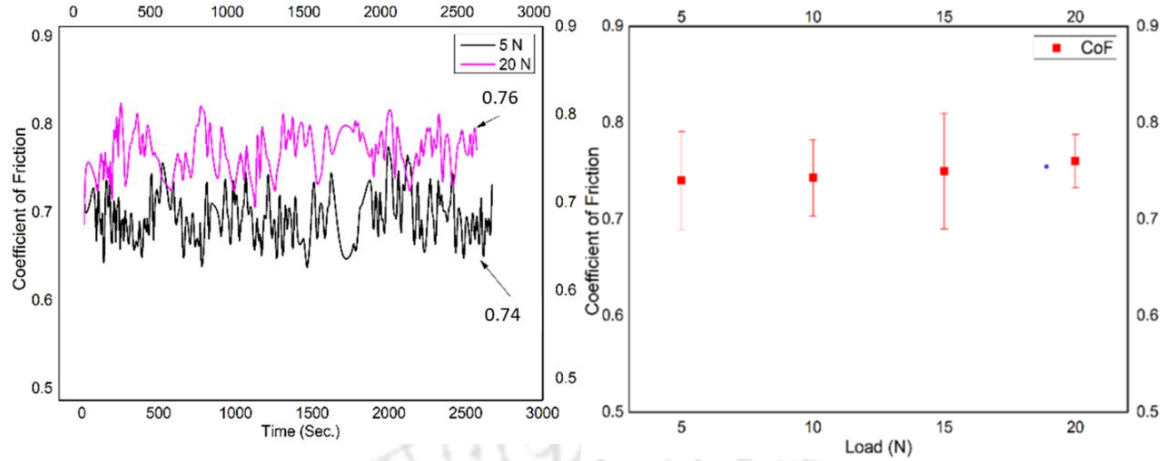

(a) (b)

Figure 5.1 Plots of COF vs (a) time and (b) load 150 RPM

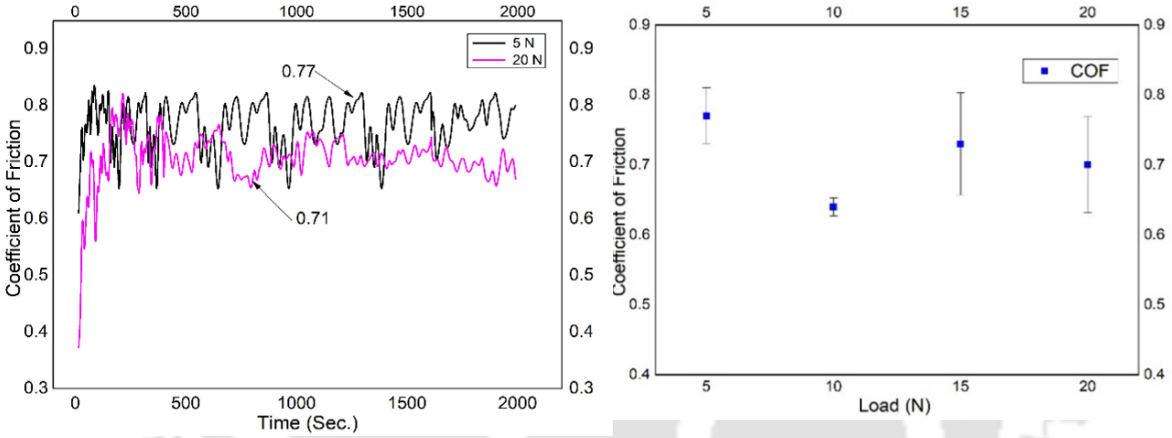

(a) (b)

Figure 5.2 Plots of COF vs (a) time and (b) load 200 RPM

For metallic contact pairs, the coefficient of friction (COF) generally increases at lower loads as the load rises, primarily due to the breakdown of the oxide layer and/or the onset of plastic deformation. This elevated COF typically remains stable within a certain load range but begins to decline at higher loads as interfacial changes occur due to wear mechanisms [94]. Frictional heating also plays a role: at lower loads, limited heat dissipation leads to localized temperature increases and higher friction. However, at higher loads, the generated heat may reach a threshold that softens the material, reducing stiffness and thereby facilitating smoother sliding [11].

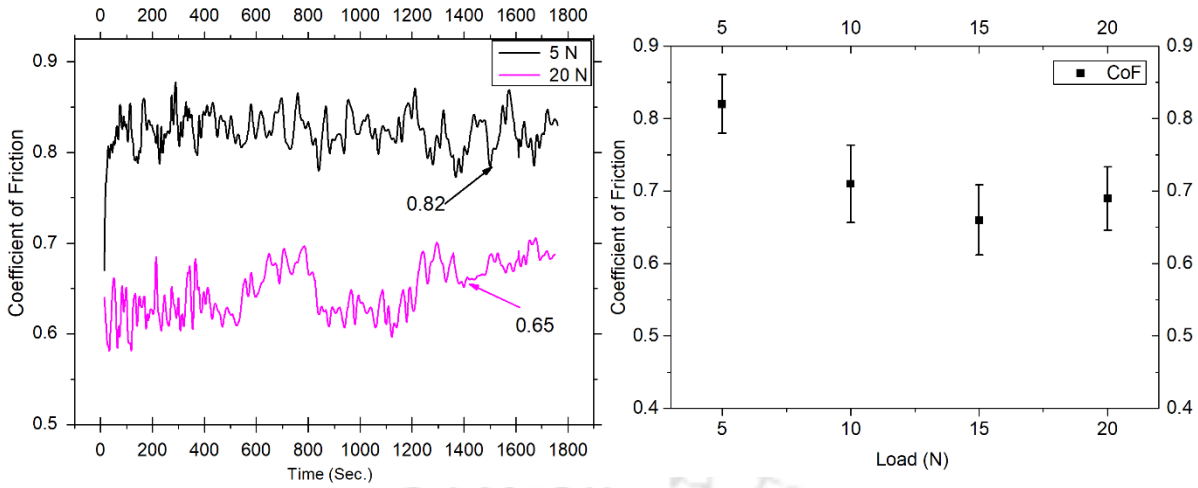

Figure 5.3 Plots of COF vs (a) time and (b) load 250 RPM

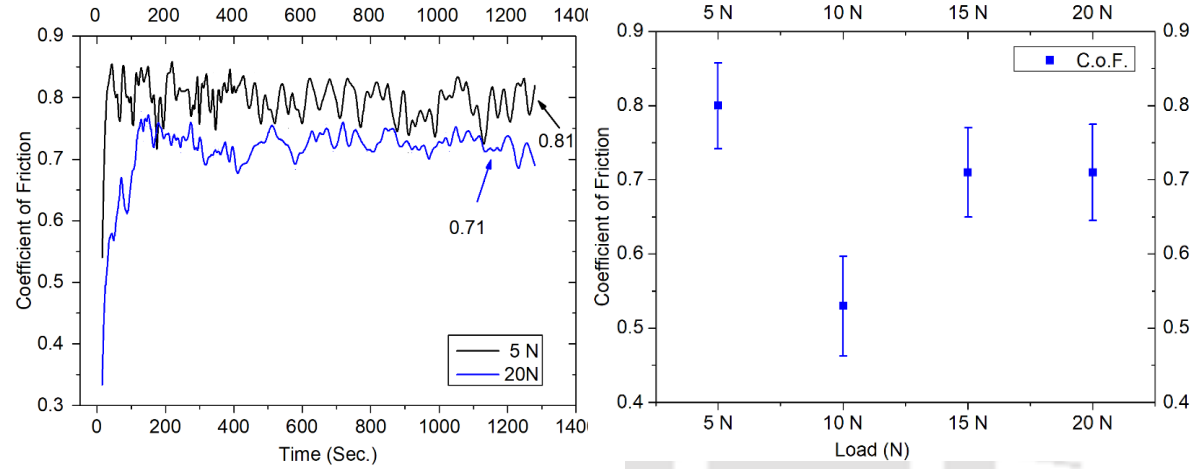

Figure 5.4 Plots of COF vs (a) time and (b) load 300 RPM

At higher loads, surface asperities are sheared off more rapidly with increasing velocity, resulting in a more significant reduction in friction. In contrast, at a lower load of 5 N, the contact between surfaces is likely dominated by static friction. As velocity increases, a transition from static to kinetic friction typically occurs. However, in some materials, this transition may not be smooth, leading to irregular frictional behavior at low loads. Additionally, at lower loads, microscopic adhesion plays a more prominent role due to the smaller real area of contact, with surface asperities largely governing the interaction. This can increase adhesion forces between asperities, resulting in higher friction at low velocities. As velocity rises, these asperities may deform or fracture more easily, which can sometimes cause a temporary increase in friction until a steady-state friction level is achieved [94].

5.1.2 Effect of Speed on Coefficient of Friction

Figure 5.5 shows the variation of the coefficient of friction (COF) with applied load at different rotational speeds (RPM). At 150 RPM, the COF remains nearly constant across all loads. Across all RPMs, the COF is highest at a 5 N load compared to higher loads. The lowest COF is observed at 10 N load with a rotational speed of 300 RPM.

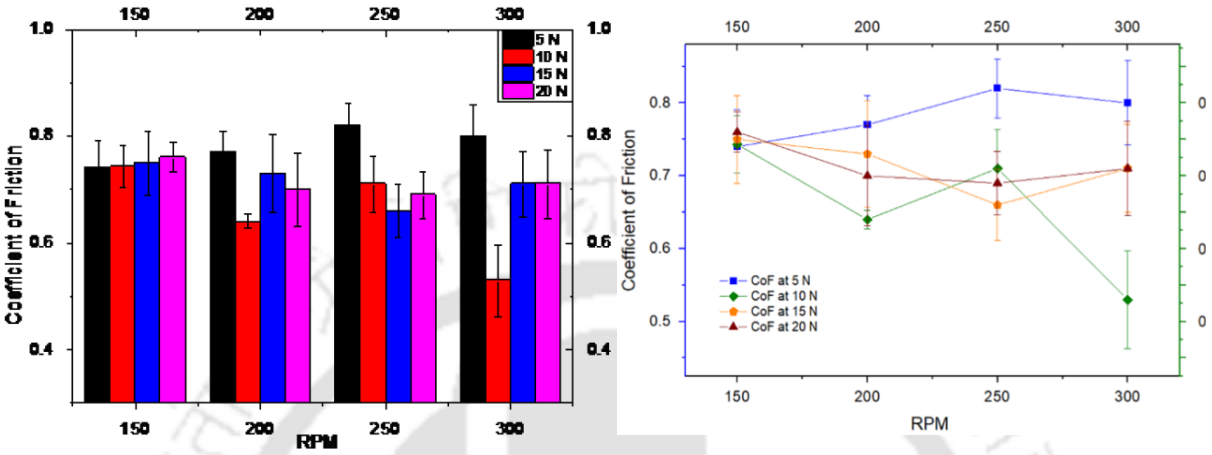

(a) (b)

Figure 5.5 Plot of COF vs RPM at various loads

At a 5 N load, the coefficient of friction (COF) increases steadily up to 250 RPM, after which it begins to decline gradually. As shown in Fig. 5.5 (b), at higher RPMs and across all loads, significant variations in COF are observed. Continued sliding leads to increased surface roughness, resulting in fluctuations in the frictional force and, consequently, changes in COF [95]. Elevated sliding velocities or higher contact pressures can cause frictional heating at the interface. This thermal effect may lead to the formation of a surface film with low shear strength, and in some cases, localized melting may occur. On the other hand, softening at the interface can lead to deeper ploughing in the softer material. Due to the complex interplay of these mechanisms, no consistent trend in COF can be established [95].

At a 10 N load, the balance between contact area and pressure appears optimal for minimizing friction, as it reduces interaction with surface asperities. In contrast, at a 5 N load, the contact area may be too small, leading to elevated localized pressures at asperity contact points. At higher loads of 15 and 20 N, the increased pressure enlarges the real contact area, resulting in greater friction. High sliding velocities and/or elevated contact pressures can generate significant frictional heating at the interface. This heating may lead to the development of a surface film with low shear strength and, in some cases, localized melting. Conversely, softening at the interface may increase ploughing in the softer material. The complex interplay

of these factors makes it difficult to predict the exact influence of sliding velocity on friction [94].

5.1.3 Effect of Load on Wear Rate

Figure 5.6 depicts the plot of wear rate versus load at various RPMs for a sliding distance of 1000 meters. The wear rate shows an increasing trend with rising load. The highest wear rate is recorded at 250 RPM under a 20 N load, while the lowest wear rate occurs at 300 RPM under a 5 N load. At the 5 N load level, higher speeds (250 RPM and 300 RPM) result in lower wear rates compared to lower speeds. As the load increases, the contact pressure between the mating surfaces also rises, contributing to the increased wear.

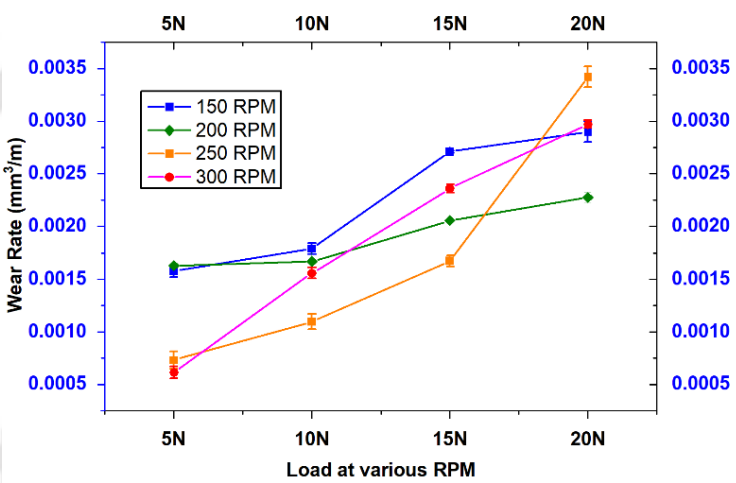

Figure 5.6 Plot of Wear Rate vs load for various speed

Higher loads promote adhesive wear by inducing localized plastic deformation and encouraging the formation of micro-welds at surface asperities. As the load increases, the materials in contact undergo more substantial plastic deformation, which leads to the generation of wear debris and facilitates material transfer between the surfaces. Deformation mechanisms such as micro-cutting, ploughing, and grooving become more prominent under elevated loads. When the normal load on the contact interface rises, the metal within the asperities deforms plastically, enlarging the actual contact area. Cold welding may also occur at these contact points [96]. The increased load thus enhances the real contact area, strengthening junctions at asperities and resulting in higher material transfer and wear rates. According to the Archard wear equation, wear increases with higher loads and extended sliding distances but decreases with harder materials [11, 97].

5.1.4 Effect of Rotational Speed on Wear Rate

Figure 5.7 shows the variation of wear rate vs speed. It is seen that the wear rate increases as the load increases from 10 to 15 N for all speeds.

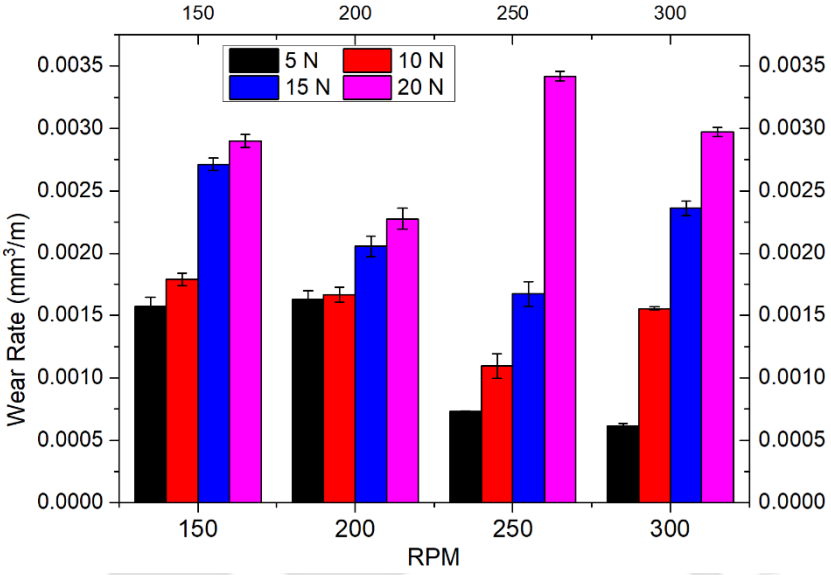

Figure 5.7 Effect of Rotational Speed on Wear

Except at the 20 N load, the wear rate decreases as the speed increases up to 250 RPM. Beyond this speed, the wear rate begins to rise. It has been noted that sliding velocity has a significant impact on the surface temperature [98]. At low loads, friction at the interface remains low, causing little to no change in interface temperature even with higher sliding speeds. However, as the load increases, wear also increases with rising sliding speed [99]. Additionally, higher sliding speeds cause ploughing to become wider and deeper. At a 5 N load, the interface temperature remains stable even at elevated sliding speeds.

As speed increases, the frictional heat generated at the interface typically rises. However, at higher sliding speeds, the reduced contact time between the surfaces leads to less material being removed [11].

5.1.5 Effect of Sliding Distance on Wear

Figures 5.8 (a) to 5.8 (d) illustrate the effect of sliding distance on the relative wear rate (as explained in section 3.6.2) at speeds ranging from 150 RPM to 300 RPM. A gradual increase in the relative wear rate is seen as the speed rises from 150 RPM to 250 RPM for sliding

distances between 0-250 m, 250-500 m, and 500-750 m. Beyond a sliding distance of 750 m, the wear rate does not follow any specific trend.

At a speed of 300 RPM, no clear trend is observed even after 500 m of sliding distance. For 150 RPM and 200 RPM, the relative wear rate decreases after 1000 m of sliding distance for an additional 250 m, except at the 10 N load. In contrast, at 250 RPM, the wear rate increases for the 10 N and 15 N loads after 1000 m for a further 250 m. Meanwhile, at 300 RPM with a 10 N load, the wear rate decreases after 1000 m for an additional 250 m. According to Archard's wear equation, wear increases with higher loads and longer sliding distances but decreases with harder materials. The wear coefficient (k) represents the complex interaction between material properties and contact conditions [97].

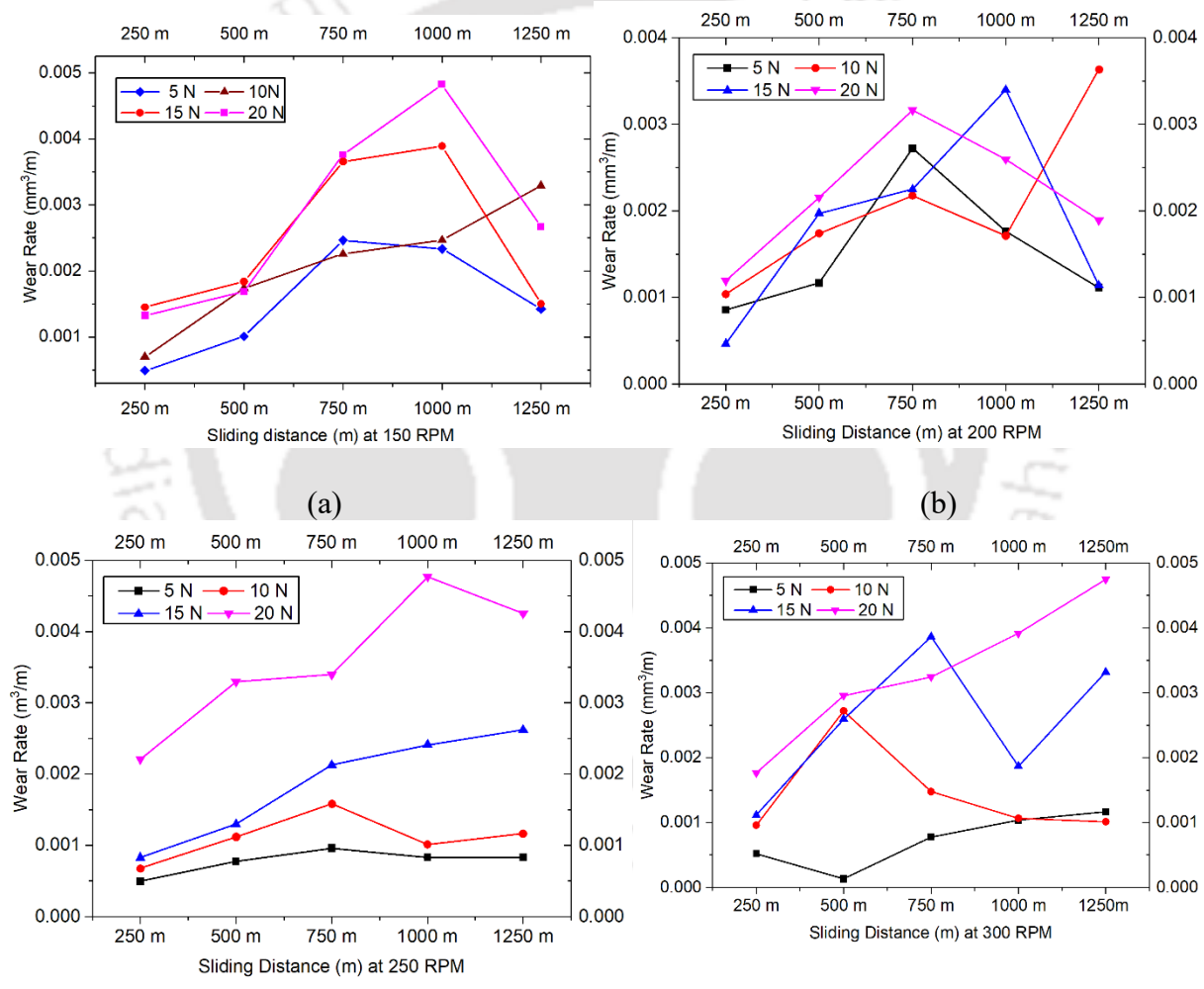

Figure 5.8 Relative wear rate vs sliding distance at (a) 150 RPM, (b) 200 RPM , (c) 250 RPM and (d) 300 RPM for different loads

5.2 Characterization of the Worn Surfaces of the Pin and Disc

Figures 5.9 (a), 5.9 (b), 5.9 (c) and 5.9 (d) present the SEM micrographs of the pin samples after the wear tests at various parameters. Features of adhesive wear, such as plastic

deformation, metal transfer, adhesion, delamination etc. are as shown by arrows “a-d” in Figures 5.9 (a), 5.9 (b), 5.9 (c) and 5.9 (d). Material accumulation and plastic deformation are seen at the contact surface edges as shown by the label “a”.

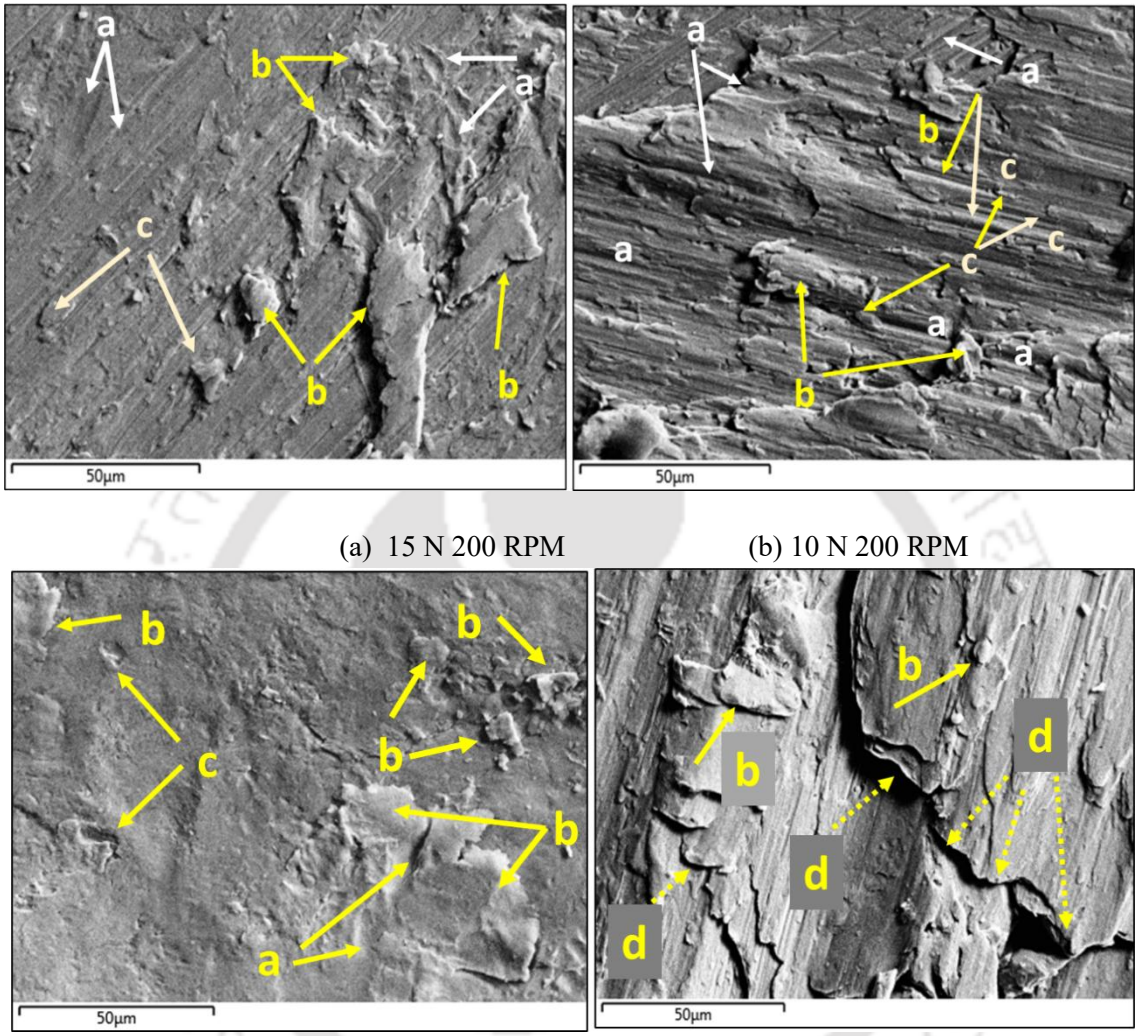

(a) 15 N 200 RPM (b) 10 N 200 RPM

(c) 5 N 250 RPM (d) 20 N 150 RPM

Figure 5.9 Worn-out pin surfaces by different parameters

The grooves resulting due to the pressure are shown labelled “a” in Figures 5.9 (a), 5.9 (b) and 5.9 (d). It happens due to the increase in contact pressure at a higher load. The material is displaced creating groves labeled “c” in Figures 5.9 (a) to (c). Similarly, Metal transfer as shown by arrows “b” in Figures 5.10 (a), to 5.10 (c).

Under a 10 N load, the surface shows clearly visible plastically deformed grooves, whereas a 15 N load causes more extensive material displacement. At the highest load of 20 N, layered features [94, 100], highlighted as “d” in Figure 5.9 (d), become more prominent.

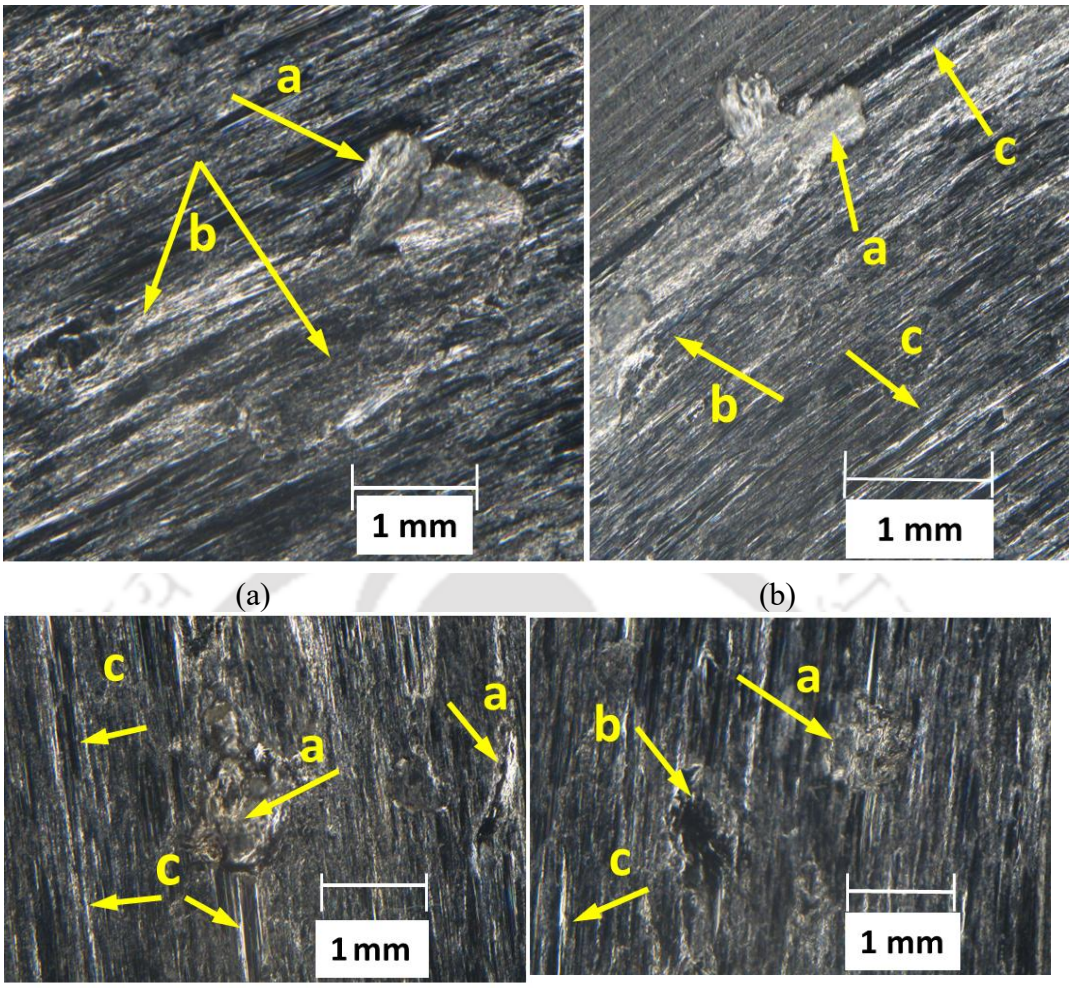

Figure 5.10 Optical micrographs of worn disc surfaces at 10 N for speeds (a) 150 RPM, (b) 200 RPM, (c) 250 RPM and (d) 300 RPM.

This is likely due to an increase in temperature, which alters the wear mechanism under the high load. The load and relative rubbing between the disc and pin generate frictional heat, causing a softening effect that can increase plastic deformation and material transfer between the contacting surfaces. This leads to adhesion, resulting in adhesive wear. Figures 5.10 and 5.11 display microscopic images of the worn disc tracks. Delamination appears as shiny patches on the disc tracks, indicated by arrows “b” in Figures 5.10 (a), 5.10 (b), and 5.10 (d). Additionally, metal transfer is highlighted by arrows “a” in Figures 5.10 (a) through (d). Plastic deformation is marked by arrows “c” in Figures 5.10 (b), 5.10 (c), and 5.10 (d). These grooves result from plastic deformation of the material, accompanied by piling up or displacement of material at the groove edges, as shown in Figures 5.10 (b), 5.10 (c), and 5.10 (d). The worn disc surfaces exhibit similar modes of adhesive wear.

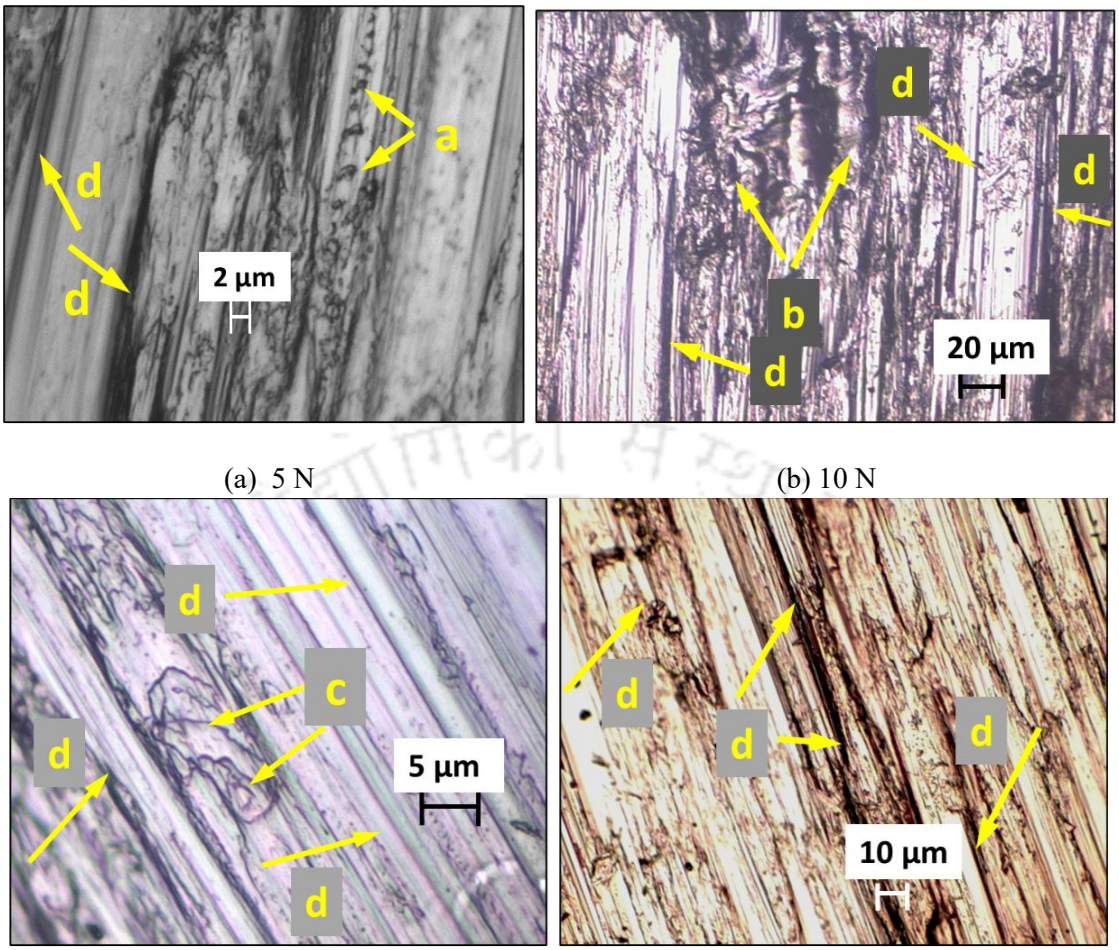

(a) 5 N (b) 10 N

(c) 15 N (d) 20 N

Figure 5.11 Worn-out disc surfaces at 150 RPM for different loads

Ploughing combined with micro-cutting is indicated by arrows labeled “a” in Figure 5.10 (a). Delamination is evident at points marked “b” in Figure 5.11 (b) and by the “c” arrows in Figure 5.11 (c). Material displacement due to plastic deformation, along with plastically induced grooves, appears more prominently, as shown by the “d” arrows in Figures 5.11(a) through (d).

5.3 EDS Analysis

Surface characterization of the pin was carried out using Scanning Electron Microscopy (SEM) at 20 kV with an SE2 detector. Figure 5.12 (a) shows a SEM image of the pin surface after wear testing. A typical Energy Dispersive Spectroscopy (EDS) spectrum, taken from the area labeled ‘Spectrum 2’ in Figure 5.12 (a), is presented in Figure 5.12 (b). Composition analysis before the wear test, as shown in Table 1, reveals that manganese (Mn) is absent in the pin but

present at 2 wt.% in the disc. Additionally, micro-cracks are observed at the same location, corresponding to the area where material transfer from the disc to the pin has been reported.

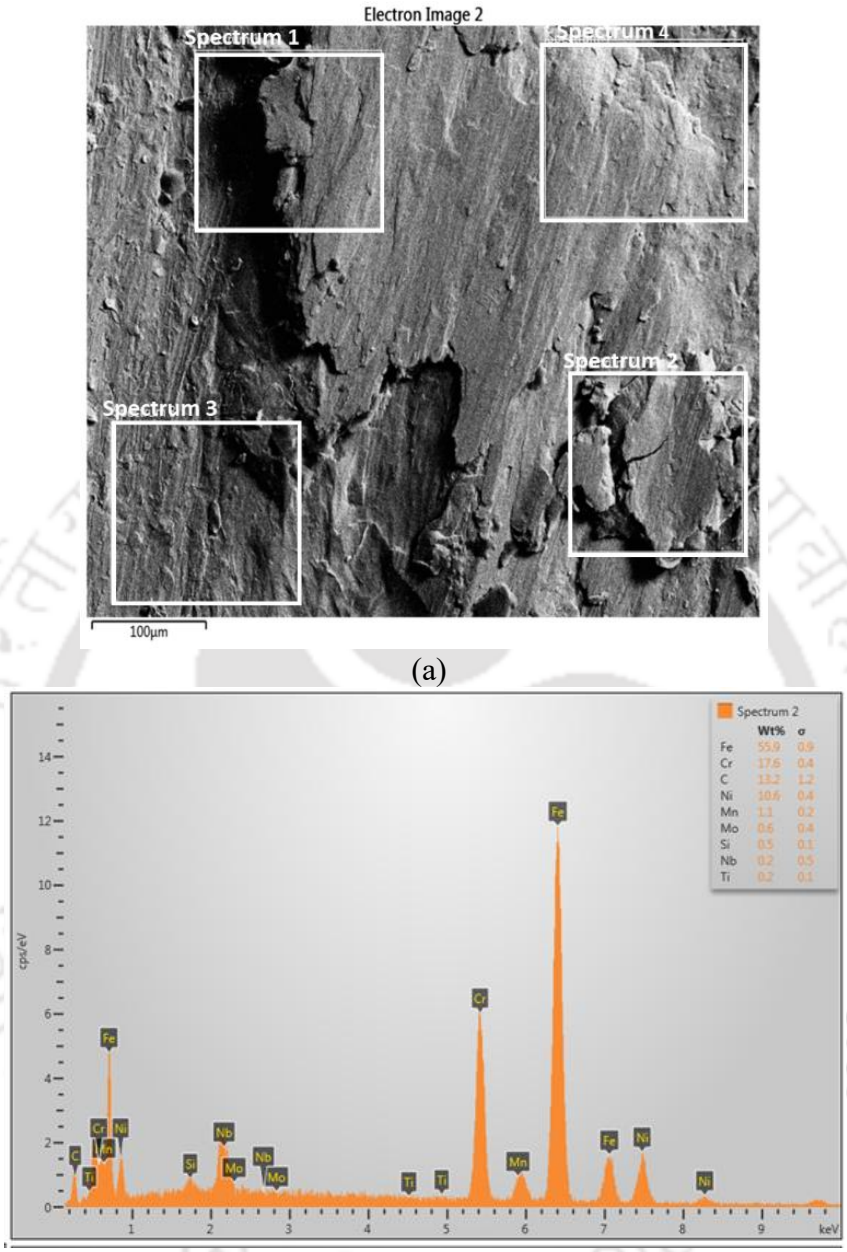

Figure 5.12 EDS spectrum (b) of the worn surface at various locations (a) of the pin sample worn by parameters 20 N /150 RPM

The EDS analysis of the wear-tested HP40Nb pin, conducted at various locations, shows manganese (Mn) content ranging from 0.4 to 1.1 wt.%, with an average of 0.7 wt.%. Similar findings have been reported in sliding wear tests of high-speed steel and white cast iron against an AISI 52100 counter-surface [101]. The present study confirms that material transfer from the disc to the HP40Nb pin occurs during the wear test. This is primarily because the pin has a

higher hardness than the SS 316 disc, causing the disc to wear due to adhesive mechanisms [71, 101].

5.4 Surface Topography of the Wear-Tested Samples

The surface topography of both the pin and the wear track on the disc was examined using a surface profilometer (Model: Form Talysurf; Manufacturer: Taylor Hobson Co.) over a measured area of 852 µm × 852 µm.

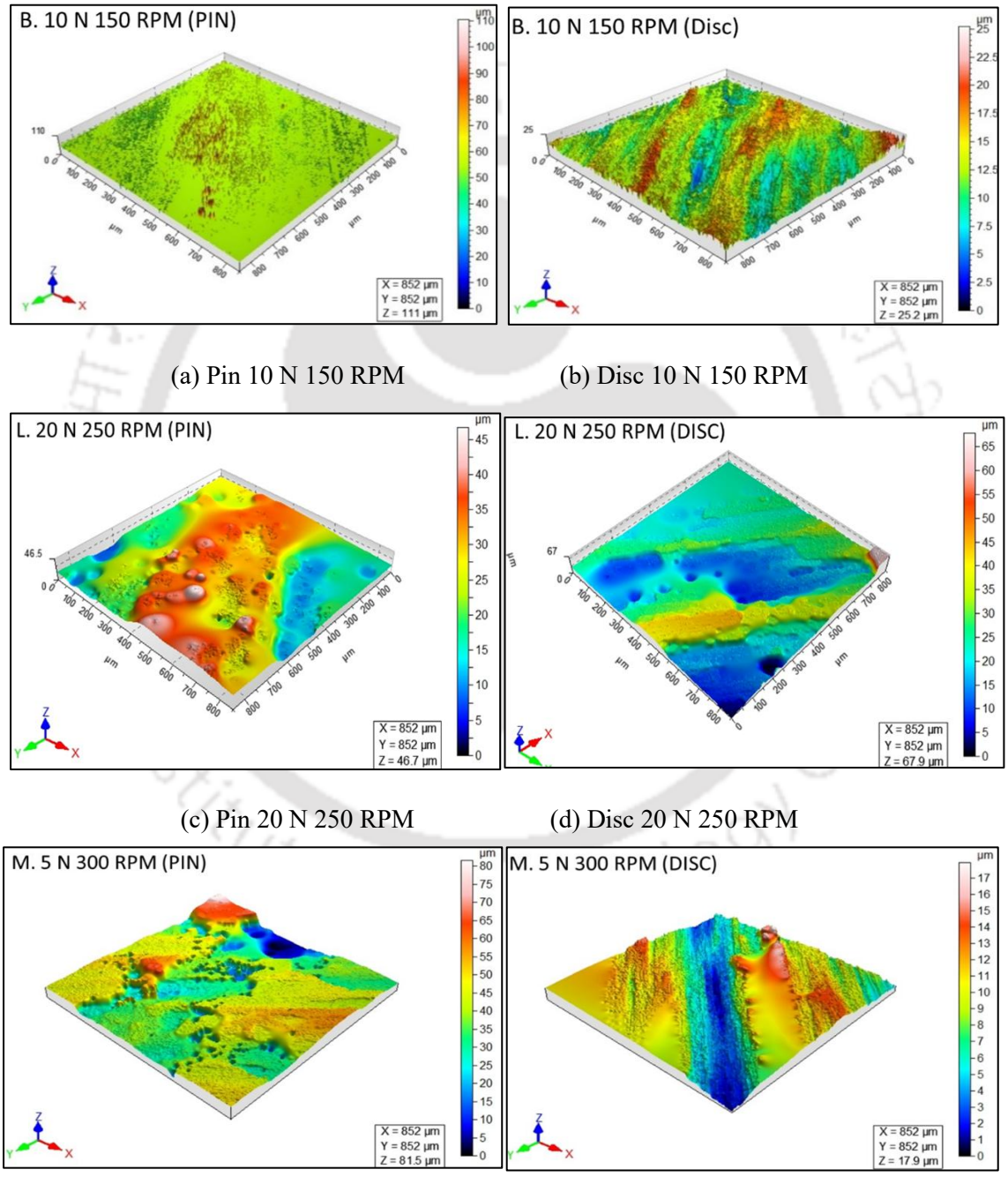

(a) Pin 10 N 150 RPM (b) Disc 10 N 150 RPM

(c) Pin 20 N 250 RPM (d) Disc 20 N 250 RPM

(e) Pin 5 N 300 RPM (f) Disc 5 N 300 RPM

Figure 5.13 3D profile of the worn surfaces

Figure 5.13 displays the surface profiles of the pin and disc following wear testing conducted under different load and rpm conditions. The maximum roughness in each image is indicated by the Z value. For each pin-disc pair, the Z value for the pin is generally higher than that for the disc, except in the test conducted at 20 N/250 RPM. The maximum Z value recorded for the disc is 67.9 µm, while the corresponding Z value for the pin is 46.9 µm, and this test also exhibits the highest wear rate. The greatest Z values for the pin are observed during wear testing at 10 N/150 RPM, with values of 111 µm and 95 µm. The elevated Z values for the pin are attributed to material transfer from the disc and its subsequent adhesion onto the pin surface. The higher Z value of the pin compared to the disc, along with the detection of manganese on the pin surface, supports the occurrence of material transfer from the softer disc to the harder pin during the wear test due to adhesion [71]. Surface profile analysis showed that the lowest Z value of 17.9 µm was recorded for the disc tested at 5 N/300 RPM, while the corresponding Z value for the pin was 81.5 µm. Notably, the wear rate was also minimal under these test conditions.

5.5 Surface Roughness Parameters

Various roughness parameters are used to characterize the surface profile. For example, Peak-to-Valley Height (R_z) indicates the overall height variation on the surface; Root Mean Square (*Rq* or *RMS*) represents the overall height variation in terms of the standard deviation; Total Roughness (R_t) measures the vertical distance between the highest peak and the deepest valley within a sampling length; and Roughness Average (R_a) is the arithmetic average of the absolute deviations of the surface profile heights from the mean line over the evaluation length.

Table 5.1 presents various roughness parameters, including peak-to-valley height (R_z), root mean square (*RMS* or R_q), total roughness or peak-to-valley height (R_t), and roughness average (R_a). The pin with the smoothest surface was observed in experiment P, conducted at 20 N and 300 RPM. Under this condition, the pin exhibited the lowest R_z and R_q values, although the R_t and R_a values were slightly higher than the minimum values recorded in other test conditions. However, for the disc, the roughness values were not the lowest under this same condition.
The best surface finish values for the wear track on the disc were achieved under condition M, i.e., 5 N and 300 RPM. At this test condition, the combination of the lowest load and highest speed results in reduced contact pressure, minimizing plastic deformation. Additionally, the shorter contact time between the mating surfaces due to the high speed leads to minimal wear.

However, the higher *Rz* and *Rt* values observed on the pin surface indicate adhesion and material transfer from the disc to the pin, a finding supported by the EDS analysis results.

Table 5.1 Roughness parameters of the surface profile for different parameters

Expt. ID	Load (N)	Speed (RPM)	(Pin)				(Disc)			
			R_z	R_q	R_t	R_a	R_z	R_q	R_t	R_a
			(Gaussian filter 0.25 mm)				(Gaussian filter 0.25 mm)			
A	5	150	16.7	2.84	35.3	1.44	10.8	2.57	15.6	2.01
B	10	150	8.65	2.41	9.63	1.98	6.06	1.35	6.96	1.13
C	15	150	11.8	3.18	16.8	2.65	7.35	1.82	7.97	1.57
D	20	150	10.7	3.22	11.8	2.82	5.38	1.18	6.87	0.97
E	5	200	9.38	3.02	15.4	2.51	11.1	2.91	17.3	2.34
F	10	200	9.90	2.68	11.6	2.24	5.68	1.49	6.56	1.32
G	15	200	10.8	2.85	14.1	2.25	8.48	2.36	10.5	1.94
H	20	200	11.0	2.62	15.3	2.06	6.78	1.65	8.80	1.29
I	5	250	18.4	5.08	33.3	4.02	6.71	1.65	8.14	1.33
J	10	250	10.9	3.19	15.1	2.75	7.13	1.87	10.4	1.64
K	15	250	7.70	2.23	9.42	1.91	5.40	1.21	6.55	1.00
L	20	250	7.35	2.06	10.4	1.73	11.5	3.08	15.1	2.51
M	5	300	27.3	4.46	34.1	2.88	5.00	1.14	5.96	0.88
N	10	300	16.1	3.52	22.4	2.72	9.65	2.26	18.1	1.79
O	15	300	10	2.7	13.5	2.31	12.1	2.55	22.3	1.97
P	20	300	7.19	1.96	9.60	1.57	5.17	1.47	8.81	1.18

At higher loads, this is attributed to the shearing of the peak regions on the pin surface, producing coarse wear debris that contributes to a rougher disc surface with reduced hardness. Figure 5.15 depicts the changes in maximum depth and height of the worn pin surface under conditions M and L. Analysing these figures alongside Table 5.2 shows that experiment A (5 N 150 RPM) exhibits the greatest peak depth and height. However, the profile area above and below the surface, as indicated in Table 5.2, is the smallest for this experiment, which can be attributed to reduced material adhesion at the lowest load and speed. At this low speed, the contact time between the mating surfaces is at its longest. Additionally, the profile areas above and below the surface for the pin worn under condition "J" are next highest, followed by condition "I," suggesting possible material deposition during subsequent passes of the pin [53].

For the highest load of 20 N, the wear is more pronounced at the lowest rotational speed of 150 RPM and the highest speed of 300 RPM, with a reduction observed between 200 RPM and 250 RPM.

Table 5.2 Peak and Valley parameters of the pin surface profile

Expt. ID	(Pin)			
	Maximum depth (µm)	Maximum height (µm)	Profile area below surface (µm^2)	Profile area above surface (µm^2)
A	16.7	58.6	275	275
B	42.0	34.5	911	910
C	12.5	27.4	4740	4738
D	24.5	19.8	4241	4242
E	17.6	23.6	5113	5121
F	30.2	26.4	4903	4921
G	18.5	24.7	5251	5248
H	11.3	13	1985	1977
I	25.1	36.9	7107	7065
J	34.7	47.3	7586	7530
K	15.7	17.8	3565	3568
L	10.7	8.06	2130	2120
M	25.6	33.6	5778	5758
N	30.8	29.1	5759	5742
O	7.98	13.4	2136	2137
P	17.1	21.1	4699	4701

Figure 5.14 shows the Line profile across the abraded pin surfaces after the test conditions 20N 250 RPM and 5 N 300 RPM respectively. The maximum height and maximum depth above and below the centre line along with the area above (shown by green) and below (shown by red) is as shown. Table 5.2 presents the main parameters describing the peak and valley features of the abraded pin surfaces for all the test conditions.

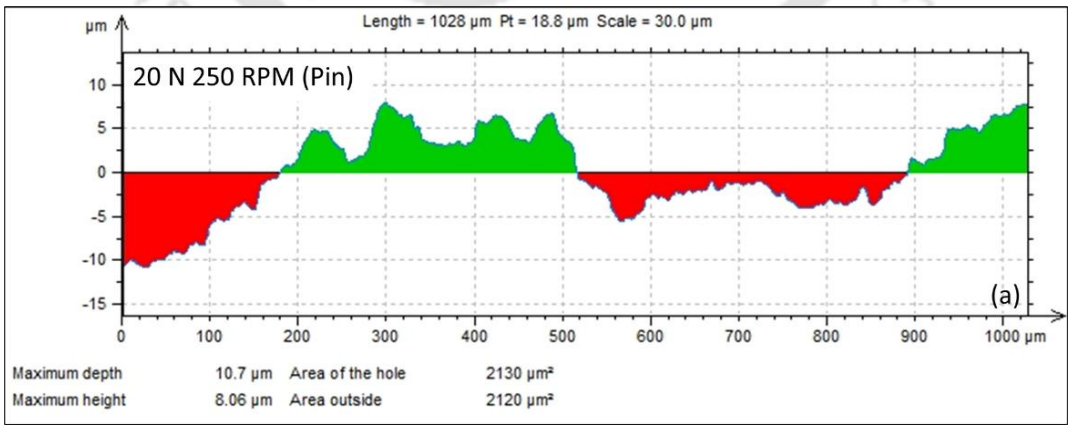

(a) 20 N 250 RPM

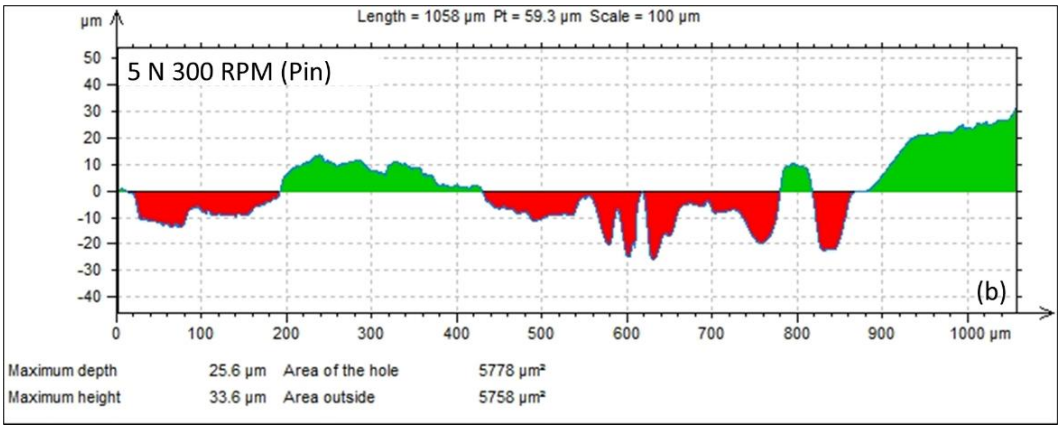

(b) 5 N 300 RPM

Figure 5.14 Line profile across the abraded surfaces

Figure 5.15 (a) illustrates the maximum height and depth of the worn surface, while Figure 5.15 (b) shows the areas above and below the mean line of the worn surface.

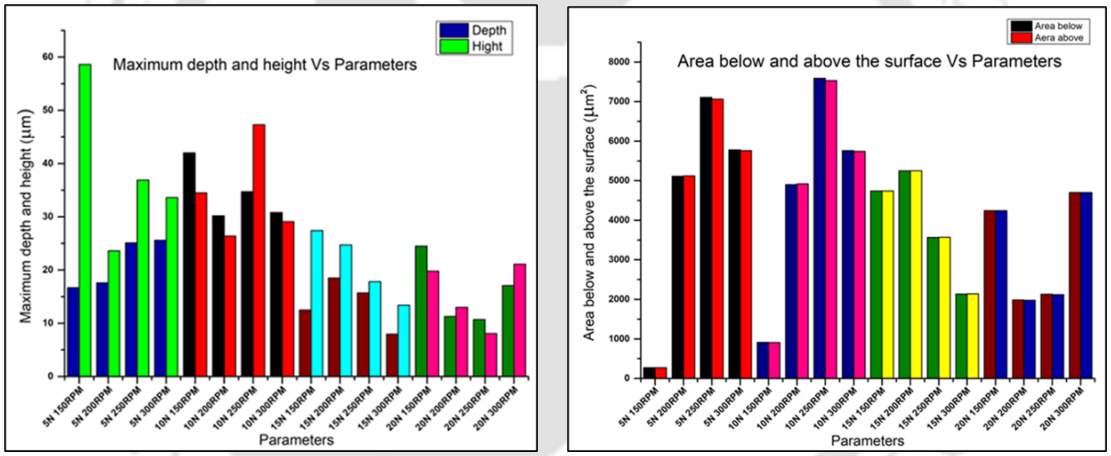

(a) (b)

Figure 5.15 Profilometry parameters of the pin surface worn by different parameters(a) Maximum depth and height of valley and peak(b) Area below and above the surface

For loads of 5 N and 10 N, these areas increase with RPM up to 250 RPM. However, when the load increases to 15 N, the areas begin to decrease after 200 RPM. The maximum peak height for the 5 N load decreases as the speed increases. The lowest peak height is observed in experiment L, while the smallest area above and below the surface is found in experiment A. Figure 5.15 (a) shows that experiment A has the greatest difference between maximum depth and height. This is likely due to significant roughness features on the surface, such as sharp peaks and deep valleys, which cause high maximum depth and height values. However, these

features may cover only a small area, leading to minimal changes in the overall surface area above and below the mean line.

5.6 Microstructure Evaluation

The microstructure of the material under similar service conditions has already been examined [9]. Samples exposed to 650°C exhibited no signs of cracks or creep cavities. It was confirmed that the examined section of the tube consists of equiaxed grains with a continuous carbide network along the grain boundaries.

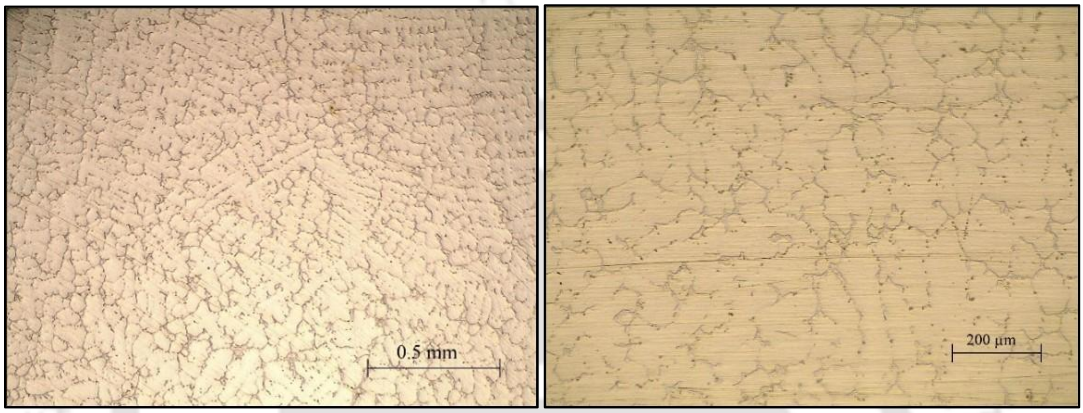

Figure 5.16 Microstructure of as received HP40Nb steel

Figures 5.16(a) and 5.16(b) show the microstructure of the samples. They reveal that the samples heated to 650°C remain structurally intact, exhibiting no damage from high-temperature stress and maintaining a stable grain structure.

5.7 Wear Debris Analysis

Wear debris collected after the test and analysed by different microscopes are as shown in Figure 5.17 (a) and (b) and Figure 5.18 (a) and 5.18 (b).

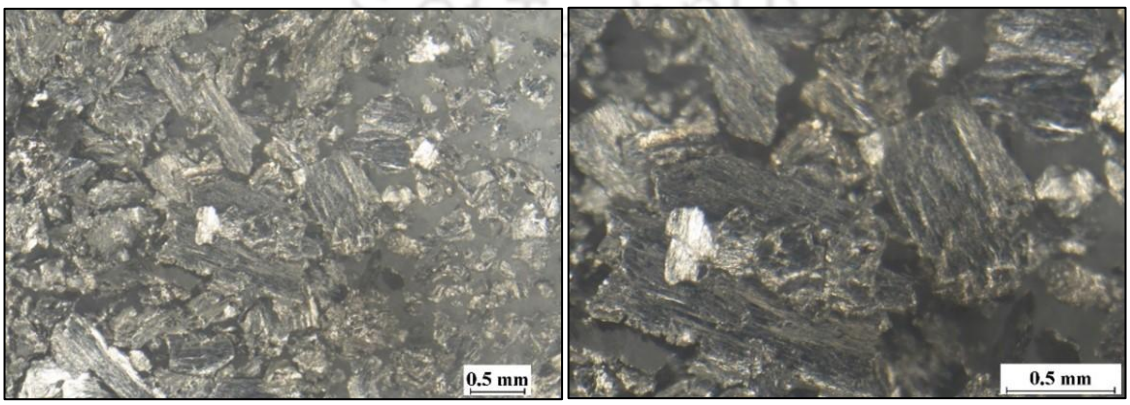

(a) (b)

Figure 5.17 Optical stereo zoom micrographs of wear debris

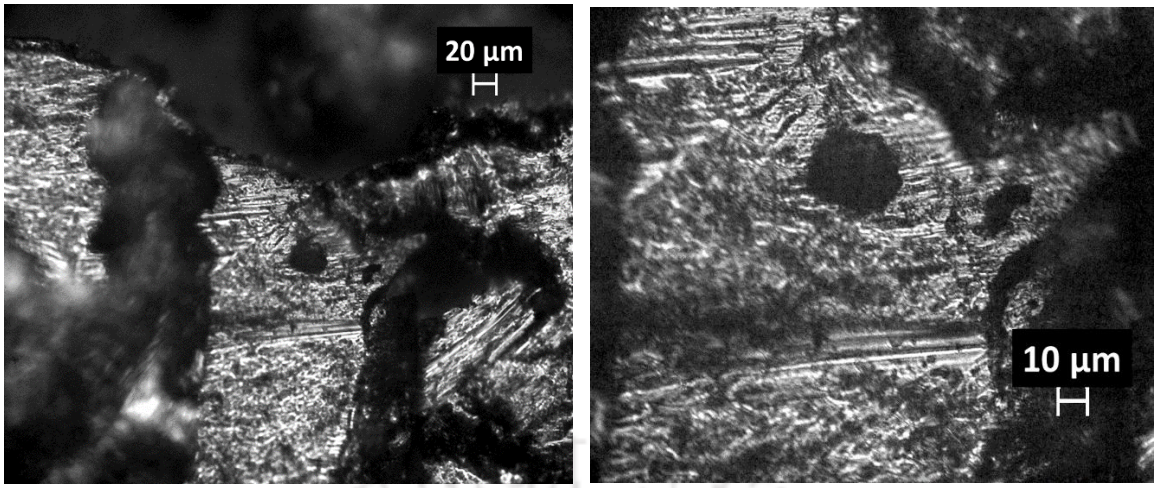

(a) (b)

Figure 5.18 Optical micrographs of wear debris

The investigation of wear debris was used to identify the mechanisms responsible for material volume loss in this tribo-system. Initially, large, irregularly shaped debris indicated abrasive wear. However, some debris flaked off from the contact surface due to a delamination mechanism [102]. Typically, plate-like wear particles form as the compacted layer flakes off during dry sliding wear testing, as illustrated in Figures 5.17 (a) and 5.17 (b).

5.8 Summary of chapter 5

The influence of load on COF at the lowest rotational speed, i.e., 150 RPM, is negligible. At higher speeds, the COF is higher at the lower load as compared to the higher load. The wear rate increases with an increase in load, and it increases with an increase in speed for most cases. At lower rotational speeds up to 250 RPM, the wear rate increased for 750 meters of sliding distance. However, at 300 RPM, this trend is not evident. Wear surface profile indicates maximum peak height at lower loads, which decreases with increased speed. The lowest peak height value is observed for the parameters 20 N /250 RPM, whereas the area below and above the surface is minimum for 5 N /150 RPM. The wear occurs by adhesion due to material transfer from the soft SS 316 disc to the hard HP40Nb pin. The mechanism of wear at lower speeds is by ploughing, micro cutting, and plastic deformation of the disc surface whereas at higher speeds, it is due to plastic deformation and metal transfer. The adhesive wear of the HP40Nb pin is due to material transfer from the softer disc to the pin followed by delamination resulting in the formation of micro-cracks on the material transferred at the pin surface. The wear debris analysis confirmed the abrasive wear, ploughing, as well as adhesive wear by forming compacted layer due to a delamination mechanism.

Chapter 6

Wear of Carburized HP40Nb SS

The results of the study on the effect of pack carburization on microstructure, hardness abrasive and adhesive wear etc, of HP40Nb steel is presented and discussed in this chapter. The abrasive and adhesive wear of carburized HP40Nb steel is presented and discussed in this chapter. The effect of different process parameters viz, speed, load and grit size (or sliding distance) on the wear rate and COF before and after carburization is compared and discussed. The results of wear rate of HP40Nb before and after carburization are compared with HSS and SS304.

6.1 Microstructure after carburization

Figure 6.1 (a) and (b) shows higher magnification optical micrographs of the carburized layer of HP40Nb Pin. Figure 6.1 (b) reveals features typical of eutectoid structure. This is attributed to the carbon diffusion through the grain boundaries during the carburization heat treatment resulting in higher amounts of carbides at grain boundary regions. The addition of carbon on the surface makes the diffusion of carbon forming the carbides such as chromium carbide, niobium carbide etc. Presence of precipitates are evident at the regions of grain boundaries. Earlier investigation in the author's lab reported Cr-rich, Nb-rich and (Nb, Ti) rich carbides at grain boundaries of the as-received reformer pipes [12, 103].

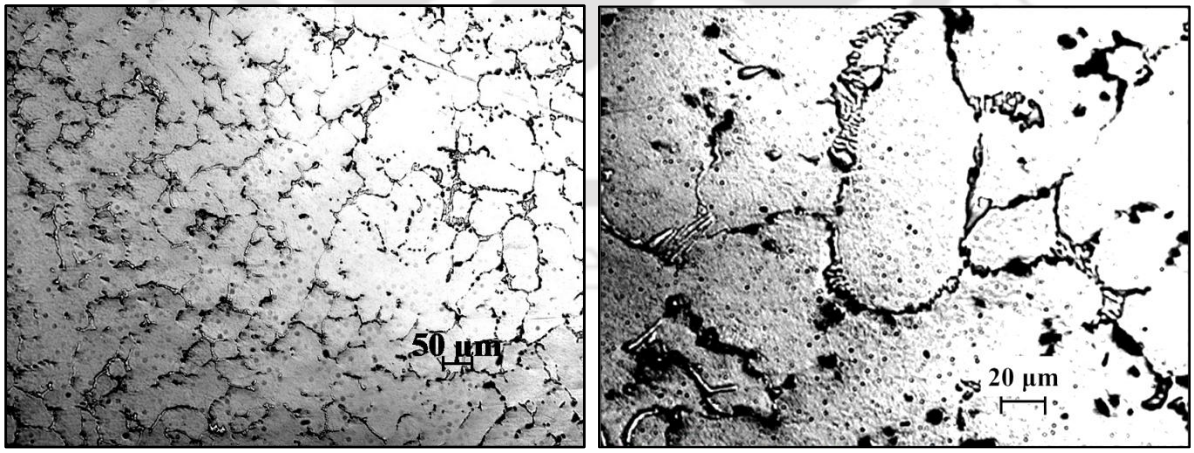

(a) (b)

Figure 6.1 Optical micrographs of the carburized HP40Nb steel

Figure 6.2 shows the SEM images of the HP40Nb reformer samples before and after carburization. Microstructure reveals precipitates at the grain boundaries of the austenite matrix. A typical microstructure of HP alloys is an austenite matrix with intergranular eutectic-like primary chromium carbides of M_7C_3 and / or $M_{23}C_6$ and MC type of niobium carbides [16].

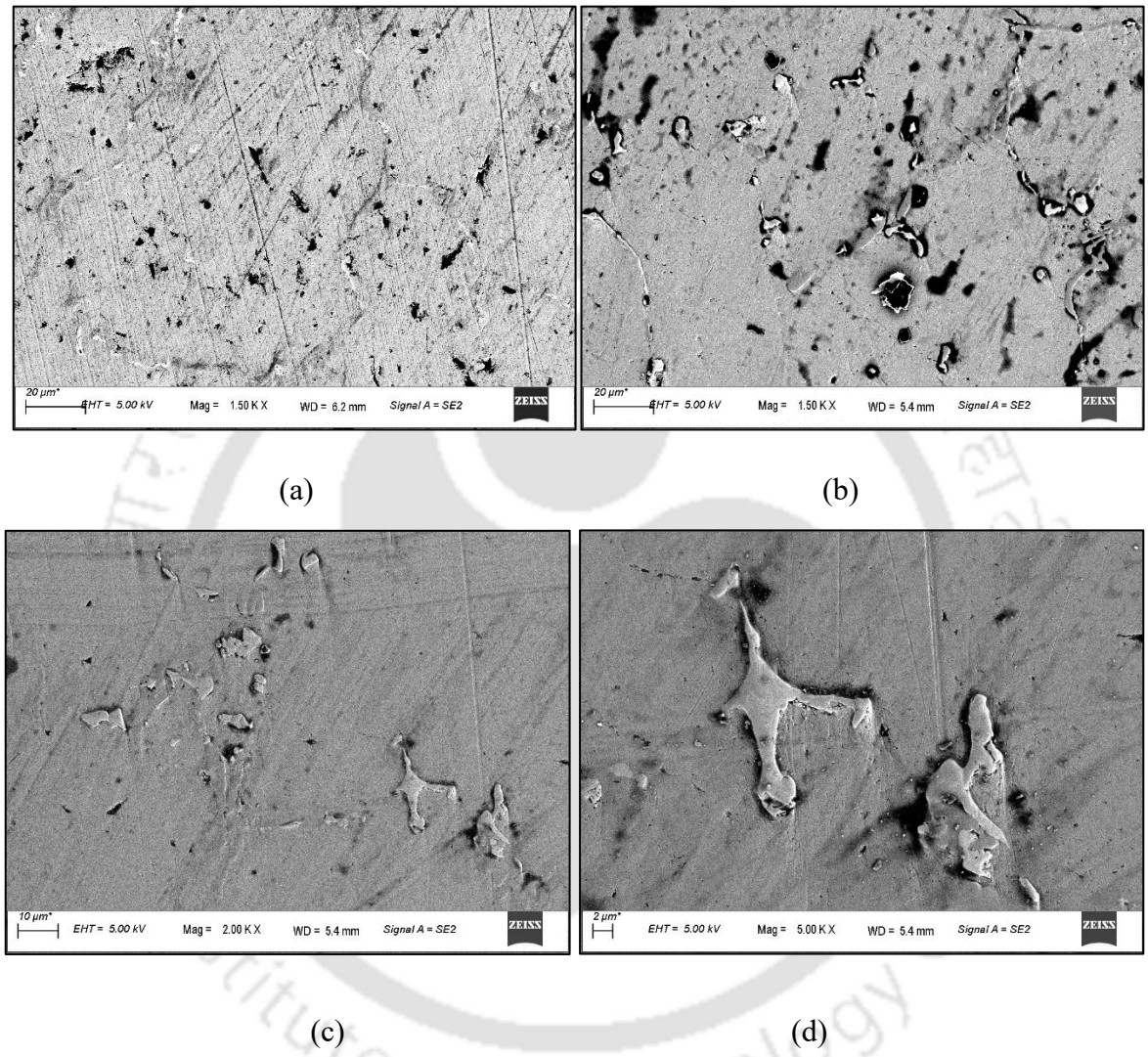

Figure 6.2 SEM images of specimen (a) before and (b), (c), (d) after carburization

Low magnification optical micrographs of the as received and carburized HP40Nb steel, are shown respectively in Figs 6.3 (a) and (b). Micrographs reveal a thin carburized layer at the outer surface of the carburized sample, as is evident from Fig 6.3 (b). The two figures reveal that the microstructure of the core is dendritic structure and that no change in the microstructure had taken place as a result of the carburization heat treatment.

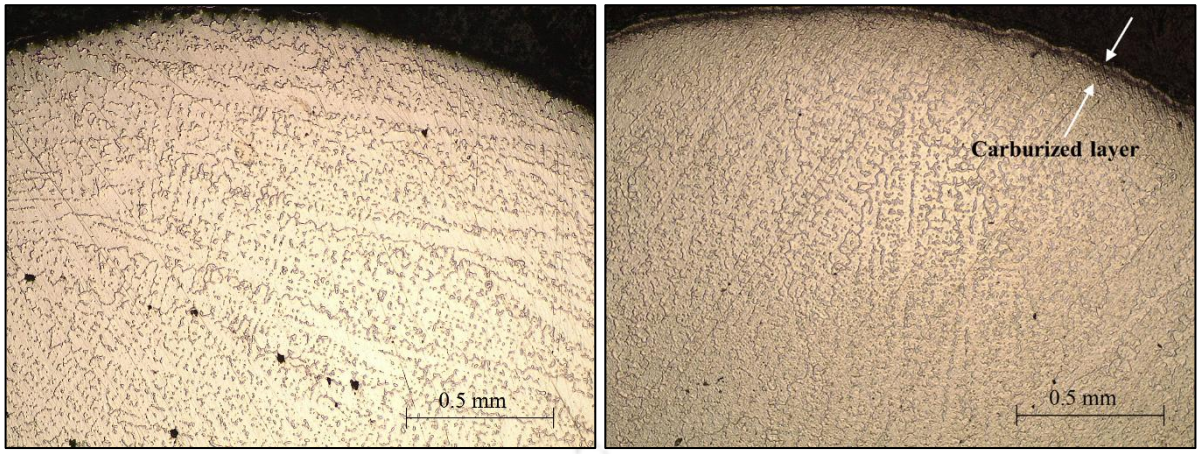

(a) (b)

Figure 6.3 Optical micrographs of HP40Nb pin in (a) as-received condition and (b) after carburization

An SEM image along with a typical electron dispersive X-ray (EDS)spectrum of an area in the carburized layer, near to the surface of the carburized specimen are shown in figures 6.12. The spectrum reveals presence of chromium, niobium, titanium, etc, along with high amount of carbon indicating the presence of carbides of these elements.

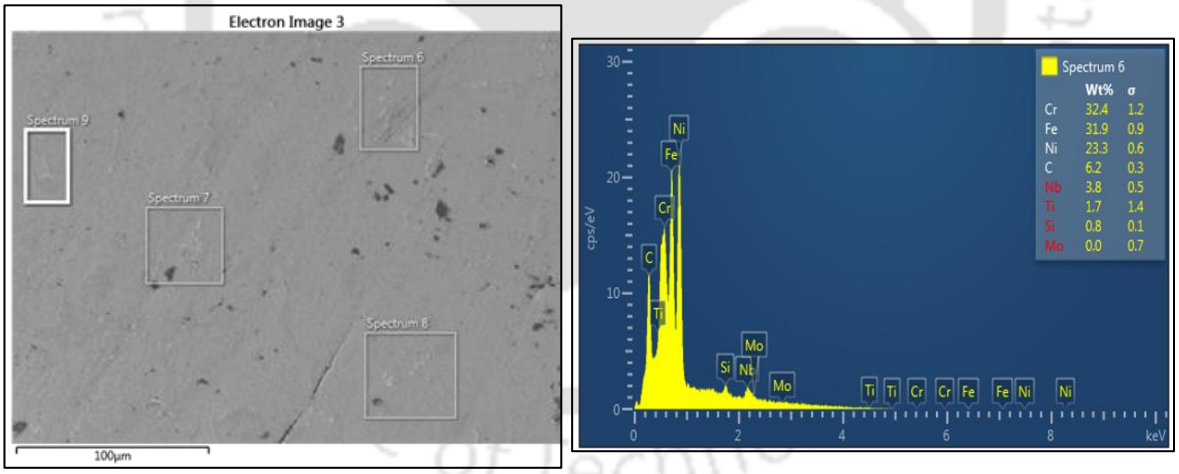

(a) (b)

Figure 6.4 EDS spectrum of carburized surface at edge

6.1.1 Hardness Test Results

Figure 6.5 show the hardness vs distance plot from the surface of HP40Nb steel before and after carburization heat treatment. The surface hardness of the as-received sample was 257.4 ± 24 HV. The hardness of surface increased 492 ± 4 HV after carburization heat treatment, i.e.,

an increase in hardness by around 91%. The hardness of the heat treaded steel decreased with distance away from the surface. Even at 3 mm depth from the surface, the hardness of the heat treated alloy was higher than the as-received alloy. A similar trend is in reported in literature [90, 103].

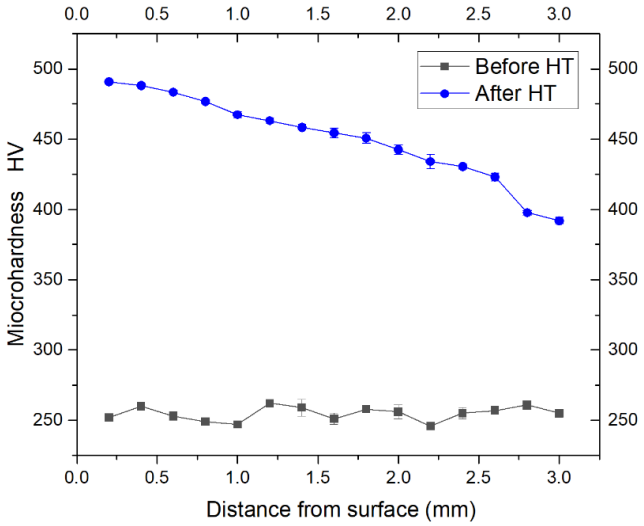

Figure 6.5 Variation of hardness Vs distance from surface.

6.1.2 XRD Analysis

The XRD analysis of the samples performed before and after carburization is done the figure shows the XRD graphs of the samples before and after the carburization process.

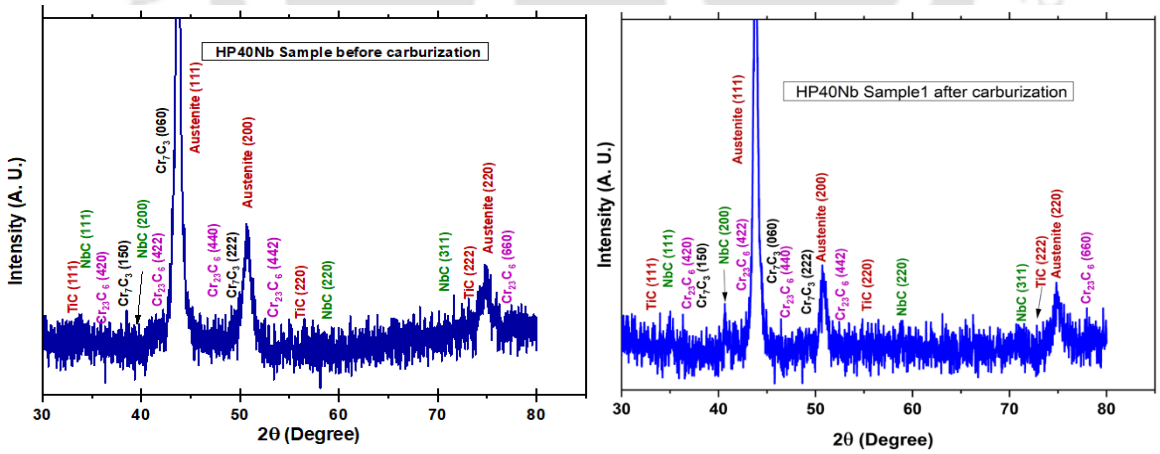

(a) (b)

Figure 6.6 XRD pattern of samples before and after surface carburization

Figure 6.6 (a) and (b) shows the XRD pattern of the as received and carburized HP40Nb steel, respectively. The peaks were indexed w.r.t to the JCPDS files. In both cases, presence of NbC,

TiC, $Cr_{23}C_6$, Cr_7C_6 are evident in the austenitic phase. These are the carbides present at the grain boundary regions seen in the micrographs of Figures 6.1.

6.2 Abrasive Wear Analysis

The wear rate and COF before and after carburization heat treatment (HT) of HP40Nb steel along with the standard deviations are depicted in Table 6.1.

Table 6.1 Output parameters before and after HT (Abrasive wear)

Expt. ID	Input parameters			Output parameters							
	Grit size (G)	Load (N)	Speed (RPM)	wear Rate after HT (mm^3/m)	Std. Deviation	Wear rate before HT (mm^3/m)	Std. Deviation	COF (μ) after HT	Std. Deviation	COF (μ) before HT	Std. Deviation
A.	600	10	200	0.00057	0.000009	0.00074	0.00001	0.24	0.07	0.54	0.02
B.	600	20	200	0.00101	0.00002	0.0013	0.00002	0.32	0.06	0.36	0.05
C.	320	20	200	0.02117	0.00003	0.02911	0.0003	0.35	0.04	0.45	0.04
D.	320	10	200	0.00385	0.00005	0.02192	0.0004	0.32	0.01	0.65	0.05
E.	320	10	150	0.00559	0.00001	0.02322	0.0005	0.25	0.04	0.61	0.08
F.	320	10	250	0.01018	0.00002	0.02409	0.0003	0.55	0.03	0.66	0.04
G.	600	10	250	0.00045	0.00003	0.00061	0.00001	0.22	0.08	0.54	0.03
H.	600	20	250	0.00127	0.00002	0.00165	0.0002	0.26	0.08	0.42	0.04
I.	600	10	150	0.00042	0.00001	0.00052	0.00003	0.22	0.04	0.38	0.03
J.	400	20	250	0.00262	0.00012	0.01166	0.00008	0.38	0.07	0.48	0.06
K.	400	10	200	0.00179	0.00006	0.00211	0.00007	0.26	0.08	0.53	0.02
L.	400	10	250	0.00227	0.0001	0.00544	0.00004	0.2	0.05	0.55	0.04
M.	400	20	150	0.00244	0.0002	0.00431	0.00002	0.23	0.09	0.39	0.06
N.	400	20	200	0.00231	0.0003	0.00812	0.00005	0.32	0.06	0.47	0.04
O.	320	20	250	0.02270	0.0008	0.03028	0.00001	0.56	0.01	0.62	0.04
P.	600	20	150	0.00113	0.00001	0.00175	0.00007	0.31	0.03	0.34	0.06
Q.	400	10	150	0.00117	0.00001	0.00141	0.00001	0.19	0.02	0.56	0.02
R.	320	20	150	0.01707	0.0007	0.02794	0.00001	0.43	0.05	0.75	0.05

6.2.1 Effect of Process Parameters on Abrasive Wear Rate

The wear rate before and after the heat treatment obtained under various process parameters is illustrated in Table 6.1. A significant reduction in wear rate of the reformer steel pin samples is evident after the carburization treatment. The result reveals that, before and carburization heat treatment, among the grit sizes used for the tests, the highest wear rate is observed while

using grit size 320 followed by 400 and 600, in order. Similar trend is reported in bainitic steel, martensitic steel, ferritic steels [36] and EN S235JR steels [39]. Study on bearing steel [7] revealed that as the size and depth of penetration of abrasive particles grow, the primary wear mechanisms shift from cutting to ploughing, with wedge formation in between resulting in an increase in abrasive wear rate. The trend in the increase in wear rate with an increase in load for all grit sizes before and after heat treatment has been observed in other types of steels [36, 38, 39].

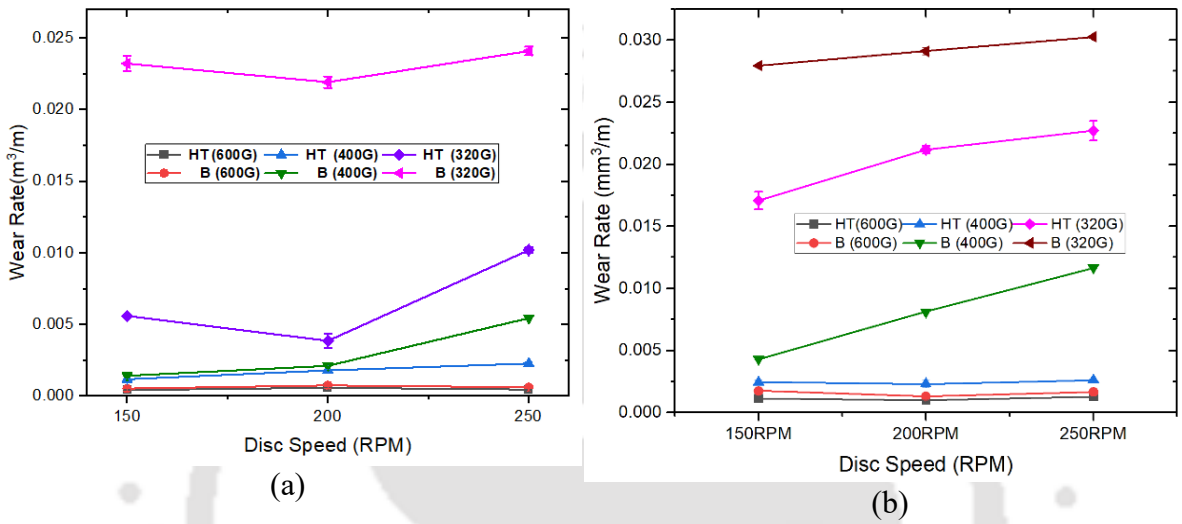

Figure. 6.7 Plots of wear rate vs disc speed at load (a) 10 N and (b) 20 N

In the present study, at higher load conditions, the wear rate increases with an increase in rotational speed. However, for Load 10 N and grit size 320 G (10 N/320 G), the wear rate reduces from the rotational speed is increased from 150 to 200 RPM. This trend is same in both the test conditions before and after the carburization heat treatment. The wear rate increases with subsequent increase in speed. The wear rate decreases up to 200 RPM & 10 N load only when tested with the abrasive disk of 320 grit size (coarser particles). Beyond 200 rpm, the wear rate increases both in the as received condition as well as in the heat treated condition. This is due to the reason that during the initial stages of testing, the coarser particles breaks resulting in decrease in the wear rate. However, with further increase speed, the broken abrasives particles also contributes to the wear phenomenon resulting in increase in the wear rate.

Figures 6.7 (a) and (b) indicates that the wear rate decreases significantly after the heat treatment. At 10 N/ 200 RPM, the average and maximum reduction in wear rate observed by carburization heat treatment is ~42% and ~82%, respectively, while using 320 G abrasives. At

20 N load the maximum reduction in wear rate is 72% and average reduction in wear rate is 41%. This result has already been published [12]. Significant reduction is wear rates by carburizing low carbon steels have been reported in the literature [31].

6.2.2 Effect of Process Parameters on Coefficient of Friction (COF)

Figures 6.8 (a) & (b) illustrates the variation in the COF before and after the carburization heat treatment. Heat treatment leads to a substantial decrease in the COF at the pin-disk interface. At test conditions of 150 RPM/10N, the COF is higher for 600 G as compared to 400G the HP40Nb steel before and after carburization. Similar observation is seen at 250RPM /10N test condition before carburization. With 320G abrasive surface and 150 RPM/10 N test condition, the COF decreases by 59% after the carburization heat treatment whereas at 250RPM/10N, the decrease in the COF is only 16.7%. Using the fine abrasive (600 G), the decrease in COF at 150 RPM and 250 RPM at 10N load are 42% and 59%, respectively.

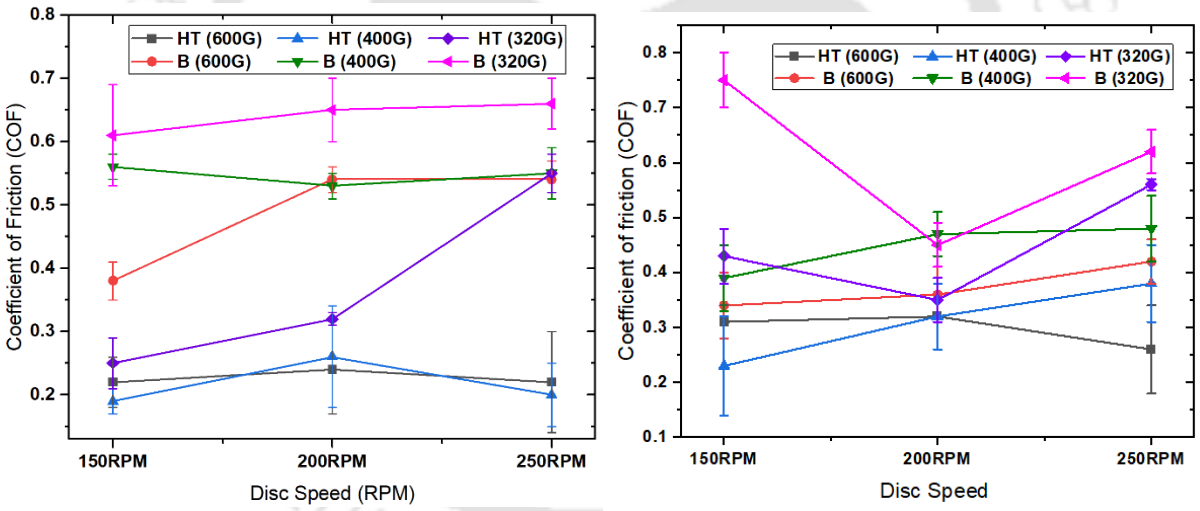

Figure 6.8 Plots of COF vs Disk speed at load (a) 10 N and (b) 20 N

Figure 6.8 (b) reveals that the variation in COF before and after heat treatments at a normal load of 20 N. The reduction in COF after the heat treatment reduces with an increase in RPM increased while using the abrasive grits of size 320 G and 400 G. The reduction in COF before and after the heat treatment at 150 RPM for 320 G and 400 G was 42.7% and 41% respectively, which reduced further as speed increased. During testing using 600 G the reduction in COF increased gradually to 38.1 % while increasing RPM from 150 RPM to 250 RPM. Not all abrasive grains actively play a role in material removal during the wear process; some simply

cause plastic deformation of the pin surface without directly contributing to wear. However, by modifying the surface roughness, they can still impact the wear process driven by other grains [38].

It has been reported that as abrasive particle size increases, there is a rise in pressure and plastic deformation at each abrasive grain, consequently leading to an increase in the friction coefficient [37]. It is worth to note that, there is a transition in wear mechanisms from adhesive to abrasive, as demonstrated in various studies, that explains the transition of wear mechanism from a cutting mode to sliding wear [37, 38, 41].

6.1.3 Surface Morphology of the Worn Surface

The surface morphology of the specimen after abrasive wear tests were analysed using optical microscope (OM). Figures 6.9 to 6.11 illustrate the worn surfaces of the pin under different process parametric combinations. Micrographs of the surfaces before heat treatment, shown in figure 6.9, figure 6.10 and figures 6.11 (a) & (b), reveals features typical of abrasive wear such as ploughing and cutting. Material displacement due to plastically impressed continuous grooves is dominant in the worn pin samples post carburization [12].

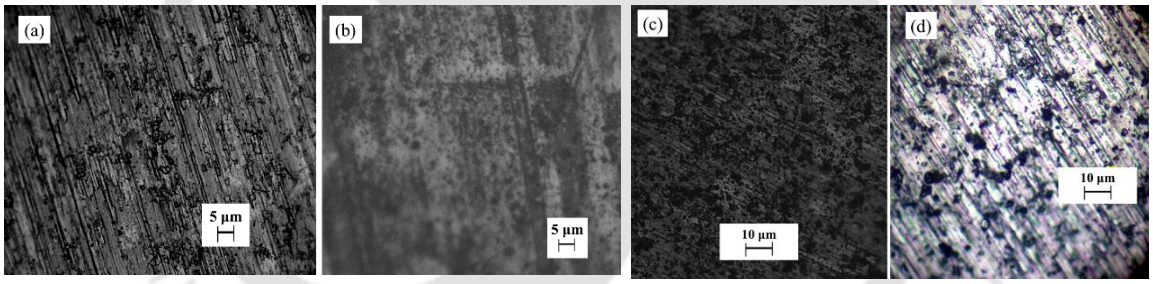

Figure 6.9 Optical micrographs of HP40Nb steel surface at (a & b) 320 G 10 N 200 RPM and (c & d) at 320 G 20 N 250 RPM. (a) & (c) refers to before heat treatment and (c) and (d) refers to after heat treatment

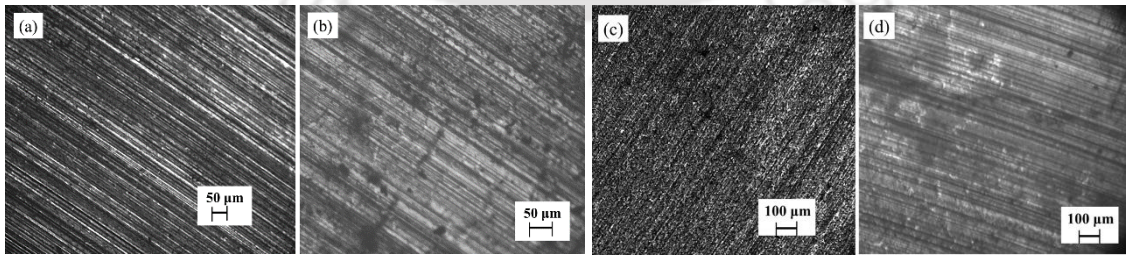

Figure 6.10 Optical micrographs of HP40Nb steel surface at (a & b) 400 G 10 N 200 RPM and (c & d) at 400 G 10 N 250 RPM. (a) & (c) refers to before heat treatment and (c) and (d) refers to after heat treatment

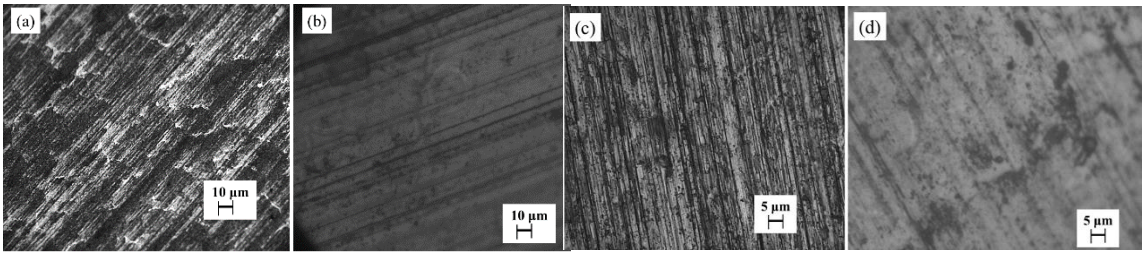

(i) 600 G 10 N 150 RPM (ii) 600 G 20 N 250 RPM

Figure 6.11 Optical micrographs of HP40Nb steel surface at (a & b) 600 G 10 N 200 RPM and (c & d) at 600 G 20 N 250 RPM. (a) &(c) refers to before heat treatment and (c) and (d) refers to after heat treatment

During chip cutting and rubbing processes, wear debris accounts for the removal of 40% of the total groove volume while the rest is displaced by plastic flow [40]. Larger abrasive particles penetrate deeper than smaller ones, leading to scratches that are often discontinuous due to the damage caused by the abrasive grains. It's important to note that not all abrasive grains directly contribute to material removal. Some grains may merely plastically deform the surface without contributing to wear. However, by altering the surface roughness, these grains can influence the wear process initiated by other grains [38].

6.1.4 Surface Topography of the Abraded Surfaces

The surface roughness of the post wear samples using the surface profilometer (Model: Form Talysurf; Make: Taylor Hobson Co.) Surface profilometry across a constant cross section (852µm × 852µm) of the pin surface before and after the heat treatment.

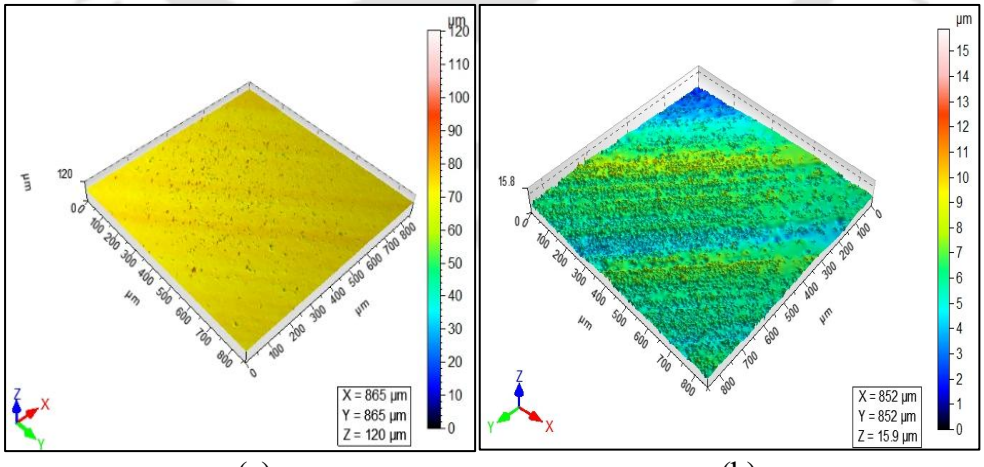

(a) (b)

Figure 6.12 3D profile of the wear surfaces worn by parameters 320 G 10 N 150 RPM (a) prior heat treatment (b) post heat treatment

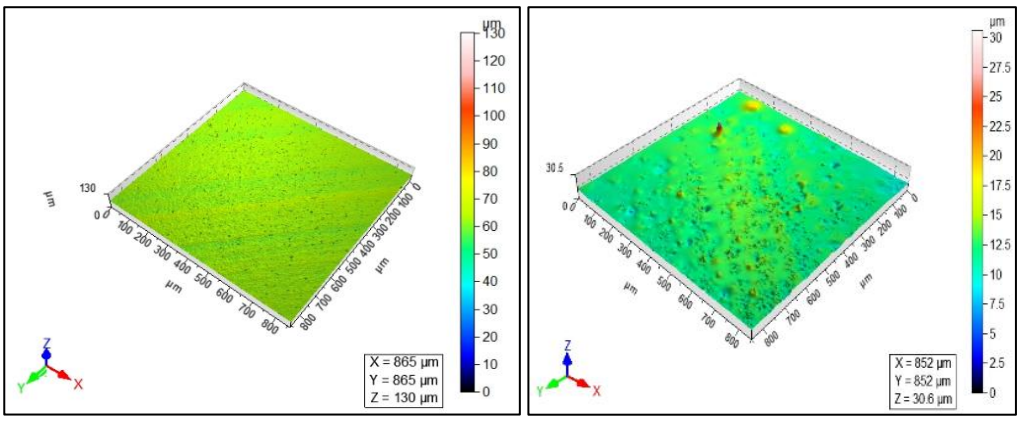

(a) (b)

Figure 6.13 3D profile of the wear surfaces worn by parameters 320 G 10 N 200 RPM (a) prior heat treatment (b) post heat treatment

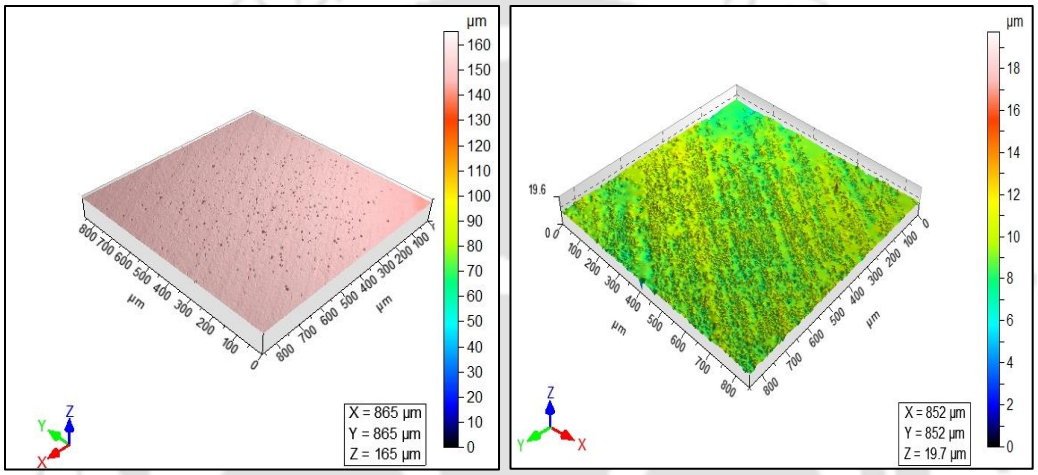

(a) (b)

Figure 6.14 3D profile of the wear surfaces worn by parameters 400 G, 10 N, 250 RPM (a) prior heat treatment (b) post heat treatment

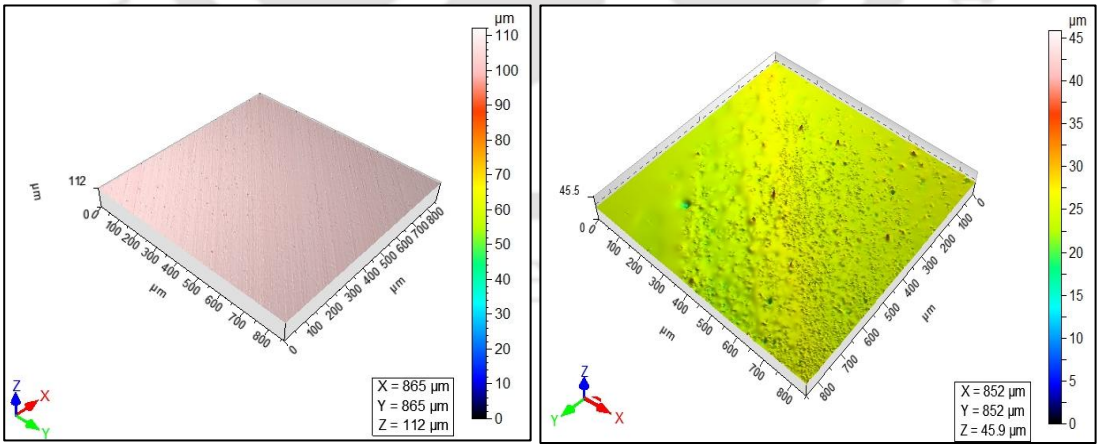

(a) (b)

Figure 6.15 3D profile of the wear surfaces worn by parameters 600 G 20 N 200 RPM (a) prior heat treatment (b) post heat treatment

Figures 6.12 to 6.15 illustrate the surface profile of the pin and disc after wear testing under different load and rpm conditions. A significant reduction in the *Z* value in the worn surfaces

of the heat-treated samples is noted. It is due to the rise in the surface hardness of the carburized HP40Nb pin samples. For the test condition as shown in figures 6.12 (a) and (b) 320 G, 10 N, 150 RPM, the Z values before heat treatment and after heat treatment are 120 µm and 15.9 µm respectively. It is 86.75% reduced in the post carburized sample. Similar observations are seen in all the test samples [12].

6.3 Adhesive Wear Analysis

The effect of load, rpm, sliding distance and COF on adhesive wear is discussed in the following sub-sections. Table 6.2 shows the effect of various parameters on adhesive wear before the carburization heat treatment.

Table 6.2 Output parameters before HT (Adhesive wear)

Input Parameters			Output Parameters (Before HT)								
Expt. ID	Load (N)	RPM	COF	Std. Dev. (COF)	Wear Rate (mm^3/m)	Std. Dev. (Wear Rate)	WR250 (mm^3/m)	WR500 (mm^3/m)	WR750 (mm^3/m)	WR 1000 (mm^3/m)	WR1250 (mm^3/m)
A.	15	300	0.71	0.06	0.002361	0.000057	0.00112	0.00259	0.003866	0.001868	0.003321
B.	15	200	0.73	0.073	0.002056	0.000044	0.00047	0.00197	0.002387	0.003399	0.001142
C.	10	200	0.64	0.013	0.001667	0.000066	0.00104	0.00174	0.002179	0.001712	0.003632
D.	10	150	0.74	0.04	0.00179	0.000047	0.00070	0.00174	0.002257	0.002465	0.003295
E.	20	200	0.7	0.069	0.002277	0.000026	0.00119	0.00215	0.003165	2.59E-03	0.001894
F.	15	150	0.75	0.06	0.002711	0.00008	0.00145	0.00184	0.003658	0.003892	0.001505
G.	10	300	0.53	0.067	0.001557	0.00007	0.00096	0.00272	0.001479	0.001064	0.001012
H.	20	150	0.76	0.028	0.002899	0.00008	0.00132	0.00169	0.003762	0.004826	0.002672
I.	20	300	0.71	0.065	0.002971	0.00009	0.00176	0.00296	0.003243	0.003917	0.004748
J.	15	250	0.66	0.049	0.001673	0.000047	0.00083	0.0013	0.002127	0.002413	0.00262
K.	10	250	0.71	0.05	0.001096	0.000053	0.00068	0.00112	1.58E-03	0.001012	0.001167
L.	20	250	0.69	0.044	0.003418	0.000079	0.00221	0.0033	0.003399	4.77E-03	0.004255

Table 6.3 shows the effect of various parameters on adhesive wear after the carburization heat treatment.

6.3.1 Effect of Process Parameters on Coefficient of Friction (COF)

The variation of COF before and after the surface hardening is as shown in figures 6.16 (a) and (b). The COF has negligible effect on load at 150 RPM before heat treatment. Considerable reduction in coefficient of friction is observed after heat treatment. However, at the same rpm, the heat treated samples indicates an increase in the COF as the load is increased from 10 N to 20 N. At 200 RPM, COF increases with increase in the load from 10 N to 15 N and with further increase in the load, it starts decreasing. The variation in the COF for after carburization heat treatment indicates the same trend as before carburization heat treatment.

Table 6.3 Output parameters after HT (Adhesive wear)

Input Parameters			Output parameters (after HT)								
Expt. ID	Load (N)	RPM	COF	Std. Dev. (COF)	Wear Rate k (mm^3/m)	Std. Dev. (Wear Rate)	WR250 (mm^3/m)	WR500 (mm^3/m)	WR750 (mm^3/m)	WR 1000 (mm^3/m)	WR1250 (mm^3/m)
A.	15	300	0.33	0.03	0.001284	0.000045	0.000467	0.000337	0.000221	0.000259	0.000285
B.	15	200	0.57	0.06	0.001505	0.00003	0.000519	0.000272	0.000324	0.000389	0.000415
C.	10	200	0.49	0.04	0.00131	0.000064	0.00013	0.00035	0.000311	0.000519	0.001881
D.	10	150	0.22	0.05	0.00118	0.000044	0.000143	0.000195	0.000454	0.000389	0.00013
E.	20	200	0.54	0.03	0.00173	0.00002	0.000636	0.00013	0.000143	6.49E-05	0.00013
F.	15	150	0.36	0.06	0.001323	0.000026	0.000285	0.000519	0.000311	0.000208	0.000519
G.	10	300	0.48	0.06	0.001206	0.000024	0.000506	0.000104	0.000441	0.000156	0.000675
H.	20	150	0.54	0.06	0.002127	0.00008	0.000182	0.000519	0.000636	0.000791	0.000882
I.	20	300	0.58	0.03	0.002374	0.00001	0.000726	0.000571	0.000532	0.000545	0.000584
J.	15	250	0.18	0.04	0.000804	0.00007	0.000169	0.000182	0.000285	0.000169	0.000195
K.	10	250	0.5	0.07	0.000778	0.000023	6.49E-05	0.00013	6.49E-05	0.000519	0.000649
L.	20	250	0.47	0.07	0.002231	0.00009	0.000467	0.001154	0.000519	9.08E-05	0.000246

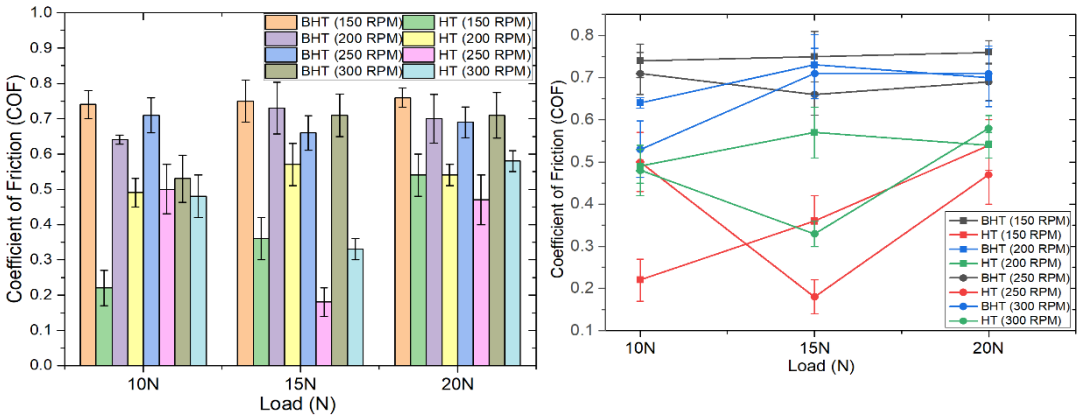

(a) (b)

Figure 6.16 Variation of COF vs load before and after HT under different RPM

6.3.2 Effect of Load and RPM on Wear Rate

Figure 6.17 (a) and (b) depicts the effect of load and RPM on wear rate. At all rpms, the wear rate (*k*) increases with increase in load before as well as after the carburization heat treatment. A remarkable reduction in wear rate is observed in the heat treated samples e. g., at 150 RPM, the average reduction in wear rate observed due to the carburization heat treatment is ~34%. Before the heat treatment, the highest and lowest wear rate (0.003418 $mm^3\ m^{-1}$ and 0.001096 $mm^3\ m^{-1}$, respectively) for is observed when tested at 250 RPM at loads 20 N and 10 N, respectively. After heat treatment, the highest and lowest wear rate (0.002374 $mm^3\ m^{-1}$ and 0.000778 $mm^3\ m^{-1}$, respectively) for is observed when tested at 20 N/ 300RPM and 10 N/250 RPM, respectively.

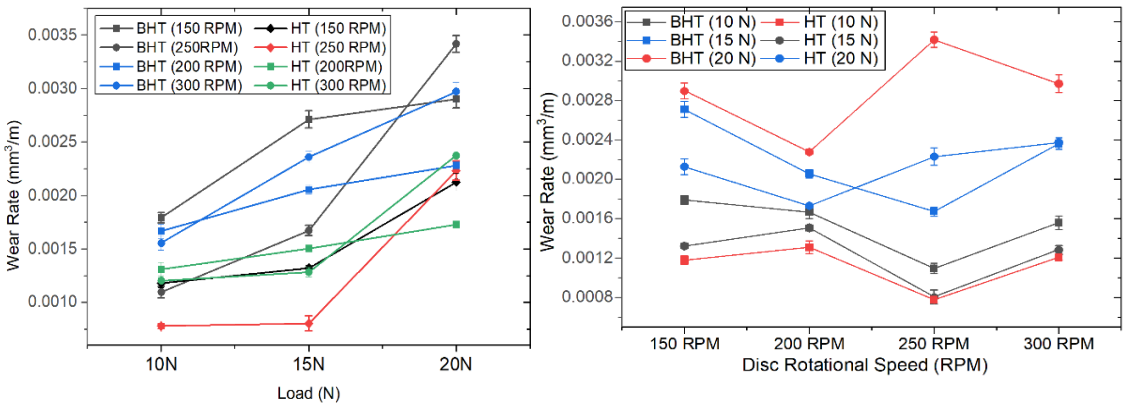

(a) (b)

Figure 6.17 (a) Wear Rate Vs Load (b) Wear Rate vs RPM

The results clearly indicates reduction in wear rate due the carburization heat treatment. It is generally known that even the smooth surface of metallographically polished surface is not smooth microscopically. Real surfaces consists of hills and valleys which, when compared to the atomic scale, are very large [96]. As the two mating surfaces come in contact with each other, the hill regions (or asperities) of the two surfaces come in contact and the actual contact area between the two surfaces are the sum of the area of contact of all asperities. The actual contact area will be far less than the apparent contact area. As the load increases, the plastic deformation occurs at contact points of asperities leading to an increase in the actual contact area between surfaces. This promotes greater material transfer and accelerates wear. As per Archard's wear equation (eq. 2.1) wear rises with higher loads and longer sliding distances but decreases with increase in hardness [11, 97].

Since the hardness of the carburization heat treated samples are much higher (around 91% higher) than the as-received material, the wear rate decreases with carburization heat treatment. It is noted that from Fig. 6.17 (b), the wear rate decreases as the speed increases from 150 to 200 RPM for all loads before and after carburization heat treatment except for the heat treated samples tested at 10 and 15N. The wear rate increases as speed increases from 250 RPM to 300 RPM for all load conditions before and after carburization heat treatment with the exception of the non-heat treated sample tested at 20 N /300RPM heat treated samples. High sliding velocities and/or high contact pressures generate heat due to the friction at the contact surface, leading to the formation of a low shear strength surface film or even local melting. In contrast, softening at interface can enhance ploughing in the softer material by the hard debris. The interplay of these factors makes predicting the effect of sliding velocity on friction more complex [94].

6.3.3 Effect of Sliding Distance on Adhesive Wear

The relative wear rate vs sliding distance (as per the method described in section 3.6.2) at loads of 10 N, 15 N and 20 N before and after carburization surface treatment is plotted in figures 6.18 (a) to (c). As mentioned in Section 5.1.5, a gradual increment in the relative adhesive wear rate, for the as-received steel, is observed as the speed is increased from 150 RPM to 250 RPM for sliding distances in the range 0-250 m, 250 m to 500 m and 500 to 750 m. Beyond the sliding distance of 750 m, no specific trend in the wear rate is observed for the as-received material. For the heat treated specimen, the variation wear rate with sliding distances were only marginal. The wear rate data for the test conditions were falling in a very narrow range.

The marginal difference in the relative wear rate with sliding distance is mainly due to the high and uniform surface hardness. The point to be noted is that the heat treated samples exhibits very low wear rate compared to the non-heat treated sample.

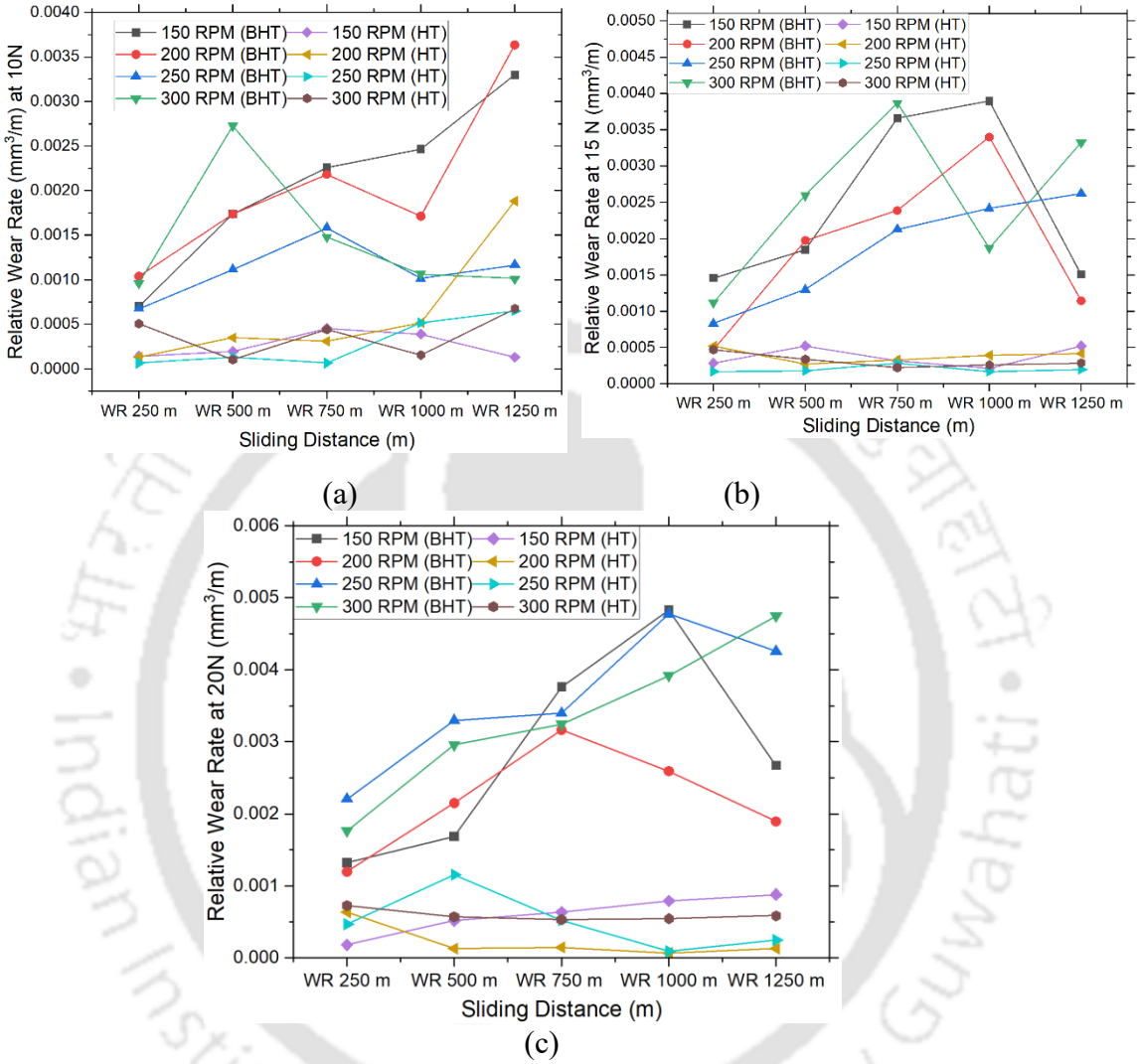

Figure 6.18 Relative Wear Rate vs. Sliding distance at (a) 10 N (b) 15 N (c) 20 N

6.3.4 Surface Morphology of the Worn Pin and Disc Surfaces

Figures 6.19 (a) to (d) shows the OM micrographs of the heat treated surfaces of HP40Nb pin after wear testing under different conditions. Figure 6.19 (a) reveals features typical of material transfer from the soft disk to the hard pin surface during the sliding test. The different images show different features under different test conditions, such as plastic deformation, metal transfer, delamination etc, which are typical of adhesive wear.

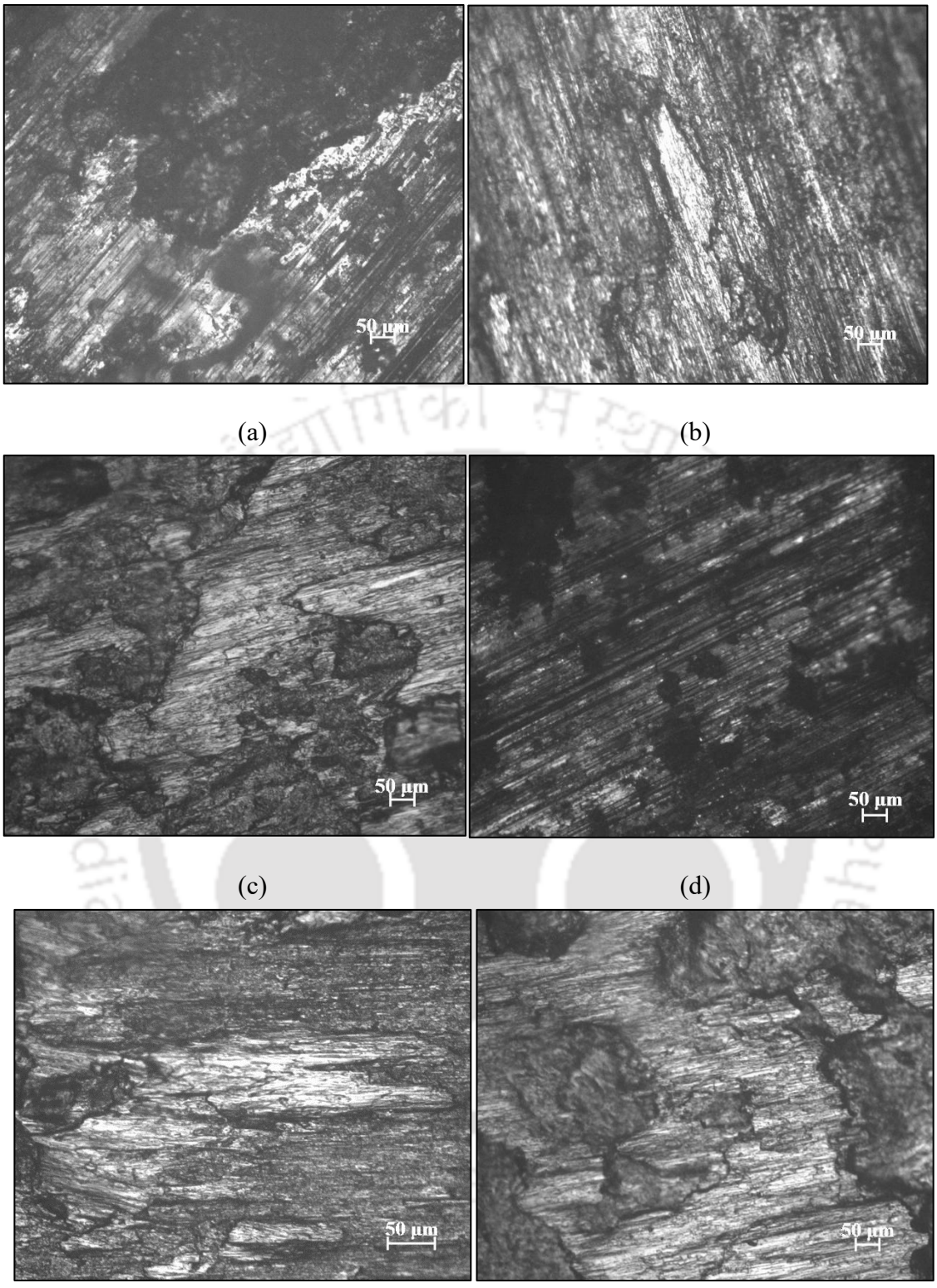

Figure 6.19 Worn out surfaces of heat treated HP40Nb pin samples by various parameters (a) 10 N 150 RPM (b) 15 N 150 RPM (c) 15 N 200 RPM (d) 15N 250 RPM (e) 10 N 250 RPM (f) 20 N 300 RPM

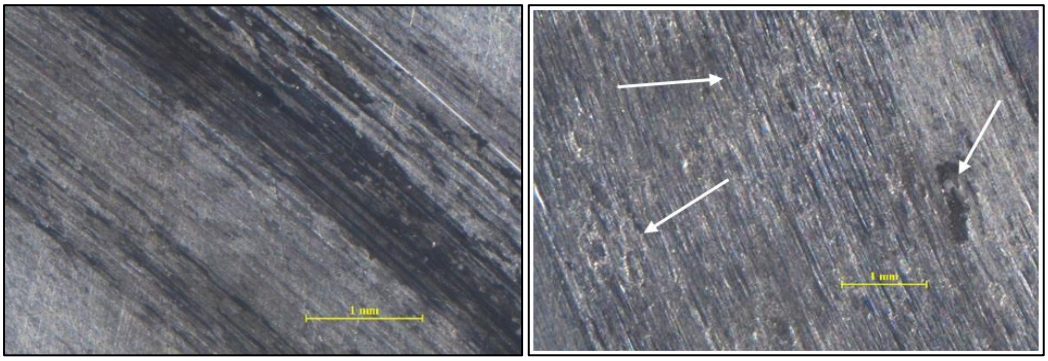

(a) (b)

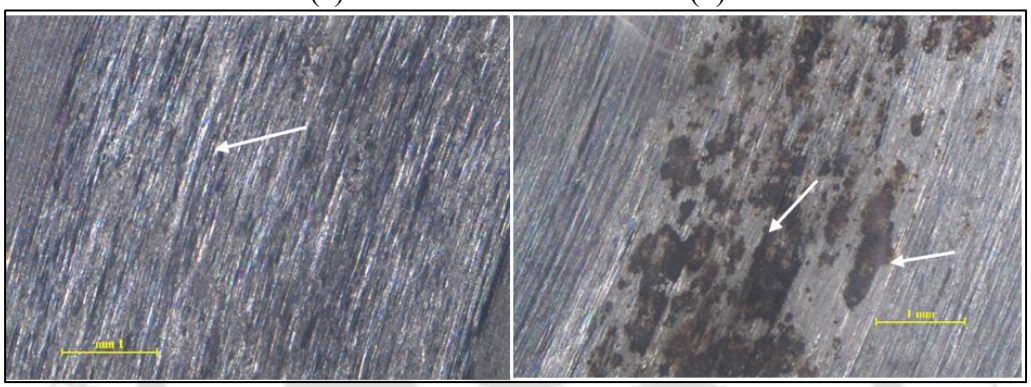

(c) (d)

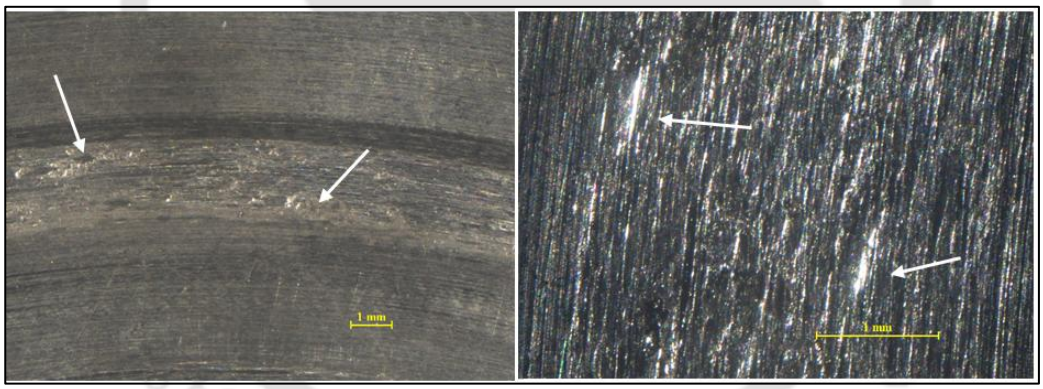

(e) (f)

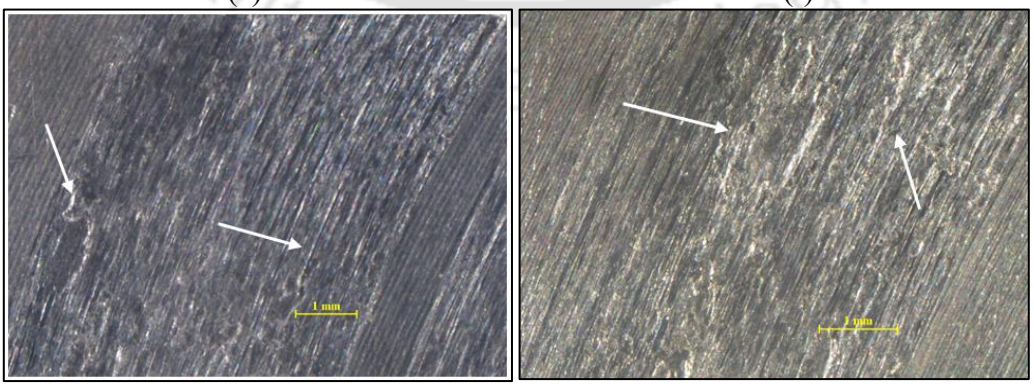

(g) (h)

Figure 6.20 Worn out surfaces of discs by various parameters (a) 10N 150RPM (b) 10N 200RPM (c) 10N 250RPM (d) 10N 300RPM (e) 15N 150RPM (f) 15N 200RPM (g) 20N 200RPM (h) 20N 300RPM

Figures 6.20 (a) to (h) depicts the optical stereo-micrographs of the wear track of the disc (SS316 disc) after wear testing of the hardened HP40Nb pin. The figures reveal features mainly material displaced due to plastically impressed grooves, delamination, and material transfer which are typical of adhesive wear.

6.3.5 Surface Topography

Figures 6.21 and 6.22 depict the 3D profile of the abraded HP40Nb pin and SS316 discs

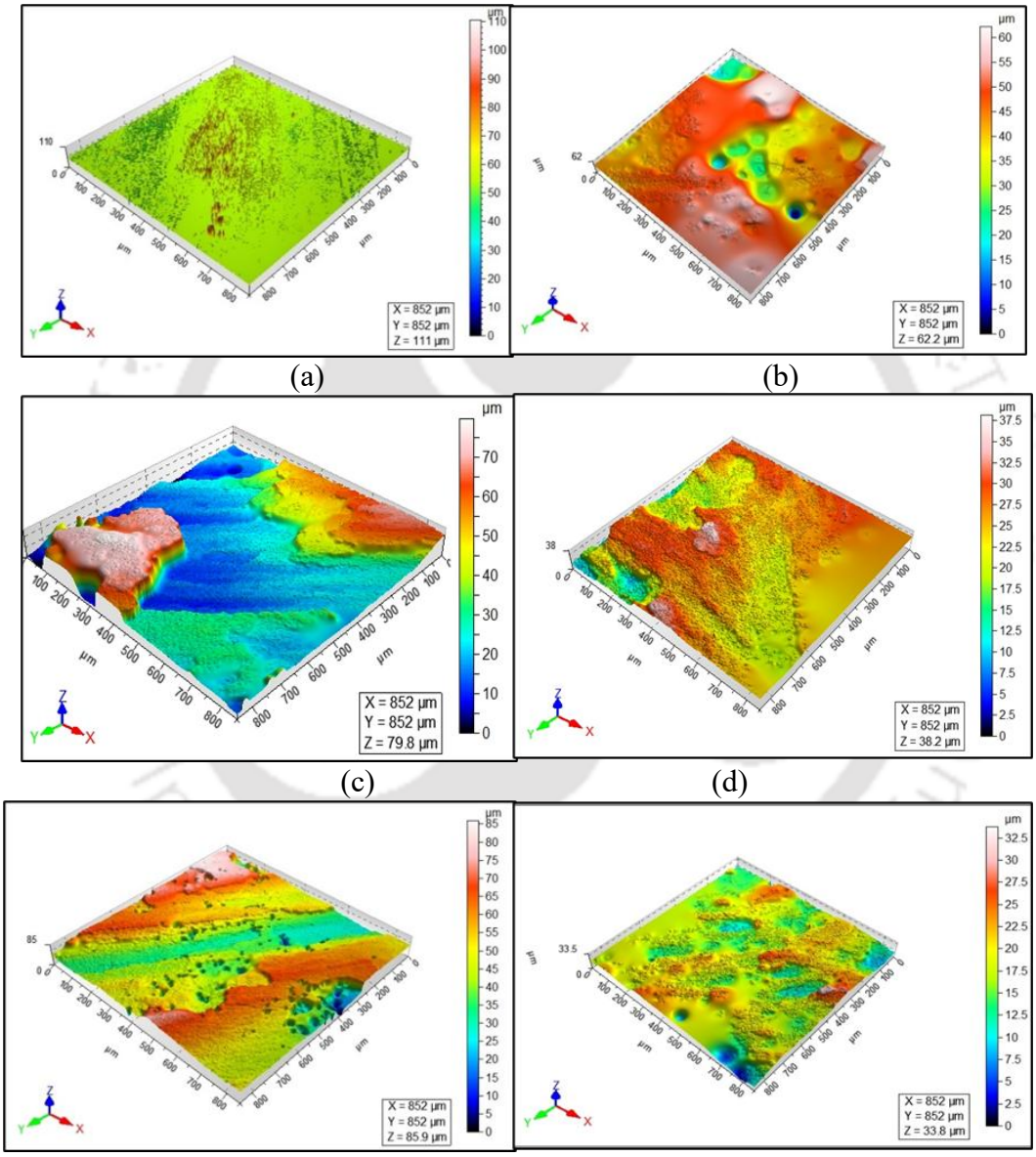

Figure 6.21 The 3D profile of the HP40Nb pin surface wear tested at (a) & (b) 10 N 150 RPM, (c) and (d) 20 N 200 RPM, (e) and (f) 10 N 300 RPM. (a), (c) and (e) before HT and (b), (d) and (f), after HT.

surfaces respectively by adhesive wear for different parameters a) before carburizing b) after

carburizing. In case of adhesive wear, the worn surfaces of a constant cross section areas of 852 µm × 852 µm, showed difference in *z* value. For maximum cases, the value was more for the specimens before carburization. The change is due to the increase in hardness of the surface after carburization. It is also justified by reduction in wear rate post carburization.

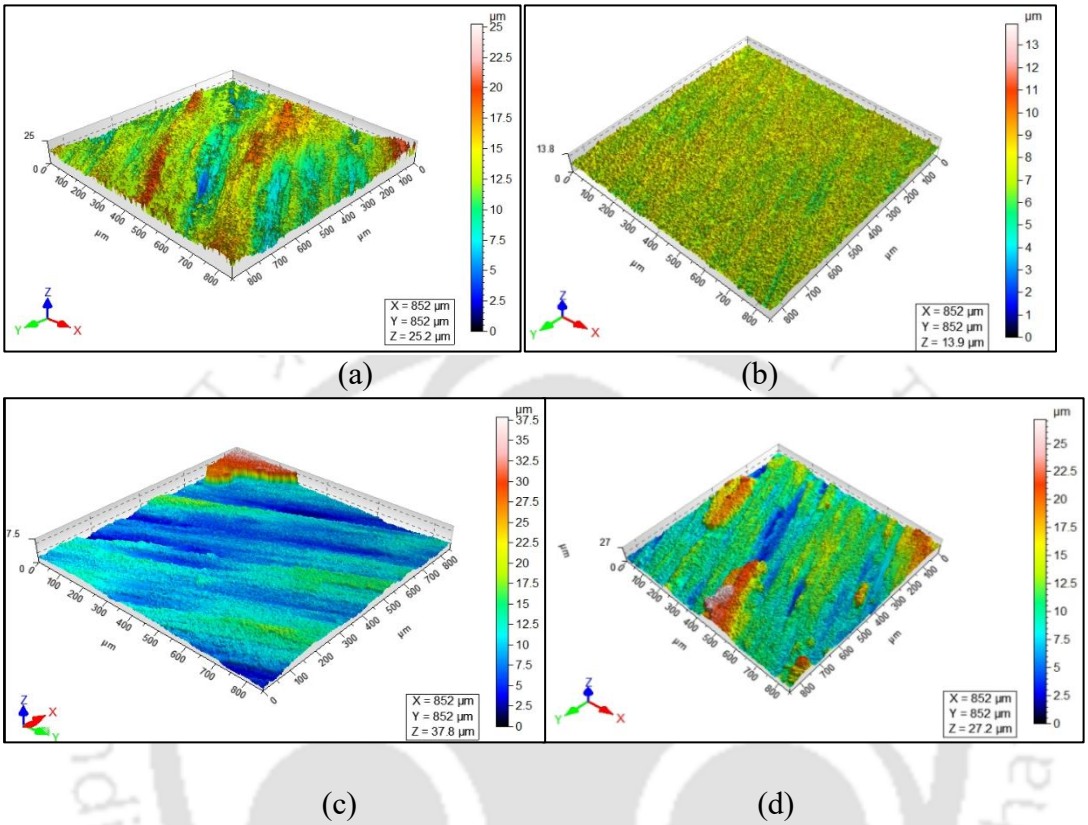

Figure 6.22 3D profile of the abraded SS316 disc surfaces tested at: (a) & (b) 10 N 150 RPM, (c) & (d) 20 N 150 RPM. (a) & (b) as-received (c) & (d) after Heat treatment

6.3.6 Wear Debris Analysis

The results of the SEM / EDS analysis of the post heat treated wear debris collected after wear test is presented in the subsequent subsections. Figures 6.23 (a) – (d) show the SEM micrographs obtained after adhesive wear. The initial stage of wear testing reveals presence of large irregularly shaped debris indicative of abrasive wear. However, as the test progressed, wear debris was detached from the surface by mechanism of delamination [12]. Figure 6.23 (c) and (d) illustrates plate-like wear particles which were peeled during the wear testing [105]. Presence of carbides due to the diffusion of carbon through the grain boundaries results in higher hardness at the carburized case region. This hard layer at the surface and subsurface regions of the heat treated pin results in finer wear debris for the heat treated sample compared to that obtained in the as-received sample [12].

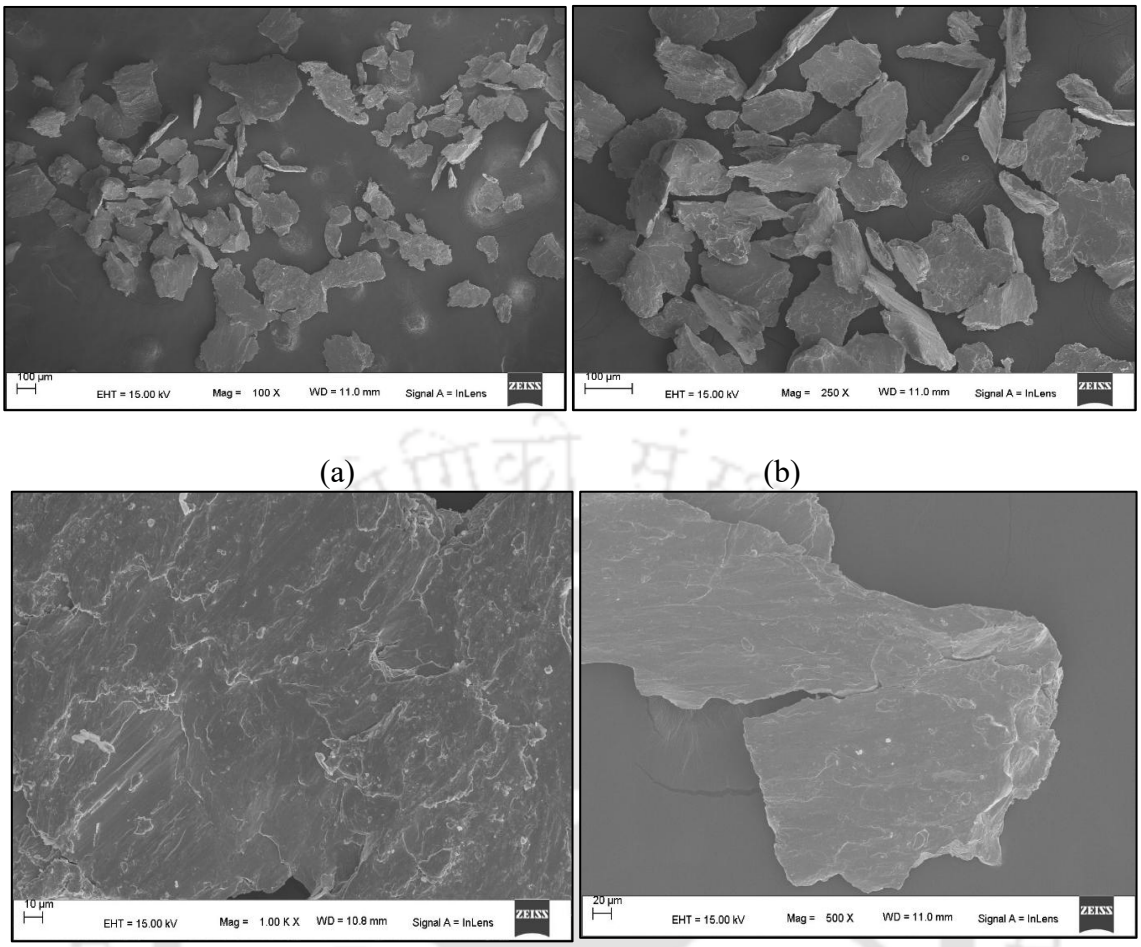

(a) (b)

(c) (d)

Figure 6.23 SEM images of wear debris

6.3.6.1 EDS Analysis of Wear Debris

Fig. 6.24 (a) and (b) shows the SEM micrograph and EDS spectrum of the wear debris of the heat treated steel, respectively.

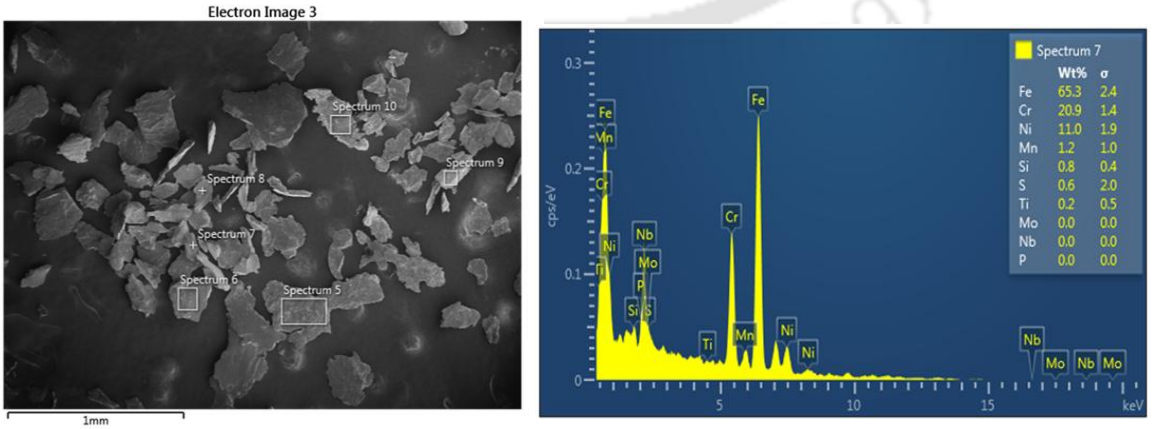

(a) (b)

Fig. 6.24 (a) SEM photo micro-graph and (b) EDS spectrum of wear debris after the wear test.

A close analysis of the composition of the pin and disc reveals that that the disc (SS 316) has a manganese content of 2 wt.% while HP40Nb steel do not have any manganese. The EDS analysis of the wear debris indicates material transfer from the soft disc to the hard pin, as revealed in Fig. 6.24 (b) by the presence of 1.2 wt.% Mn.

The debris after carburization heat treatment are finer than the debris formed during the adhesion test before carburization heat treatment. The EDS spectrum as shown in the figure suggests that wear particle fragmentation is more significant in heat-treated samples than in as-received samples. This occurs because heat-treated samples contain chromium precipitates along the grain boundaries.

6.4 Comparison of Abrasive and Adhesive Wear with Some Standard Materials

In order to compare the wear resistance of HP40Nb steel with some standard materials, adhesive and abrasive wear tests of high speed steel (HSS) and SS304 were performed under few parametric conditions, which were judiciously selected. The wear rate under different parameters are shown in figures 6.25 and 6.26 respectively. Figure 6.26 illustrates the abrasive wear rate of HP40Nb steel, HSS and SS304. Among these materials the highest wear rate is observed in SS304 and lowest for HSS. The abrasive wear rate of HP40Nb steel lies between the SS304 and HSS. It is evident that while using finer grit size abrasives, the difference in the wear rate of heat treated HP40Nb steel and HSS is almost the same whereas the as-received HP40Nb steel and SS304 is higher. While using the finest grit size abrasive disc 600 G, the wear resistance of all the four materials differ only marginally.

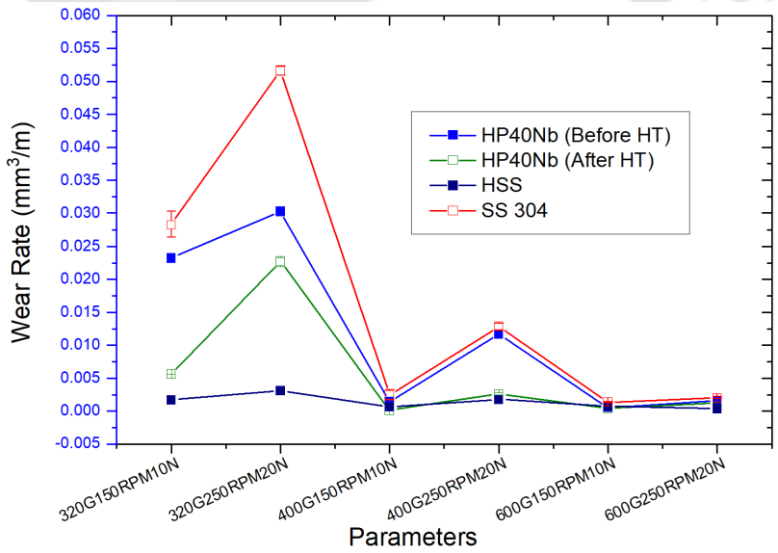

Figure 6.25 Comparison of Abrasive Wear Rate of HP40Nb with HSS and SS304

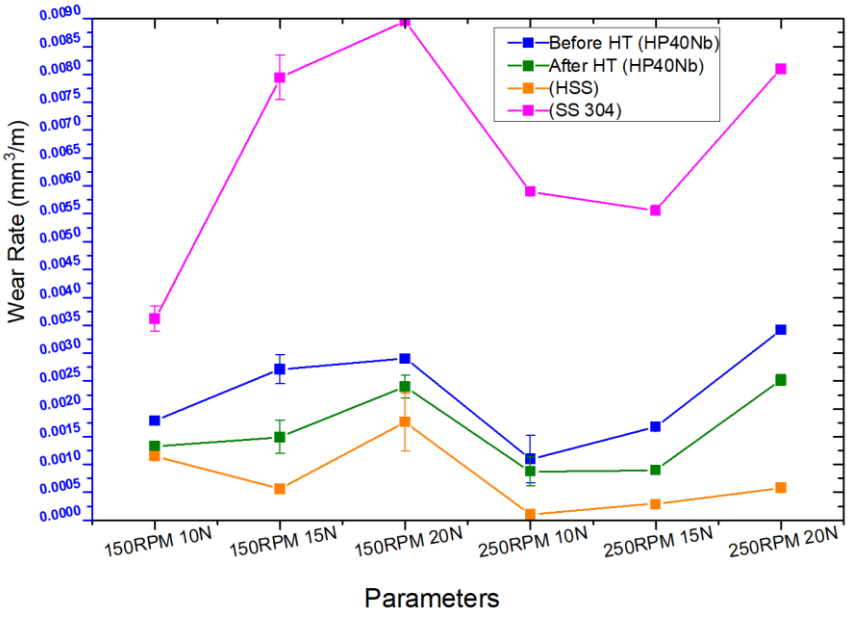

Figure 6.26 Comparison of Adhesive Wear Rate of HP40Nb with HSS and SS304

The adhesive wear rate of HSS, SS 304, and HP40Nb steel in the as received as well as carburised conditions are illustrated in Figure 6.26. It is evident that adhesive wear resistance of SS 304 is the least and increases in the order, as-received HP40Nb steel > carburized HP40Nb steel > HSS SS 304. At 150 RPM, the adhesive wear resistance increases as the normal load is increased from 10 N to 20 N. The same trend is observed when tested at 250 RPM.

6.5 Summary of Chapter 6

6.5.1 Abrasive wear

Wear rate of the steel increases with coarse surface of the abrasive disc. Carburizing results in decrease in the COF of the surface, which attributed to the high hardness achieved by the heat treatment. Carburizing increased the hardness of the steel surface by around 91%. At a load of 10 N and 200 RPM, the post-carburized pin samples with 320 G abrasives showed a comparable trend with an average wear rate reduction of approximately 42% and a maximum reduction of around 82%. The surface topography of the worn surfaces revealed the various modes of abrasive wear, such as ploughing, cutting, with intermittent groves, were dominantly observed for the abraded pin samples before carburization. Whereas material displacement due to the various impressed continuous grooves was noted in the abraded post carburized samples abraded surfaces. The profilometry investigation of the worn pin surface revealed a significant reduction in the Z value (vertical displacement of the surface) in the post carburized samples.

The SEM and EDS analysis reveals that the network of carbide precipitation is uniform in the sample after surface hardening treatment.

6.5.2 Adhesive wear

Surface hardening achieved through the carburizing heat treatment process leads to a substantial reduction in the coefficient of friction (COF). The diffusion of carbon into the surface layer forms high-hardness carbides, which enhance surface strength and resistance to plastic deformation. This hardened layer suppresses asperity adhesion and micro-ploughing during sliding, thereby minimizing frictional energy losses. Consequently, the wear resistance and overall tribological performance of the material are significantly improved.

The enhanced wear resistance of the carburized steel is attributed to a significant reduction in ploughing depth resulting from the increased surface hardness imparted by the heat treatment. Examination of the worn, post-carburized samples revealed evidence of plastic deformation, metal transfer, and delamination.

The hardened surface and subsurface layers of the heat-treated pin led to the generation of finer wear debris compared to the as-received sample, indicating a reduction in severe material removal during sliding. Elemental analysis of the debris revealed the presence of material from the disc, providing strong evidence of material transfer. These observations suggest that the increased surface hardness not only limits plastic deformation but also influences the wear mechanism, resulting in smaller debris and more controlled wear.

6.5.3 Comparison of Abrasive and Adhesive Wear with Some Standard Materials

The abrasive wear rate of HP40Nb steel lies between the SS304 and HSS. It is evident that while using finer grit size abrasives, the difference in the wear rate of heat treated HP40Nb steel and HSS is almost the same whereas the as-received HP40Nb steel and SS304 is higher. While using the finest grit size abrasive disc 600 G, the wear resistance of all the four materials differ only marginally.

The adhesive wear rate of HSS, SS 304, and HP40Nb steel in the as received as well as carburised conditions are illustrated in Figure 6.26. It is evident that adhesive wear resistance of SS 304 is the least and increases in the order, as-received HP40Nb steel > carburized HP40Nb steel > HSS SS 304. At 150 RPM, the adhesive wear resistance increases as the normal load is increased from 10 N to 20 N. The same trend is observed when tested at 250 RPM.

Chapter 7

Conclusions and Scope for Future Work

7.1 Conclusions

The present work was performed with the main aim of experimental investigation of abrasive wear and adhesive wear in HP40Nb austenitic steel. The study includes characterization of microstructure, DOE, wear testing, wear surface characterisation, effect of carburization on the adhesive and abrasive wear in HP40Nb steel. Finally, the wear resistance of this steel was compared with that of HSS and SS304. The results of the investigation have been presented in the previous chapters. The main conclusions of the thesis work are as follows:

Effect of test parameters:

- The most significant parameter affecting the abrasive wear of HP40Nb steel is the abrasive particle size. This is followed by the normal load and RPM, in the order.
- On coefficient of friction (COF), the significance of parameters in the order of grit size, load and RPM was found.
- The interaction in between the parameters was found significant on abrasive wear rate but not significant for COF.
- The adhesive wear rate increases with increase in load and speed.

Wear mechanisms:

- Worn surfaces of pin revealed the various modes of abrasive wear, such as ploughing, cutting along with intermittent groves.
- The mechanism of wear at lower speeds is by ploughing, micro cutting, and plastic deformation of the disc surface whereas at higher speeds, it is due to plastic deformation and metal transfer.
- The wear occurs by adhesion due to material transfer from the soft SS316 disc to the hard HP40Nb pin.

Effect of carburization:

- Carburizing heat treatment increases the hardness of the steel surface by around 91%. This is attributed to the precipitation of carbides in the sample surface during the heat treatment.
- Surface hardening by carburizing heat treatment process reduces the COF resulting in improvement in wear resistance.

- Both abrasive and adhesive wear rate decreases significantly after the carburizing heat treatment process.
- The high wear resistance of the carburized steel is due to the significant reduction in ploughing depth as a result of the high surface hardness achieved by the heat treatment.
- In the abraded post carburised samples, material displacement due to the plastically impressed continuous grooves was noted. Whereas in case of adhesive wear, plastic deformation, metal transfer and delamination were observed.
- Hardness increase by carburizing reduces *Z* value in the abraded surface of the steel.
- Diffusion of carbon leads to uniform precipitation of carbides at grain boundaries during Carburization heat treatment.

Comparative performance:

- The abrasive wear rate of HP40Nb steel is higher than SS 304 lower than HSS.
- With finer abrasive particles, the abrasive wear rate of heat-treated HP40Nb steel and HSS is only marginal. However, the variation in the wear rate between as-received HP40Nb steel and SS304 is more pronounced.
- The SS304 has the lowest adhesive wear resistance, which increases in the following order: as-received HP40Nb steel > carburized HP40Nb steel > HSS.

7.2 Future Scope

This study draws the comprehensive way to study the adhesive wear behaviour of reformer HP40Nb steel in pair with SS316 in the normal environmental temperature conditions.

a. Industrial Relevance

- The high-temperature wear resistance of HP40Nb steel should be evaluated to simulate its performance under actual industrial operating conditions such as those in petrochemical or power generation environments.
- The stability and integrity of the carburized layer at elevated temperatures should be examined to ensure long-term performance in cyclic thermal and mechanical loading conditions.
- The fracture toughness of HP40Nb steel at both ambient and elevated temperatures should be assessed to understand its behavior under dynamic and impact loading typical of service environments.

- Further studies on the weldability, machinability, and formability of HP40Nb steel can help determine its feasibility for component fabrication in industries such as chemical processing, energy, and automotive manufacturing.

b. Modelling Scope

- Finite element analysis (FEA) or predictive wear modelling can be employed to simulate the wear mechanisms and stress distribution in carburized HP40Nb steel under varying temperature and loading conditions.
- Computational modelling can assist in predicting carburization depth, diffusion profiles, and layer stability over time, reducing experimental costs and optimizing process parameters.

c. Sustainability and Economics

- A cost–benefit analysis comparing pack carburization with alternative surface treatments (e.g., nitriding, boriding, or thermal spraying) can be conducted to assess process efficiency, energy consumption, and overall economic viability.
- The sustainability of the carburization process can be evaluated by examining resource utilization, process emissions, and the potential for extending component life thereby reducing material waste and operational costs.

7.2 Limitations of the present work

The present work has following limitations which has further scope of study as follows

- The study has been focused on the abrasive and adhesive wear resistance of HP40Nb reformer steel. It can be even extended for analysing resistance of erosion, fretting, and corrosion.
- The process parameters like grit size, disc rotational speed, load for different ranges can be used for studying the wear resistance under various test conditions.
- The present work is carried out at the normal room temperature conditions however the high temperature abrasive and adhesive wear resistance can also be analysed.
- The present work have been carried out by prioritising the most common and economical method of pack carburization surface hardening treatment, however other surface hardening treatments such as nitriding, carbonitriding may also prove more efficient as compared to the presented pack carburization process.

REFERENCES

[1] ASM International, Stainless Steels for Design Engineers 2008. https://doi.org/10.31399/asm.tb.ssde.9781627082860.

[2] American Petroleum Institute, Calculation of heater-tube thickness in petroleum refineries: API recommended practice, Washington (DC),530, 3 (1988).

[3] J. Łabanowski, M. Jurkowski, M. Landowski, Effect of long term service at elevated temperatures on mechanical properties of manaurite XM reformer tubes, Advances in Material Science 16 (2016) 38–44. https://doi.org/10.1515/adms-2016-0021.

[4] T. Dessolier, T. McAuliffe, W.J. Hamer, C.G.M. Hermse, T.B. Britton, Effect of high temperature service on the complex through-wall microstructure of centrifugally cast hp40 reformer tube. Materials Characterization 177 (2020). https://doi.org/10.1016/j.matchar.2021.111070.

[5] J. Swaminathan, K. Guguloth, M. Gunjan, P. Roy, R. Ghosh, Failure analysis and remaining life assessment of service exposed primary reformer heater tubes, Engineering Failure Analysis 15 (2008) 311–331. https://doi.org/10.1016/j.engfailanal.2007.02.004.

[6] V.H. Dao, J.S. Song, J.Y. Kim, K.B. Yoon, Creep deformation characteristics of microalloyed HP40Nb steel at 950°C, Jornal of Mechanical Science and Technology 33 (2019) 4813–4821. https://doi.org/10.1007/s12206-019-0922-9.

[7] L. Shen, P. Jin, Y.i Wang, J.Gong, Numerical Simulation of Damage Evolution and Life Prediction for Two Commercial Fe–Cr–Ni Alloys Subjected to Mechanical and Environmental Factors, Journal of Pressure Vessel Technology (2016), Transactions of the ASME 138(5). https://doi.org/10.1115/1.4032916.

[8] A. Raj, B. Goswami, S.B. Kumar, G. Krishna, N. Roy, A.K. Ray, Performance and life assessment of reformer tubes in petrochemical industries, High Temperature Materials and Processes, 33 (2014) 217–230. https://doi.org/10.1515/htmp-2013-0041.

[9] M. Mostafaei, M. Shamanian, H. Purmohamad, M. Amini, A. Saatchi, Microstructural degradation of two cast heat resistant reformer tubes after long term service exposure, Engineering Failure Analysis, 18 (2011) 164–171. https://doi.org/10.1016/j.engfailanal.2010.08.017

[10] A. Ghatak, P. S. Robi, Effect of temperature on the microstructure and hardness of service exposed 25Cr35NiNb reformer tubes, Transations of Indian Institute of Metals 69 (2016) 823–827. https://doi.org/10.1007/s12666-015-0552-6.

[11] A. Ghatak, P. S. Robi, High-temperature Deformation Behavior of HP40Nb Micro-alloyed Reformer Steel, Metallography, Microstructure and Analysis 4 (2015) 508–517.

https://doi.org/10.1007/s13632-015-0235-z.

[12] L.H. Nemade, P.S. Robi, P. Biswas, Investigation on the mechanisms and mitigation strategies for adhesive wear in reformer HP40Nb steel, Emergent Materials 2024 https://doi.org/10.1007/s42247-024-00950-4.

[13] L.H. Nemade, P. S. Robi & Pankaj Biswas, Enhancing abrasive wear resistance in HP40Nb reformer steel through carburization, Australian Journal of Mechanical Engineering February (2025), https://doi.org/10.1080/14484846.2025.2469378.

[14] B. Bhushan, Introduction to Tribology, Second Edition. John Wiley and Sons, (2013). https://doi.org/10.1002/9781118403259.

[15] T. S. Eyre, Wear characteristics of metals, Tribology International (1976) 202–212. https://doi.org/10.1016/0301-679X(76)90077-3

[16] Stainless Steel Research Guide, Sheffield City Council, Sheffield Libraries Archives and Information v.1.0 (2011). https://www.sheffield.gov.uk/sites/default/files/docs/libraries-and-archives/archives-and-local-studies/research/Stainless-Steel-and-Harry-Brearley-v-1-1--PDF--578-KB-.pdf

[17] Steel Founders' Society of America 2004, Steel castings handbook, Supplement 9 High Alloy Data Sheets Heat Series. https://www.sfsa.org/wordpress/wp-content/uploads/2021/10/s9-2004.pdf.

[18] America Metal Academy, Capability and choice: Steel material for stainless steel, tool and special purpose, Metal Manual, 9th edition.

[19] D.J. Cox and D.E. Jordan, Proceedings of the Materials Technology Symposium Held on October 21–22, Pergamon Press, London 1964.

[20] R. H. Kane, Effects of silicon content and oxidation potential on the carburization of centrifugally cast HK-40, Corrosion, 37 (1981) 187–199.

[21] S.J. Zhu, P.E. Li, J. Zhao, Z.B. Cao, The effect of prior aging on the creep crack growth behaviour of austenitic HK40 steel, Materials Science and Engineering: A, 114 (1989) 7–12. https://doi.org/10.1016/0921-5093(89)90839-3.

[22] C. Stallybrass and G. Sauthoff, Ferritic Fe-Al-Ni-Cr alloys with coherent precipitates for high-temperature application, Materials Science and Engineering: A, 387–389 (2004) 985–990. http://dx.doi.org/10.1016/j.msea.2004.01.108.

[23] C.S. Li and Y.S. Yang, A glass based coating for enhancing anti-coking and anti-carburizing abilities of heat-resistant steel HP, Surface and Coatings Technology, 185 (2004), 68–73. http://dx.doi.org/10.1016/j.surfcoat.2003.12.010.

[24] F. Lechermama, M. Fahnlea and J.M. Sanchez, First-principles investigation of the

Ni-Fe-Al system, Intermetallics, 13 (2005) 1096–1109. http://dx.doi.org/10.1016/j.jssc.2009.07.026.

[25] M. Garbiak, W. Jasiński, B. Piekarski, Materials for Reformer Furnace Tubes. History of evolution, Archives of Foundry Engineering. 11, Special Issue 2/(2011) 47–52. https://scispace.com/pdf/materials-for-reformer-furnace-tubes-history-of-evolution-12298yy21o.pdf.

[26] S.J. Zhu, D.J. Li, Y. Wang, W.Q. Tian, S.G. Xu and F.G. Wang, Effect of niobium on creep and creep crack growth of cast Ni-Cr austenitic steel, Materials Science and Technology, 6 (1990) 119–1198. https://doi.org/10.1179/mst.1990.6.12.1193.

[27] J. Yan, Y. Gao, F. Yang, C. Yao, Z. Ye, D. Yi and S. Ma, Effect of tungsten on the microstructure evolution and mechanical properties of yttrium modified HP40Nb alloy, Materials Science and Engineering: A, 529 (2011) 361–369. http://dx.doi.org/10.1016/j.msea.2011.09.044.

[28] G.D. A. Soares, L.H. deAlmedia, T.L. daSilveira and I.L. May, Niobium additions in HP heat-resistant cast stainless steels, Materials Characterization, 29 (1992), 387–396. https://doi.org/10.1016/1044-5803(92)90045-J.

[29] R. Voicu, J. Lacaze, E. Andrieu, D. Poquillon and J. Furtado, Creep and tensile behaviour of austenitic Fe-Cr-Ni stainless steel, Materials Science and Engineering A, 510–511 (2009) 185–189. http://dx.doi.org/10.1016/j.msea.2008.04.098.

[30] K. Guan, H. Xu and Z. Wang, Quantitative study of creep cavity area of HP40 furnace tube, Nuclear Engineering and Design, 235 (2005) 1447–1456. http://dx.doi.org/10.1016/j.nucengdes.2005.01.009.

[31] R. Kirchheiner and P. Woelpert, Niobium in centrifugally cast tubes for petrochemical application, Proceedings of the International Symposium Niobium, Orlando, USA, (2001) 1–14.

[32] T. Sourmail, Precipitation in creep resistant austenitic stainless steels, Materials Science and Technology, 17 (2001) 1–14. http://dx.doi.org/10.1179/026708301101508972.

[33] R. Voicu, E. Andrieu, D. Poquillon, J. Furtado and J. Lacaze, Microstructure evolution of HP40-Nb alloys during aging under air at 1000 °C, Materials Characterization, 60, (2009), 1020–1027. http://dx.doi.org/10.1016/j.matchar.2009.04.007.

[34] C.J. Liu and Y. Chen, Variation of the microstructure and mechanical properties of HP40Nb hydrogen reformer tube with time at elevated temperature, Materials and Design, vol. 32 (2011) 2507–2512. http://dx.doi.org/10.1016/j.matdes.2010.08.031.

[35] H.C. Furtado and I.Le May, High temperature degradation in power plants and refineries, Materials Research, vol. 7 (2004) 103–110. http://dx.doi.org/10.1590/S1516-14392004000100015.

[36] A. Alvino, D. Lega, F. Giacobbe, V. Mazzocchi and A. Rinaldi, Damage characterization in two reformer heater tubes after nearly 10 years of service at different operative and maintenance condition, Engineering Failure Analysis, 17 (2010), 1526–1541. http://dx.doi.org/10.1016/j.engfailanal.2010.06.003.

[37] H. Czichos, Tribology and Its Many Facets: From Macroscopic to Microscopic and Nano-scale Phenomena, Meccanica 36 (2001) 605–615. http://dx.doi.org/10.1023/A:1016388517893.

[38] M. M. Khruschov, Principles of abrasive wear, Wear, 28 (1974) 69–88. https://doi.org/10.1016/0043-1648%2874%2990102-1

[39] Raymond G. Bayer, Fundamentals of Wear Failure. (2002) https://doi.org/10.31399/asm.hb.v11.a0003558

[40] M.A. Moore, A review of two-body abrasive wear, Wear, 27 (1974) 1–17. https://doi.org/10.1016/0043-1648(74)90080-5

[41] Koji Kato, Abrasive wear of Metals, Tribology International (1997) 333–338, Volume 30, Number 5. https://doi.org/10.1016/S0301-679X(96)00063-1

[42] M. Hawryluk, M. Marciniak, Gr. Misiun, Possibilities of investigating abrasive wear in conditions close to those prevailing in industrial forging processes, Maintenance and Reliability.16, 4 (2014).

[43] B. Narayanaswamy, P. Hodgson, H. Beladi, Comparisons of the two-body abrasive wear behaviour of four different ferrous microstructures with similar hardness levels, Wear, (2016). https://doi.org/10.1016/j.wear.2016.01.013

[44] A. Çoban, A. Demirer, F. Fiçici, Optimization of Wear Parameters of Polyamide-6 Composite Materials Filled with Wollastonite Particles, Periodicals of Engineering and Natural Sciences 2, 1 (2014). https://doi.org/10.21533/pen.v2i1.35

[45] T. Kivak, Optimization of surface roughness and flank wear using the Taguchi method in milling of Hadfield steel with PVD and CVD coated inserts, Measurement 50, (2014), 19–28. http://dx.doi.org/10.1016/j.measurement.2013.12.017

[46] B. Stojanović, S. Veličković, M. Babić, I. Bobić, Optimization of Tribological Properties IN A356/10SIC/5GR Hybrid Composite Using Taguchi Method, 15th International Conference on Tribology – Serbiatrib ’17 (2017). http://dx.doi.org/10.1177/0021998316672294.

[47] P. Serrao, R. Prabhu, Chiranth B. P., Yazid Mohammed, Application of Taguchi Method to Predict the Abrasive Wear Behavior of CP Titanium, Journal of Mechanical Engineering and Automation 6 (5A), (2016), 13–17. http://dx.doi.org/10.5923/c.jmea.201601.03

[48] V.C. Uvaraja, N. Natarajan, Optimization on Friction and Wear Process Parameters Using Taguchi Technique, International Journal of Engineering and Technology 2, 4 (2012). http://dx.doi.org/10.4236/jmmce.2012.118063

[49] A. Baradeswarana, R. Elayaperumal, I. Franklin, A Statistical Analysis of Optimization of Wear Behaviour of Al-Al2O3 Composites using Taguchi technique, Available online at www.sciencedirect.com, Procedia Engineering 64 (2013) 973–982. http://dx.doi.org/10.1016/j.proeng.2013.09.174

[50] S. Ghalme, A. Mankar, Y. J. Bhalerao, Optimization of wear loss in silicon nitride (Si3N4)–hexagonal boron nitride (hBN) composite using DoE–Taguchi method, Springer Plus (2016). http://dx.doi.org/10.1186/s40064-016-3379-7

[51] N. Radhika and R. Raghu, Evaluation of Dry Sliding Wear Characteristics of LM 13 Al/B4C Composites, Tribology in Industry 37, 1 (2015) 20–28.

[52] S. Ghosh, P. Sahoo, and G. Sutradhar, Tribological Performance Optimization of Al-7.5% SiCp Composites Using the Taguchi Method and Grey Relational Analysis, Hindawi Publishing Corporation Journal of Composites, (2013) 1–14. http://dx.doi.org/10.1155/2013/274527

[53] R. Ganesh, K. Chandrasekaran, M. Ameen, R.P. Kumar, Optimization of The Process Parameters For dry Sliding Wear of an AL 2219-SICP Composite Using The Taguchi-Based Grey Relational Analysis, Materials and technology 48 (2014), 361–366. UDK 669.018.95:620.178.1

[54] S. Sivaraosa, K.R. Milkey, A.R. Samsudin, A.K. Dubey, P. Kidd, Comparison between Taguchi Method and Response Surface Methodology (RSM) in Modelling CO2 Laser Machining, Jordan Journal of Mechanical and Industrial Engineering 8 1(2014) 35–42.

[55] G. Agarwal, A. Patnaik, R. Kumar Sharma, Parametric Optimization and Three- Body Abrasive Wear Behavior of Sic Filled Chopped Glass Fiber Reinforced Epoxy Composites, International Journal of Composite Materials 3 (2013) 32–38. https://doi.org/10.5923/j.cmaterials.20130302.02.

[56] S. Rajesh, S. Rajakarunakaran, R. Sudhakara Pandian, Modelling and Optimization of Sliding Specific Wear and Coefficient of Friction of Aluminium Based Red Mud Metal Matrix Composite Using Taguchi Method and Response Surface Methodology, Materials

Physics and Mechanics 15 (2012) 150–166.

[57] Y.T. Jou, W.T. Lin, W.C. Lee, T.M. Yeh, Integrating the Taguchi Method and Response Surface Methodology for Process Parameter Optimization of the Injection Molding, Applied Mathematics Information Science 8, 3 (2014) 1277–1285. http://dx.doi.org/10.12785/amis/080342.

[58] V. Singha, S.K. Pradhan, Optimization of WEDM parameters using Taguchi technique and Response Surface Methodology in machining of AISI D2 Steel, Science Direct, Available online at www.sciencedirect.com, Procedia Engineering 97 (2014) 1597–1608. http://dx.doi.org/10.1016/j.proeng.2014.12.310.

[59] G. Tressia, A. Sinatora, Effect of the normal load on the sliding wear behavior of hadfield steels, Wear (2023) 520–521. https://doi.org/10.1016/j.wear.2023.204657.

[60] X. Li, M. Sosa, U. Olofsson, A pin-on-disc study of the tribology characteristics of sintered versus standard steel gear materials, Wear 340-341 (2015) 31–40. http://dx.doi.org/10.1016/j.wear.2015.01.032.

[61] P.C. Okonkwo, G. Kelly, B. F. Rolfe, M. P. Pereira, The effect of sliding speed on the wear of steel–tool steel pairs, Tribology International 97 (2016) 218–227. http://dx.doi.org/10.1016/j.triboint.2016.01.030

[62] X. Ma, Y. Li, H. Cui, P. Zhu, Effect of speed and load on the dry sliding wear behaviour of titanium carbide coatings, IOP Conference Series: Materials Science and Engineering 394 (2018) 1–6. http://dx.doi.org/10.1088/1757-899X/394/3/032012

[63] M.A. Moore, The relationship between the abrasive wear resistance, hardness and microstructure of ferritic materials, Wear 28 (1974) 59–68. https://doi.org/10.1016/0043-1648(74)90101-X.

[64] P.C. Okonkwo, G. Kelly, B. F. Rolfe, M. P. Pereira, The effect of temperature on sliding wear of steel-tool steel pairs, Wear 282–283 (2012) 22–30. http://dx.doi.org/10.1016/j.wear.2012.01.017.

[65] F.H. Stott, High-temperature sliding wear of metals, Tribology International 35 (2002) 489–495. http://dx.doi.org/10.1016/S0301-679X(02)00041-5.

[66] J. Hardell, B. Prakash, High-temperature friction and wear behaviour of different tool steels during sliding against al–si-coated high-strength steel, Tribology International 41 (2008) 663–671. https://doi.org/10.1016/j.triboint.2007.07.013.

[67] B. Podgornik, Adhesive Wear Failures. Failure Analysis and Prevention. 22 (2022) 113–138. https://doi.org/10.1007/s11668-021-01322-4.

[68] H. Zhang, R. Goltsberg, I. Etsion, Modeling Adhesive Wear in asperity and rough surfaces contacts: a review. Materials (2022). http://dx.doi.org/10.3390/ma15196855.

[69] G. Wang, H. Zhao, Y. Zhang, J. Wang, G. Zhao and L. Ma, Friction and wear behavior of nm500 wear-resistant steel in different environmental media. Crystals 13, 770 (2023). http://dx.doi.org/10.3390/cryst13050770.

[70] H. Mohamed, E. shazly and S.A. Zaki, Adhesive wear prediction through finite element analysis in tribological applications. Journal of Egyptian Society of Tribology (2024) 109–134. http://dx.doi.org/10.21608/jest.2024.326515.1105.

[71] Lu Sun, Y. Li, C. Cao, G. Bi and X. Luo, Effect of Low-Temperature Plasma Carburization on Fretting wear Behavior of AISI 316L Stainless Steel. Coatings (2024) 1–20. http://dx.doi.org/10.3390/coatings14020158.

[72] S. Jiang, S. Zhang, J. Lin, X. Zhu, S. Li, Y. Sun, Y. Xia, W. Liu and C. Wang, Study on the microstructure and mechanical properties of martensitic wear-resistant steel. Crystals (2023) 1–14. https://doi.org/10.3390/cryst13081210.

[73] C.C. Viáfara, A. Sinatora, The effect of hardness of sliding bodies on the wear regime transition of steels, Lubrication Science 25 (2013) 123–138. https://doi.org/10.1002/ls.1198.

[74] G.J. Gore, J.D. Gates, Effect of hardness on three very different forms of wear, Wear (1997) 544–563. https://doi.org/10.1016/S0043-1648(96)07414-5.

[75] D.A. Rigney, The roles of hardness in the sliding behavior of materials, Wear (1994) 63–69, https://doi.org/10.1016/0043-1648(94)90169-4.

[76] N. Axén, S. Jacobson, S. Hogmark, Influence of hardness of the counter body in three-body abrasive wear — an overlooked hardness effect, Tribology International 27 (1994) 233–241. https://doi.org/10.1016/0301-679X(94)90003-5.

[77] J. Li, Z. Cao, L. Liu, X. Liu, J. Peng, Effect of Microstructure on Hardness and Wear Properties of 45 Steel after Induction Hardening, Steel Research International (2021) https://doi.org/10.1002/srin.202000540.

[78] T. Dessolier, T. McAuliffe, W. J. Hamer, C.G.M. Hermse, T. Ben Britton, Effect of high temperature service on the complex through-wall microstructure of centrifugally cast HP40 reformer tube, Material Characterization 177 (2021). https://doi.org/10.1016/j.matchar.2021.111070.

[79] Y. Kim, J. Kim, Evaluation of wear characterisitics of SKD11 substrate with advanced high strength steel, International Journal of Automotive Engineering 7 (2016) 121–126. http://dx.doi.org/10.20485/jsaeijae.7.4_121.

[80] K.H. Habig, Wear behaviour of surface coatings on steels, Tribology International, 22 (1989) 65–73. https://doi.org/10.1016/0301-679X(89)90167-9.

[81] T. Kayaba, K. Hokkirigawa, K. Kato, Analysis of the abrasive wear mechanism by successive observations of wear processes in a scanning electron microscope,Wear 110 (1986) 419-430. https://doi.org/10.1016/0043-1648(86)90115-8

[82] K. Hokkirigawa, K. Kato, The effect of hardness on the transition of the abrasive wear mechanism of steels, Wear, 123 (1988) 241 –251. https://doi.org/10.1016/0043-1648(88)90102-0.

[83] V.M. Golubets, V.V . Kozub, K. P. Tabinskii, Wear resistance of heat treated and chemical-thermally treated steel parts in the presence of an abrasive layer. Physicomechanical Institute, Academy of Sciences of the Ukrainian SSR, L'vov. 11, 4 (1975) 73–77.

[84] P.J. Mutton, J.D. Watson, Some effects of microstructure on the abrasion resistance of metals, Wear, 48 (1978) 385 - 398. https://doi.org/10.1016/0043-1648(78)90234-X

[85] C. Martini, G. Palombarini, G. Poli, D. Prandstraller, Sliding and abrasive wear behaviour of boride coatings, Wear 256 (2004) 608–613. https://doi.org/10.1016/j.wear.2003.10.003.

[86] D. Pereira, J. Gandra, J. Pamies-Teixeira, R.M. Miranda, P. Vilaça, Wear behaviour of steel coatings produced by friction surfacing, Journal of Materials Processing Technology, 214 (2014) 2858–2868 https://doi.org/10.1016/j.jmatprotec.2014.06.003.

[87] G.M. Michal, F. Ernst, A. H. Heuer, Carbon Paraequilibrium in Austenitic Stainless Steel, Metallurgical and Materials Transactions A Vol. 37a, June 2006, 1819–1824. https://doi.org/10.1007/s11661-006-0124-9.

[88] S. Liu, Q.Q. Guo, X.F. Wu, J. Shen, L.L. Liu, Y. Niu, Carburization of three Fe-19Ni-21Cr-xAl (x = 0, 2, 6 at. %) alloys at 900◦C in oxygen-contaminated CH_4/H_2 atmospheres, Corrosion Science 111 (2016) 436–445. http://dx.doi.org/10.1016/j.corsci.2016.05.008.

[89] D.B. Lewis, A. Leyland, P.R. Stevenson, J. Cawley, A. Matthews, Metallurgical study of low-temperature plasma carbon diffusion treatments for stainless steels, Surf. Coatings Technol. 60 (1993) 416–423. https://doi.org/10.1016/0257-8972(93)90124-7

[90] D.E. P. Klenam, C. Polese, L.H. Chown, S. Kwofie, L.A. Cornish, Mechanical behaviour of pack carburized AISI 316L austenitic stainless steel, The Journal of South African Institute of Mining and Metallurgy, (2015) 1183–1191. http://dx.doi.org/10.17159/2411-9717/2015/v115n12a6

[91] S.R. Collins, P.C. Williams, S.V. Marx, A. Heuer, F. Ernst, H. Kahn, Low-Temperature

Carburization of Austenitic Stainless Steels, Heat Treat. Irons Steels. 4 (2018) 451–460. https://doi.org/10.31399/asm.hb.v04d.a0005939

[92] M. Gathmann, N. Tonnißen, C. Baron, A. Kostka, M. Steinbacher, H. Springer, Surface hardening of high modulus steels through carburizing and nitriding: First insights into microstructure property relationships Surface & Coatings Technology 494 (2024). https://doi.org/10.1016/j.surfcoat.2024.131354.

[93] F. Novy , J. Harvanec, M. Mician, The Influence of Induction Hardening, Nitriding and Boronising on the Mechanical Properties of Conventional and Sintered Steels, 14, 1602 Coatings (2024) 1–20. https://doi.org/10.3390/coatings14121602.

[94] Y. Sun, X. Li, T. Bell, Low temperature plasma carburising of austenitic stainless steels for improved wear and corrosion resistance, Surface Engineering. 15 (1999) 49–54. https://doi.org/10.1179/026708499322911647.

[95] M. Egawaa, N. Ueda, K. Nakata, M. Tsujikawa, M. Tanaka, Effect of additive alloying element on plasma nitriding and carburizing behavior for austenitic stainless steels, Surface and Coatings Technology, 205 (2010) 246–251. http://dx.doi.org/10.1016/j.surfcoat.2010.07.093.

[96] I. Ciancaglioni, R. Donnini, S. Kaciulis, A. Mezzi, R. Montanari, N. Ucciardello and G. Verona-Rinati, Diffusion profiles after nitrocarburizing austenitic stainless steel 44 (2012) 1001–1004. http://dx.doi.org/10.1002/sia.4894.

[97] D. Wu1, Y. Ge, H. Kahn, F. Ernst, A. H. Heuer, Diffusion profiles after nitrocarburizing austenitic stainless steel, Surface & Coatings Technology. 279 (2015) 180–185. http://dx.doi.org/10.1016/j.surfcoat.2015.08.048.

[98] R.A. Savraia, P.A. Skorynina, A.V. Makarov, and A.L. Osintsev, Effect of Liquid Carburizing at Lowered Temperature on the Micromechanical Characteristics of Metastable Austenitic Steel, Physics of Metals and Metallography. 121 (2020) 1015–1020. http://dx.doi.org/10.1134/S0031918X20100105.

[99] X. An, Y. Tian, B. Wang, T. Jia, H. Wang, Prediction of the formation of carbide network on grain boundaries in carburizing of 18CrNiMo7-6 steel alloys, Surface and Coating Technology, 421 (2021). https://doi.org/10.1016/j.surfcoat.2021.127348.

[100] T. Wei, Z. Zhou, X. Ling, M. Lv, Y. Di, K. Qin and Q. Zhou, A Study of the Effect of roughness on the three-body wear mechanism from a microscopic point of view: asperity peak removal, Metals, 14, 1385 (2024) 1–21. https://doi.org/10.3390/met1412138.

[101] A. Kovalev, Z. Yazhao, C. Hui and Y. Meng, A concept of the effective surface profile to predict the roughness parameters of worn surface, Frontiers in Mechanical Engineering,

Section Tribology. 5 (2019) 1–11. https://doi.org/10.3389/fmech.2019.00031.

[102] L.H. Nemade, P.S. Robi & P. Biswas, Abrasive wear behaviour of HP40Nb reformer steel, Springer Nature, Lecture Notes in Electrical Engineering, (2023) 30–38. http://dx.doi.org/10.1007/978-981-99-4362-3_4.

[103] J. Gegner, A. A. Vasilyev, P. J. Wilbrandt and M. Kaffenberger Alloy Dependence of the Diffusion Coefficient of Carbon in Austenite and Analysis of Carburization Profiles in Case Hardening of Steels. Conference: MMT'2012 At: Ariel University Centre of Samaria, Ariel, Israel, 2012. http://dx.doi.org/10.13140/2.1.3871.2646.

[104] A. Ghatak, Creep Correlation of Micro-Alloyed HP40Nb Reformer Steel, PhD Thesis, Indian Institute of Technology, 2016.

[105] C.P. Fenili, M.R. da Rocha, K.S. Al-Rubaie, Â.B. Coelh o Arnt, E. Angioleto, A.M. Bernardin, Effect of sensitization on tribological behavior of AISI 304 austenitic stainless steel, International Journal of Materials Research. January 2018 http://dx.doi.org/10.3139/146.111594.

[106] Allen J. Fuller, Jr. Introduction to Carburizing and Carbonitriding, 2013. https://doi.org/10.31399/asm.hb.v04a.a0005811.

List of Publications

[1] **L.H. Nemade**, P.S. Robi, P. Biswas, Investigation on the mechanisms and mitigation strategies for adhesive wear in reformer HP40Nb steel, Emergent Materials, 2024. http://dx.doi.org/10.1007/s42247-024-00950-4.

[2] **L.H. Nemade**, P.S. Robi, P. Biswas, Enhancing abrasive wear resistance in HP40Nb reformer steel through carburization, Australian Journal of Mechanical Engineering, February (2025). http://dx.doi.org/10.1080/14484846.2025.2469378.

[3] **L.H. Nemade**, P.S. Robi, P. Biswas, Improving Adhesive Wear Resistance of HP40Nb Reformer After High-Temperature Carburization (Communicated).

[4] **L.H. Nemade**, P.S. Robi, P. Biswas, Microstructural evolution of HP40Nb stainless steel under carburization. (Under preparation).

Conference

[1] **L. H. Nemade**, P. S. Robi & P. Biswas, Abrasive wear behaviour of HP40Nb reformer steel, Springer Nature, Lecture Notes in Electrical Engineering, (2023) 30–38. http://dx.doi.org/10.1007/978-981-99-4362-3_4.